

Electrical Characterization of Carbon Nanotubes for Electronics

DISSERTATION

**zur Erlangung eines Grades eines Doktors
der Naturwissenschaften**

**der Fakultät für Mathematik und Physik
der Eberhard-Karls-Universität zu Tübingen**

vorgelegt von

Chen-Wei Liang

aus Taipei, Taiwan

2009

Tag der mündlichen Prüfung: 11.05.2009

Dekan: Prof. Dr. W. Knapp

1. Berichterstatter: Prof. Dr. D. Kern

2. Berichterstatter: Dr. habil. S. Roth

List of publications

Parts of this work were published in:

*Electrical characterization of the mutual influences
between gas molecules and single-walled carbon nanotubes*

C.-W. Liang, S. Sahakalkan, S. Roth
Small **4**, 432, (2008)

Electrical and Optical Transport of GaAs/Carbon Nanotube Heterojunctions

C.-W. Liang, S. Roth
Nano Lett. **8**, 1809, (2008)

Other publications

*In-situ Observation on Raman Spectra and Transport Properties
of Isolated Single-Wall Carbon Nanotubes*

C.-W. Liang, W.-Y. Lee, C.-H. Tsai, S. Roth
Phys. Stat. Sol. (**b**) 245, 2209, (2008)

Contents

Chapter 1 Introduction	1
1.1 Historical background.....	1
1.2 Organization of this Thesis.....	3
Chapter 2 Mesoscopic Systems	4
2.1 Introduction.....	4
2.2 Characteristic lengths.....	4
2.3 Low-dimensional systems.....	6
2.4 Realization of mesoscopic systems.....	8
Chapter 3 Carbon Nanotubes	13
3.1 Introduction.....	13
3.1.1 Crystal structure.....	13
3.1.2 Electronic properties.....	15
3.1.3 Nanotube electronics.....	17
3.2 Quantum transport in carbon nanotubes.....	20
3.2.1 Coulomb blockade.....	21
3.2.2 Quantum interference.....	27
3.2.3 Conductance quantization.....	28
3.2.4 Low-temperature transport in carbon nanotubes.....	30
3.3 Spin transport in carbon nanotubes.....	33
3.3.1 Introduction to spintronics.....	33
3.3.2 Spin transport in carbon-related materials.....	36
3.3.3 Spin transport in carbon nanotubes.....	37
Chapter 4 Carbon Nanotube Electronics with Different Contact Configurations	40
4.1 Introduction.....	40
4.2 Materials and methods.....	40
4.3 CNT with symmetrical contacts.....	41
4.4 CNT with asymmetrical contacts.....	45
4.5 Conclusions.....	49
Chapter 5 Semiconductor/Carbon Nanotube Heterojunction	50
5.1 Introduction.....	50
5.2 Materials and methods.....	51
5.3 Charge transport of GaAs/CNT heterojunctions.....	51
5.4 Conclusions.....	58
Chapter 6 Charge-Molecule Interaction in Carbon Nanotubes	59
6.1 Introduction.....	59
6.2 Materials and methods.....	60
6.3 Current-induced annealing (CIA).....	60
6.3.1 Gas desorption induced by CIA.....	60
6.3.2 Annealing mechanism.....	64
6.4 Influences of molecules on CNTs.....	66
6.4.1 Molecules as momentum-scattering centers.....	66

6.4.2 Molecules as spin-relaxation centers.....	69
6.5 Conclusions.....	74
Chapter 7 Summary	75
A Device fabrication and measurement set-up	77
A.1 Sample preparation.....	77
A.2 Electrical measurements.....	79
A.3 Low-temperature techniques.....	80
B High-field Transport in Carbon Nanotubes	82
Bibliography	85
Acknowledgments	93
Curriculum Vitae	94

Chapter 1

Introduction

1.1 Historical background

Human beings, driven by the force of curiosity, always pursue to understand the fundamental mechanisms and elements of nature. Many ancient philosophers in every culture have spoken of their viewpoints about the world based on their experiences and senses: the Greek philosophers proposed the idea of atoms, the Chinese Taoists pictured the concept of duality and the Buddhists explained the driving force of nature with causality. Among these and many other theories, similarities and differences exist. Due to the lack of analytical means, a big part of them had evolved into theology. However, the Newtonian mechanics developed since the 17th century enabled people to quantify the natural phenomena and exam some questions, which had been philosophical, in almost any field, including mechanics, thermodynamics, electrodynamics, etc. This ability finally turned the scientific knowledge into the applied technologies, which directly or indirectly resulted in the industrial revolution. As technology further advanced, people gained more abilities to expand their interests into ever bigger or smaller worlds. When the study was extended to the atomic level, mysterious phenomena hardly explained by the Newtonian theory emerged. This finally stimulated the birth of quantum mechanics in the early 20th century, which offers a new frame to the world of physics. For material science quantum mechanics laid the groundwork for the theories dedicated to the explanation of the electrical, optical and the magnetic properties of matter. Once the material properties were well understood and could be engineered, the development of the semiconductor industry was boosted in the late 20th century, leading the world into a *digital era*, in which the computer and Internet played more and more important roles in everyone's daily life. Quantum mechanics also offered an explicit model for the atomic/molecular structure and

therefore largely advanced the knowledge of chemistry, with which people were able to synthesize or engineer more molecules, composites and so on.

Although the material properties can now be understood and controlled nicely, mostly bulk matter as are addressed is in size larger than μm (or has more than 1,000,000,000,000 atoms). Theories for bulk properties often start from the atomic level and are then scaled up to an infinite size with the assumption of an ideal structure. However, not like the single atom, bulk materials often do not have ideal structures but contain defects, impurities and so on. Usually these imperfections are ignored or averaged out by the theories. Other factors that contribute to the non-ideal, including surface effects and environmental influences, are also neglected. Nevertheless, most of the bulk model indeed explains the experiment well and is practically useful. But when the size of the materials is down to the level where the size of the imperfections is comparable to the whole sample, the physics becomes more complicated and the material properties are more difficult to engineer. This leaves a gray area to be investigated: materials with the size ranging from a few nm to hundreds of nm. This is exactly of the size between the single atoms and bulk materials. In the past decades, material science and atomic physics have built a solid knowledge database for the macroscopic and the microscopic worlds, enabling people nowadays to get access into the *mesoscopic* world to map out the missing link in between.

This is the purpose that this thesis is dedicated to. The presented work tries to understand a *nanomaterial*: carbon nanotube (CNT), and studied the factors that influence its properties. CNT is a graphitic tubule with diameter around 1 nm. Since the discovery of CNT in 1991, much effort has been put into its properties in various aspects, including mechanical, optical and electrical ones. From these studies, people have learned that the experimental results of the nanotubes are sensitive to the probing means as well as the surrounding environments. It has been also shown that the physics of the CNT-based devices is complicated and the technology to engineer them is also challenging. This reflects the common concerns for the researches on nanomaterials. The major task of the thesis is to study the transport phenomena of CNT-based electrons, especially focusing on the variations of the device properties with the contact structures, environmental changes, etc., and then discuss these variations based on the updated knowledge of the nanotubes.

1.2 Organization of this Thesis

The thesis begins with, before going into the details of the experimental works, the basic concepts of the mesoscopic system as well as the introduction of the CNT: Chapter 2 discusses the definition and properties of the mesoscopic systems; Chapter 3 reviews both theoretical and experimental backgrounds of the nanotubes. In this chapter, lattice structure and the electronic properties will be first discussed and then the review of a set of experimental studies on the transport characteristics of the CNTs follows.

Chapter 4, 5 and 6 are the main research works of this thesis, where the discussions is based on the background knowledge given in the second and the third chapters. Chapter 4 discusses the transport properties of CNT devices with different configurations of metal electrodes, showing how the contact materials influence the device characteristics. Chapter 5 discusses the interface properties and the transport phenomena of the semiconductor/CNT junctions and shows the effects of the doping profiles of the semiconductors on the nanotube devices. Chapter 6 discusses the mutual interaction between the CNT and the gas molecules and the influences of the molecules on the transport properties. All the work is summarized in the last chapter, Chapter 7.

Experimental techniques are appended in Appendix A, where methods of preparing CNT devices and measurement equipments are described in detail. Appendix B reviews the physics of high-field transport in CNT in order to complement the discussion of experimental results in Chapter 6.

Chapter 2

Mesoscopic Systems

2.1 Introduction

The prefixes “macro-”, “meso-” and “micro-” come from the Greek word “macro”, “mesos” and “micro”, meaning large, middle and small respectively. The mesoscopic system thus has the scale between the macroscopic (bulk) and the microscopic ones (single atoms and molecules). For condensed matter, a mesoscopic system often means an object of the size of several nanometers. With the state-of-art technologies, many nanoscale materials have been produced and are available for systematical studies. To be more specific, a mesoscopic system does not necessarily have all its dimensions on the nanoscale. For example, one-dimensional (1D) systems are also in this category with two of their dimensions in nm size. For the electronic properties, materials at mesoscopic scale are often in the size smaller or comparable to the electron scattering lengths, making the transport properties different from their bulk forms.[DAT] Therefore, the mesoscopic system enables the studies of the fundamental mechanism of the electron transport, and the development of new technologies as long as there are properties available for engineering.

2.2 Characteristic lengths

When the electrons travel through condensed matter, their characteristics depend on the size of the sample and are governed by different mechanisms. For macroscopic matters, Ohm's law, a well-known behavior describing a linear relation between voltage and current, dominates. Ohm's law consists of an intuitive concept of multiple electron scattering: the Drude model.[AM] However, the application of Ohm's law is limited as the size of the sample becomes smaller. Here the word “smaller” is a relative term and the

exact size, at which Ohm's law is violated, depends on the material. To find out the border of the applicability of Ohm's law for different material systems, it is necessary to compare their characteristic lengths of the electrons with the sample size. Three characteristic lengths are often taken as the measures: (1) the electron wave length, (2) the mean-free-path length and (3) the phase-relaxation length. As long as the sample size is close to or smaller than these characteristic lengths, transport models other than Ohm's law should be considered.

Wavelength

In quantum mechanics, moving electrons are described as propagating waves. Since only the electrons with the energy close to the Fermi level, E_f , contribute to the current, the relevant length is the Fermi wavelength, λ_f , and can be written as

$$\lambda_f = \frac{2\pi}{k_f} = \frac{h}{\sqrt{2mE_f}} \quad (2.1)$$

where k_f is the Fermi wave vector and h is Planck's constant.

Mean free path

The movement of electrons in an ideal crystal is analogous to the Brownian motion of gas molecules in the vacuum: electrons travel straightly through a certain distance until “scattering” occurs. There are various sources of electron scattering. For a perfect crystal, electrons scatter with themselves and their traveling in the crystal is the same as in vacuum. But in reality, often the crystal is not ideal but has defects like impurities or lattice vacancies. Defects will increase the probability of the electron scatterings. Other sources like phonons and magnetic-polarized particles also contribute to the scattering and will dominate at certain physical regimes. Scattering changes the energy and the momentum of the electrons. The mean-free path, L_m , is then defined as the distance, at which an electron can travel freely without scattering. Since only the electrons with Fermi energy conduct, L_m can be calculated from

$$L_m = v_f \tau_m \quad (2.2)$$

where v_f and τ_m are the Fermi velocity and the momentum relaxation time (time between two subsequent scattering events) respectively.

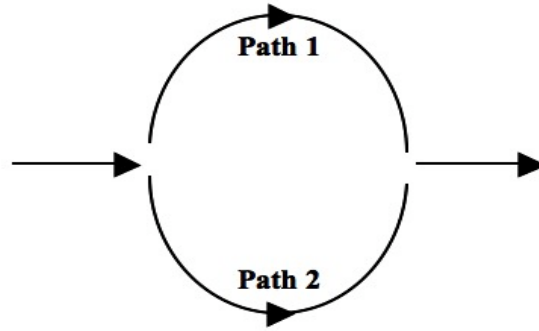


Figure 2.2.1 An electron wave, which is split into two due to scattering, can interfere with itself while recombining.

Phase-relaxation length

Similar to electromagnetic waves, electron waves also interfere with each others. One example is the interference of the incident waves with those reflected by an energy barrier. Another example is the interference of the electron waves split by scattering centers: an analogy to the single/double-slit experiment of light. While encountering a scattering center, the electron wave splits its propagating path, and then recombines afterwards (Figure 2.2.1). Phase shifts of the electron waves will cause a consequent variation of conductance. Constructive (in-phase) interference results in maximum electrical conduction, while destructive (out-phase) interference minimizes it. The phase-relaxation length, L_ϕ , can be written as

$$L_\phi = v_f \tau_\phi \quad (2.3)$$

where the τ_ϕ is the phase relaxation time.

2.3 Low-dimensional systems

In condensed matter physics, low-dimensional systems refer to physical objects of structure that extend to less than three dimensions. They could be a plane structure (2D), wire structure (1D) or dot structure (0D). To categorize the dimensionality of a material system, one should first specify what physical property is concerned. The same material could be classified to different dimensionalities in different topics: a steel bar is a 1D material when discussing its mechanical properties but a 3D material when its electrical property is concerned. For transport properties, the characteristic lengths, L_m and L_ϕ , are the

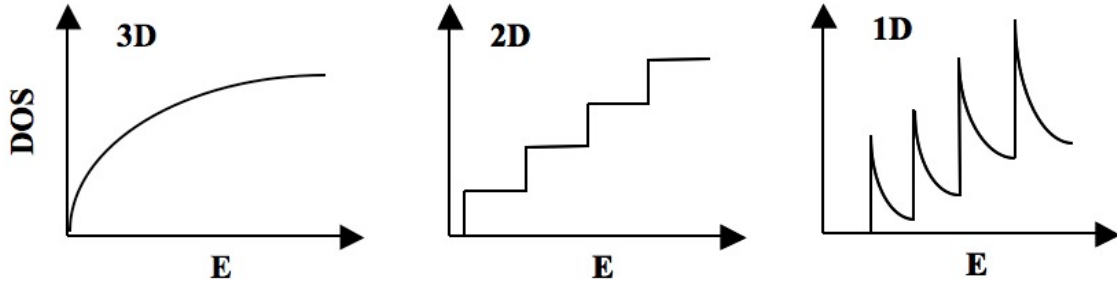


Figure 2.3.1 The density of states (DOS) of 3D, 2D and 1D systems.

measures to catalog the dimensionality of a material. A 2D material is, for example, a system with one of its dimensions in the scale comparable to or smaller than the characteristic lengths while keeping the other two relatively large. For electrons, this creates a strong confinement at one dimension and leaves the others approximately infinite. This would lead a 2D material to have a different electronic structure from its 3D form.

Electron density of states

The density of states (DOS) is important when discussing the electrical, optical and thermal properties of a condensed-matter system. It is a property quantifying how closely packed energy levels are in a quantum-mechanical system (numbers of eigenstates per unit energy interval and per volume). Due to the different electronic confinements of the 3D, 2D and 1D systems, their DOS is formulated differently, as the followings:

$$g(E)_{3D} = \frac{1}{2\pi^2} \left(\frac{2m^*}{\hbar^2} \right)^{3/2} \sqrt{E - E_{min}}, \text{ for } E \geq E_{min} \quad (2.4)$$

$$g(E)_{2D} = \frac{m^*}{\pi \hbar^2}, \text{ for } E \geq E_{min} \quad (2.5)$$

$$g(E)_{1D} = \frac{1}{\pi} \left(\frac{m^*}{2\hbar^2} \right)^{1/2} \frac{1}{\sqrt{E - E_{min}}}, \text{ for } E \geq E_{min} \quad (2.6)$$

where g is the DOS as a function of energy, \hbar is Planck's constant divided by 2π , m^* is the effective mass of the electron and E_{min} is the minimum of an energy band. Figure 2.3.1, which plots curves corresponding to eq. 2.4-6, shows the distinct dependence of the DOS of the materials with different dimensionalities on the electron energy. The DOS of the 3D system is a continuously parabolic curve but the 2D system has a stepwise curve. The quantization is more obvious in the 1D system, where the DOS consists of a multi-peaks

structure. These peaks appear at the minimum energy of each band and are called *van Hove singularities*, which originally described frequency distribution of the elastic vibration of crystals with different dimensions.[vH]

2.4 Realization of mesoscopic systems

Two-dimensional system

The realistic 2D system can be traced back to the metal-oxide-semiconductor field effect transistor (MOSFET), where the electrons (or holes) accumulate at the interface between the oxide and the semiconductor substrate. Figure 2.4.1a is a standard MOSFET with a p-doped Si and shows that electrons are attracted to the oxide/Si interface and create a conducting layer when a positive voltage is applied to the gate electrode (the poly-Si). The accumulation of the electrons therefore forms a 2D structure, where the motion of the electrons in the direction perpendicular to the surface is limited (confined).

Another example is using the heterostructure of III-V semiconductors, as shown in Figure 2.4.1b, and the accumulation of the electrons at the interface between the AlGaAs and GaAs is due to the space charge resulting from the Fermi-level alignment. Note that this structure is similar to the silicon MOSFET, where the oxide is replaced by the wide-bandgap AlGaAs. With a well-controlled growth condition for the GaAs/AlGaAs heterostructure, samples with mobility exceeding $10 \times 10^6 \text{ cm}^2/\text{Vs}$ are achievable.[UPH] This then gives the electrons a mean-free path longer than $100 \text{ }\mu\text{m}$, meaning that within that range the electrons in the 2D conducting layer travel as freely as the gas molecules do in vacuum. Therefore such a 2D electron conducting layer is also called 2D electron gas (2DEG).

Another 2D system is the graphene sheet (single layers of graphite, Figure 2.4.1c). Different from those artificial 2D systems made by Si-MOSFETs or GaAs-based heterostructures, graphene is a natural 2DEG. With its thickness down to the single atomic level, graphene is an ideal 2D system. Early studies suggested that 2D crystals are not stable and cannot exist without the support of substrates with matching lattice structures. However, the discovery of isolated graphene sheets on the amorphous SiO_2 or as suspended membranes showed that natural 2D crystals are available.[NG04][MG]

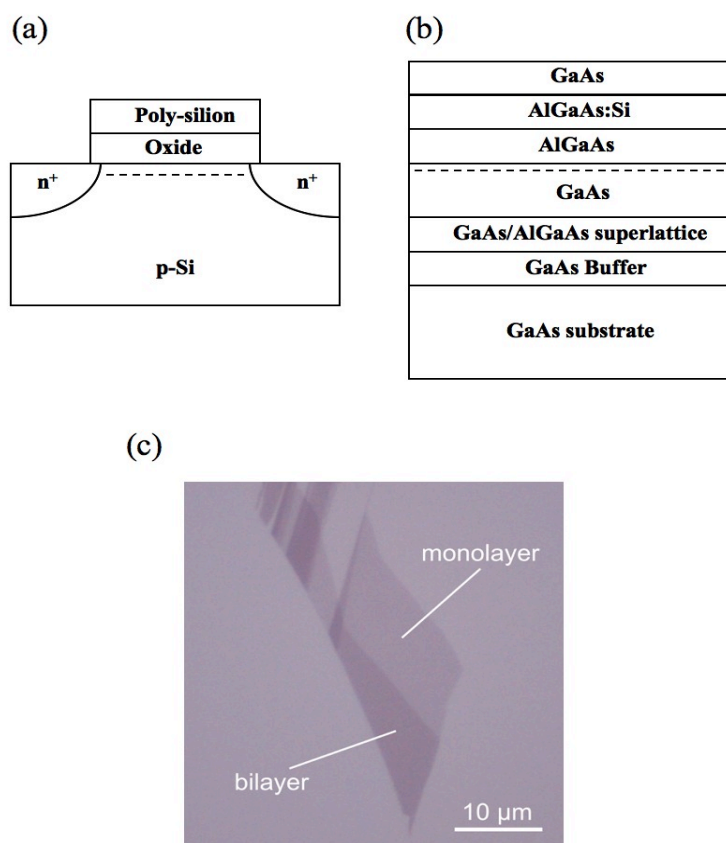


Figure 2.4.1 2DEG resulted from the electrons accumulated at the (a) oxide/silicon and (b) AlGaAs/GaAs interfaces. Dashed lines indicates the region of 2DEG. (c) A natural form of 2DEG: graphene sheets. Sheets with different layers are recognized with different transparencies, as indicated (Picture adopted from [GI].)

Graphene has revealed some unique properties, e.g. room-temperature high mobility ($200,000 \text{ cm}^2/\text{V}$)[MNK][BSJ] and room-temperature quantum hall effect (QHE)[NJZ], and enables the studies on massless Dirac fermions[NG05] and Kleiner paradox.[KNG]

One-dimensional system

As the 2D systems, the 1D systems can be also realized both artificially and naturally. Due to the reduced size in 1D materials, some of the 1D systems are also called quantum wires (QWs) when they show quantum-mechanical properties. To make an artificial 1D system one can pattern the gate electrodes on the GaAs/AlGaAs heterostructure to form a narrow conducting channel, as shown in Figure 2.4.2. The width of the channel is defined to be much smaller than the mean-free path of the electrons in the 2DEG in order to

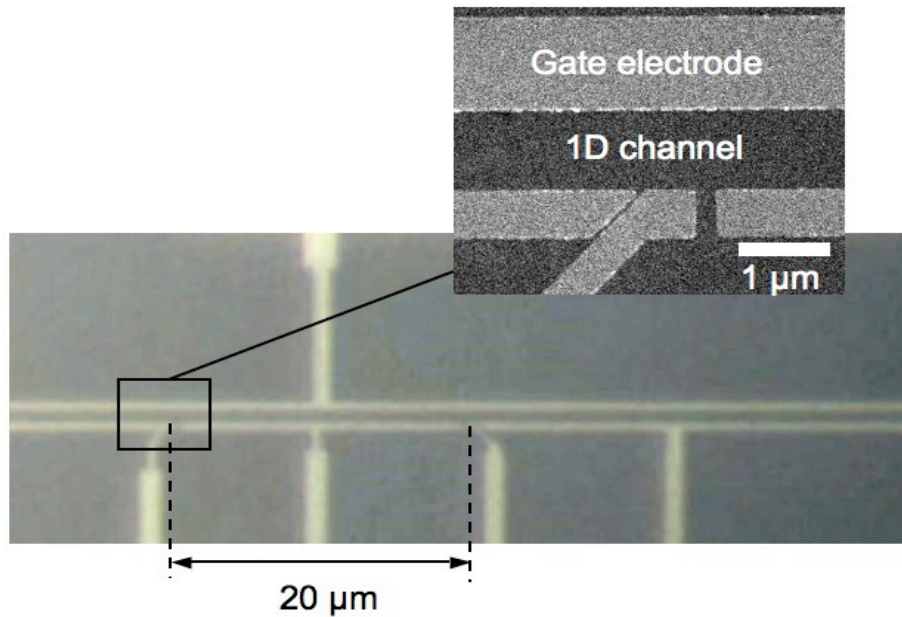


Figure 2.4.2 A quantum wire defined by the gate electrodes, which repel the electron gas underneath and consequently decouple the electrons in the 1D region from the surroundings (Pictures adopted from [FVY]).

confine the lateral movement of the electrons.

Naturally, there are numerous 1D materials existing in the forms of wires or tubes. They consist of single elements or compounds. 1D materials with various types, including conductors, semiconductors, ferromagnets and superconductors, have been synthesized successfully (Figure 2.4.3). Their diameters range from a few nm to hundreds of nm while the lengths may be in the scale of μm or even mm. The length of the 1D materials matches the scale of the state-of-art lithography technique, making the studies on isolated wires/tubes possible.

Zero-dimensional system

Like the above two mesoscopic systems, 0D systems (also called quantum dots, QDs) can be made via artificial or natural routes, too. The gate-defined QDs from 2DEG (Figure 2.4.4a) have been widely studied for their electronic structures and simulate that of the atoms, and hence have the synonym “artificial atoms”. [KM] By connecting several QDs in certain geometries, one can then build the “artificial molecule”. [BHW] This is an important step towards the engineering of quantum mechanics, since the size of a natural atom or molecule is too small to have a full control with current technologies.

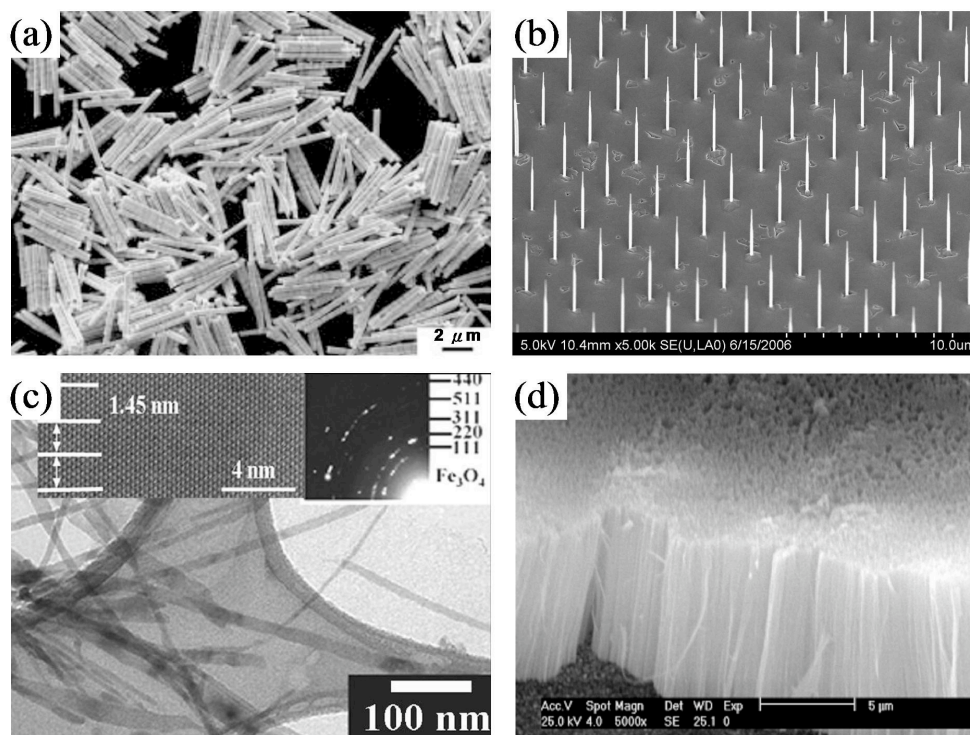


Figure 2.4.3 1D materials: (a) Au-Ag alloy.[QPH] (b) GaAs semiconductor.[CNR] (c) Half-metallic Fe₃O₄, Inset: high-resolution TEM image of the lattice structure of the Fe₃O₄ wire (left panel) and the diffraction pattern (right panel).[CCH] (d) Pb nanowires. [ZD]

The natural QDs usually consist of single particles in nanoscale. A milestone of this kind is fullerene (also called buckyball, Figure 2.4.4b). Other examples of the natural QDs are self-assembled semiconductor QDs (Figure 2.4.4c) and single molecules (Figure 2.4.4d).

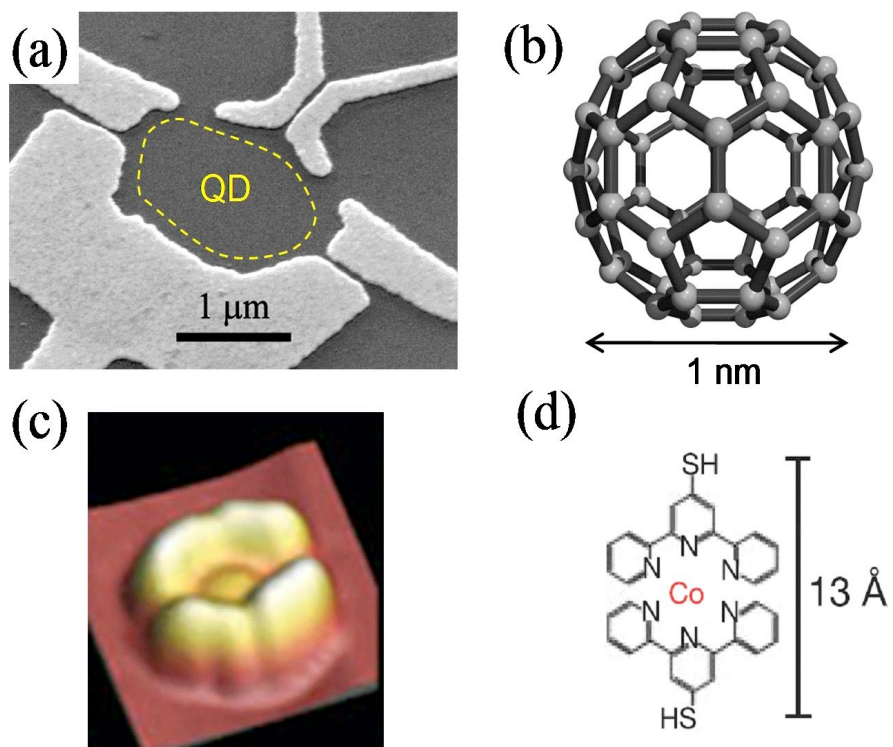


Figure 2.4.4 0D systems in the forms of (a) gate-defined quantum dot from the 2DEG (marked with the dashed line),[Bas] (b) fullerene,[Ken] (c) self-assembled InGaAs QDs (diameter: 150 nm),[LWS] (d) single molecules.[PPG]

Chapter 3

Carbon Nanotubes

3.1 Introduction

Carbon, given its hybridization of four-electron orbitals, has crystal structures in all kinds of dimensions.[SDD] Its 3D form, the diamond crystal, is used in the industries for cutting, drilling and polishing. Diamond is also very valuable in the gem industry due to its common use in luxury decoration. The 2D carbon is graphite, which can be found in the ancient Chinese ink since 1200 B.C. and nowadays is still one of the most important materials to pen industry for making pencils. Other than being used as a marking material, graphite is also employed in modern industry, e.g. as an ingredient to make steel or electrodes for the arc furnace. Since 1985, general interest in graphitic microstructures was excited among the science community due to the discovery of fullerene, a carbon material with the lattice structure of a soccer ball.[KHO] Its small size (diameter ~ 1 nm) boosts the development of nanoscience and nanotechnology. Soon after the discovery of fullerene, images of a kind of graphitic carbon in the tubular form with a diameter of only a few nm were published in 1991.[Iij] This material, which was called “microtubules” then and “carbon nanotubes” now, is a 1D carbon material. By that time, the four allotropes of carbon with different varieties have been demonstrated.

3.1.1 Crystal structure

Carbon nanotube (CNT) has the crystal structure of a honeycomb lattice and can be thought of as a rolled-up graphite sheet. Depending on the number of graphene layers folding as the walls of the tube, CNT is categorized into two groups: it is called *single-wall* carbon nanotube (SWNT) if the wall has only one atomic layer of carbon and *multi-wall* carbon naontube (MWNT) if there are more than one layers. Based on the lattice structure,

CNTs are further classified by the orientations of the carbon hexagons relative to the tube axis. The introduction of a so-called *chiral vector*, \mathbf{C}_h , is essential to such a classification.

Figure 3.1.1a shows an unrolled graphene sheet representing a SWNT. \mathbf{C}_h points in the direction of the circumference of the nanotube and T is the translational vector along the tube axis. The \mathbf{a}_1 and \mathbf{a}_2 are the lattice vectors. The blue lines are the edges that overlap when the honeycomb sheet is wrapped. An index system with \mathbf{a}_1 and \mathbf{a}_2 as the base vectors is then used to position each atom of the graphene lattice. The \mathbf{C}_h can be written as

$$\mathbf{C}_h = n\mathbf{a}_1 + m\mathbf{a}_2, \quad n \geq m. \quad (3.1)$$

according to the system. A nanotube is then specified by the pair of the integers (n, m) . Based on this index system, nanotubes can be classified into three groups: zigzag, armchair and chiral tubes. The zigzag tubes always have $m = 0$ while the armchair ones have $n = m$. The other nanotubes not belonging to the above two categories are referred to as chiral tubes. The diameter of a (n, m) tube, d_{nt} , can be calculated as

$$d_{nt} = \frac{|\mathbf{C}_h|}{\pi} = \frac{\sqrt{\mathbf{C}_h \cdot \mathbf{C}_h}}{\pi} = \frac{a\sqrt{n^2 + m^2 + nm}}{\pi} \quad (3.2)$$

where a is the lattice constant ($a = 2.49 \text{ \AA}$ for graphite). Because the lattice vectors, \mathbf{a}_1 and \mathbf{a}_2 , are not orthogonal, the inner product between \mathbf{a}_1 and \mathbf{a}_2 yields

$$\mathbf{a}_1 \cdot \mathbf{a}_1 = \mathbf{a}_2 \cdot \mathbf{a}_2 = a^2, \quad \mathbf{a}_1 \cdot \mathbf{a}_2 = \frac{a^2}{2}. \quad (3.3)$$

In addition to the diameter, the chiral angle, θ , is defined as the angle, at which the \mathbf{C}_h leans with respect to the zigzag axis, and can be also calculated from the (n, m) index:

$$\cos \theta = \frac{\mathbf{C}_h \cdot \mathbf{a}_1}{|\mathbf{C}_h| |\mathbf{a}_1|} = \frac{2n + m}{2\sqrt{n^2 + m^2 + nm}}. \quad (3.4)$$

Here one sees that the zigzag tubes ($m = 0$) and armchair tubes ($n = m$) have $\theta = 0^\circ$ and 30° respectively. For the chiral tubes, θ is between 0° and 30° . The helical structure of nanotube has been observed by imaging a SWNT with scanning tunneling microscopy (STM), as shown in the inset of Figure 3.1.1a.

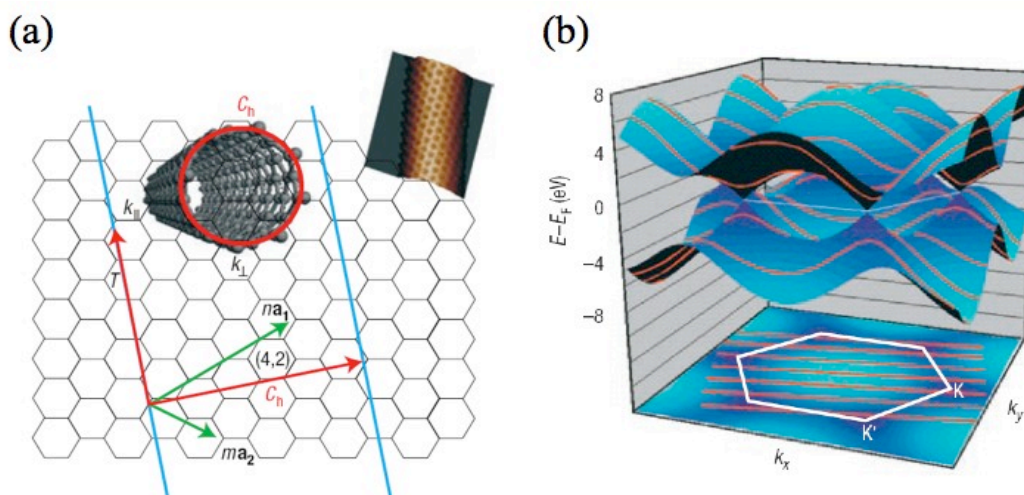


Figure 3.1.1 (a) Coordinate system of CNT. The area, sectioned by the blue lines from the surrounding lattice, represents an unrolled nanotube. The chiral vector, C_h , indicates the circumference direction (also shown by the red circle in the sketch of a nanotube). The STM image of a SWNT is shown in the upper-right corner. (b) Band structure of graphene and CNT. The π (lower part) and π^* (upper part) bands are separated at K points without gap. The hexagonal arrangement of the K points is indicated by the white lines. The bottom plane shows the projection of the band. Red lines represent the band quantization of the CNT, which may or may not overlap with the K points. (Pictures adopted from [ACP])

3.1.2 Electronic properties

Graphene

In the honeycomb lattice each carbon atom connects to three neighboring atoms and shares the sp^2 hybridized orbitals with them. The bonding orbits are called σ -bonds, which have the electrons localized between the atoms. This leaves one electron in the p_z orbital since carbon has the valence of four with three of them in the σ -bonds. The band structure of these p_z electrons calculated based on the tight binding model is illustrated in Figure 3.1.1b, which shows a Brillouin zone with a hexagonal symmetry. There are two bands crossing at the K -points of the Fermi plane, where the DOS is zero. The lower band is the π band (bonding) and upper one is the π^* band (anti-bonding). At the ground state, the π band is fully occupied by two electrons per unit cell. Because there is no energy gap between the π and π^* bands, graphene is also called zero-gap semiconductor.[GN] At the vicinity of the K -points the dispersion function is linear. Therefore the electrons with the

energy close to the Fermi level are massless and hence called massless fermions.

Nanotube

The distinction between the band structures of the graphene and nanotube comes from their different dimensions. Electrons in graphene move freely and meet no boundary in every of the in-planed directions. However, the small diameter of the nanotube puts a constraint on the electrons along the direction perpendicular to the nanotube axis and introduces a periodic boundary condition on its electron wave function:

$$C_h \cdot \mathbf{k} = 2q\pi, \quad (3.5)$$

where \mathbf{k} is the wave vector of the electrons and q is an integer. Due to the the boundary conditions, the Brillouin zone of the nanotube forms discrete lines in the k -space, as shown in Figure 3.1.1b. Depending on the chirality of the nanotube, the quantized lines may or may not overlap the K -points. Because the π and π^* bands of graphene cross at the K -points, the electrons in the nanotube with its Brillouin zone passing through the K -points see no energy gap. Therefore nanotubes of this type are metallic. If the Brillouin zone of the nanotube does not overlap with the K -points, electrons need additional energy in order to be excited to the conduction bands. In this case, they are semiconducting. Since it is the circumference as the boundary condition that decides the metallic/semiconducting properties, the chiral vector can then be used for the calculation of the band structure of nanotubes.[MDW][AA][HSO][JIN] The theoretical results show a simple equation available to deduce the electronic properties by the chiral index n and m : When $(2n + m)$ is a multiple of 3, the nanotube is metallic, otherwise it is semiconducting. As a consequence, one third of the SWNTs is metallic and two thirds are semiconducting and the armchair tubes are always metallic and the zigzag ones are semiconducting according to the calculation (Figure 3.1.2). Another important result is the dependence of the band gap of the semiconducting nanotube on the reciprocal of its diameter:

$$E_g = \frac{|E_t| a_{cc}}{d_t} = \frac{\pi |E_t| a_{cc}}{a \sqrt{n^2 + m^2 + nm}}, \quad (3.6)$$

where $|E_t|$ is the carbon-carbon tight binding energy and a_{cc} is the carbon-carbon distance (1.44 Å).

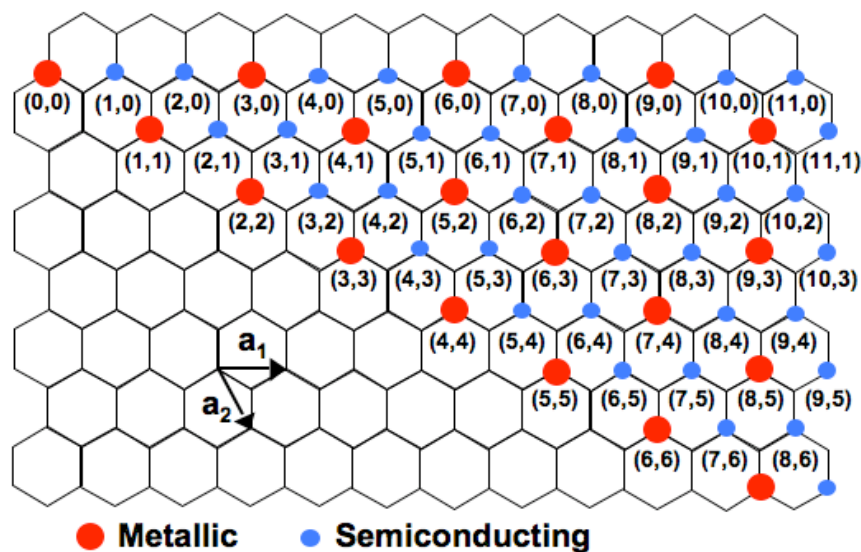


Figure 3.1.2 Metallic or semiconducting nanotubes according to their chiral index.

3.1.3 Nanotube electronics

Nanotubes have many merits in terms of application in electronics due to their unique characteristics like high electron mobility ($79,000 \text{ cm}^2/\text{Vs}$) [DGC], room-temperature ballistic transport [WT] [JGW] [LLL] and so forth. Much effort has been put into the development of CNT electronics. In this section different electronic devices, including field-effect transistors, Schottky diodes and sensors, made from isolated nanotubes are reviewed.

Field-effect transistors (FETs)

The core device in modern integrated circuit (IC) industry is the transistor. Its electrical switching behavior is realized by tuning the charge density inside the semiconductor. The most common transistor by far is the MOSFET, in which the charges (electrons or holes) in the region between the source and drain electrodes are controlled by the electrical field applied by the gate electrode (Figure 2.4.1a). Nanotubes fulfill the central criterion of the transistor (the tunable conductance) because two thirds of them are semiconducting and therefore are suitable for the transistor application. [TVD] [BHN] [MSS]

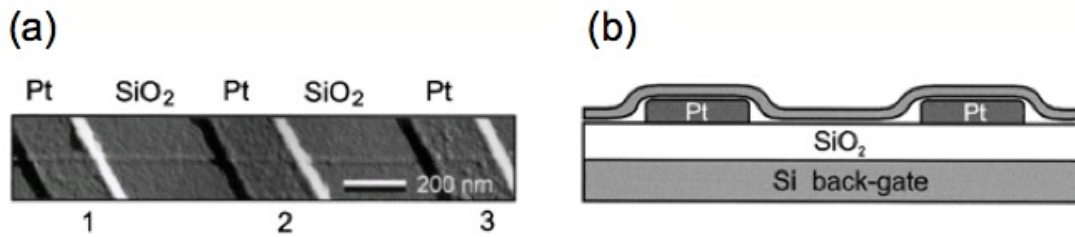


Figure 3.1.3 Carbon nanotube field effect transistor. (a) AFM image of the CNTFET. (b) CNTFET in sketch. A nanotube lying on the SiO₂ and platinum leads used as source and drain electrodes. The doped Si substrate functions as the back gate electrode. Pictures adopted from [TVD]

Figure 3.1.3 demonstrates a carbon nanotube field-effect transistor (CNTFET) consisting of a SWNT lying on platinum leads. Experiments show that the CNTFET is a p-type transistor with holes as the charge carriers. Such a p-type characteristic opened the debate over its origin. Early theoretical and experimental results showed that oxygen doping is responsible for such a unipolar behavior,[CBI][BJC][JLC] while the later studies suggested that the Schottky barrier due to the Fermi-level alignment at the metal/semiconductor interface should be the dominating factor.[HTM][MDL][DMA]

From the practical viewpoints, the application of the CNTFET faces several technical challenges:

Electrical contacts: Electrical contacts to the nanotubes are not stable and the contact resistance deviates from device to device. Two factors are responsible for the quality of the metal contacts: (1) the wettability and (2) the work function of the metals. When metals are deposited on nanotubes, noncontinuous metal clusters may form on the tube surface instead of continuous films as long as they wet the CNTs poorly.[ZFC] Poor wettability causes a non-uniform contact area and hence degrades the contact quality. On the other hand, the work function of the metals is also important because it determines the height of the Schottky barrier at the metal/SWNT interface. The barrier increases when the misalignment of the Fermi levels between SWNT and metal increases, giving larger contact resistance. Different

metals have been tried in order to optimize the contact quality.[CAK] Among various choices, contacts made by palladium (Pd) have been discovered to be nearly ohmic and the CNTFETs with Pd contacts show ballistic transport even at room temperature.[JGW]

Separation of nanotubes: The raw material of CNT consists of both metallic and semiconducting tubes. Without separation of these two types of tubes, the electronic devices or circuit will be a mixed system of both types and easily short-circuited by the metallic nanotubes. In such a situation, the semiconducting tubes cannot function properly.[KHL]

Chirality control: As shown in eq. 3.6 the band gap of the nanotube depends on its chirality and is different from one nanotube to another. This is a drawback to the application of the CNTFETs for the IC industry because the switching voltage of the transistors cannot be well controlled. Therefore the chirality control is another critical issue for the application of the CNTFET.

Channel length: Although the CNTFET is a building block for nanoelectronics, the IC industry will not benefit much until the gate length (the distance between the source and drain electrodes) is made small enough, because what really is in nanoscale with a CNTFET is the diameter of the nanotube but not the channel length. Shrinking the channel length to an ever smaller scale is a common challenge to the transistor technologies in order to increase the device number on a Si chip. Therefore efforts are still needed to reduce the device size in order to make a more compact IC system.[SGK]

Schottky diodes

Schottky diodes are rectifying metal/semiconductor junctions, which are often employed in high-frequency applications in the range of 3 – 30 GHz due to their high switching speeds. Devices made of Schottky diodes like detectors, mixers and frequency multipliers are the main components of the front-end circuit of wireless communication systems. However, when increasing the working frequency to the hundred GHz range, conventional diodes have problems with inherent parasitic capacitances (proportional to the junction

area) and the resistance (inversely proportional to electron mobility). Therefore, from the material point of view, nanotubes are an excellent alternative to their solid-state counterparts because of their small diameters and high mobility. A CNT Schottky diode (CNTSD) is achievable by contacting the nanotubes with different metals: One of the contacts is ohmic while the other has a Schottky interface. Current rectification has been observed in this kind of devices due to such asymmetrical contacts.[MWS] Early results show that the large lumped series resistance downgrades the performance of CNTSDs but after optimizing the device structure, results from CNTSDs in THz range could be comparable to those made of GaAs.

Sensors

The tube wall of the SWNTs has a thickness of only one atomic layer. Since their surface is also where the electrons are transported, every change at the surface would easily influence the transport properties. This also implies that SWNT has merits in sensing technologies. Another perspective of the SWNTs on sensing is their large surface area, which would also increase the sensing efficiency. Indeed, several studies of CNTFETs have shown that the transport properties change with the presence of gas species like NO₂, NH₃, CO, etc.[NKZ][LLY] or certain biomolecules[DCA], showing the suitability of CNTs for sensing applications. However, the main challenge to the practical applications of CNT sensors is to improve their selectivity, enhance their ability to discriminate the target objects from others.[CMG]

3.2 Quantum transport in carbon nanotubes

The small diameter of CNTs makes them an ideal material for the study of the basic physics of low dimensional systems. This is often done at low temperature to suppress thermal excitations of the electrons, keeping them at the ground state. In this section, several features of quantum transport of low-dimensional systems, including Coulomb blockade, quantum interference, ballistic transport and spin-coherent transport, are discussed. Their experimental studies with nanotubes will then be reviewed.

3.2.1 Coulomb blockade

A three-terminal transport system as well as the equivalent circuit are shown in Figure 3.2.1a and b. A small conductor, the quantum dot, is connected with two leads, the source and drain and an additional gate electrode coupling capacitively to the dot. In order to resolve the electrical spectra of a quantum dot at its ground state, it is important to minimize the number of charges going through the circuit. The optimum condition is to control the conduction down to the single-electron level. For this purpose, sufficient energy barriers are needed at the interfaces between the dot and the leads in order to decrease the electron tunneling rate. Another requirement is that the charging energy of the conductor by single electrons should be high enough to suppress thermal excitation, otherwise the thermally excited electrons may overcome the Coulomb repulsion generated from the electrons inside the dot and tunnel into it. When the conditions are fulfilled, further electron tunneling into a charged QD will be prohibited by the Coulomb repulsion. The blockage of the electron tunneling is called *Coulomb blockade*. In the Coulomb blockade regime, the tunneling probability depends on whether there are available states in the dot for the electrons in the leads to fill in. If the energy state of the dot aligns well with the Fermi level of the lead, the tunneling probability increases. In case of misalignment, the tunneling rate decreases. Because it is the energy states of the dot that decide the tunneling probability, one can control the tunneling rate via the gate terminal, which tunes the energy of the QD electrostatically. It has been observed that while sweeping the gate voltage, the tunneling current of the QD either stays at zero or shows sharp peaks (Figure 3.2.1c). These peaks correspond to the condition, where there is an available state in the dot aligning with the Fermi level of the electrode, and the regions with zero conductance is due to the blockage of the electrons. Since the system controls the electron tunneling at the single electron level, it is also called a single-electron transistor (SET).[GD]

For more detailed discussions of the transport behavior of the SET, a capacitance model based on the equivalent circuit is applied. Assuming that there are N_0 electrons in the dot at zero gate voltage, the ground-state energy of the dot with N electrons is then given by

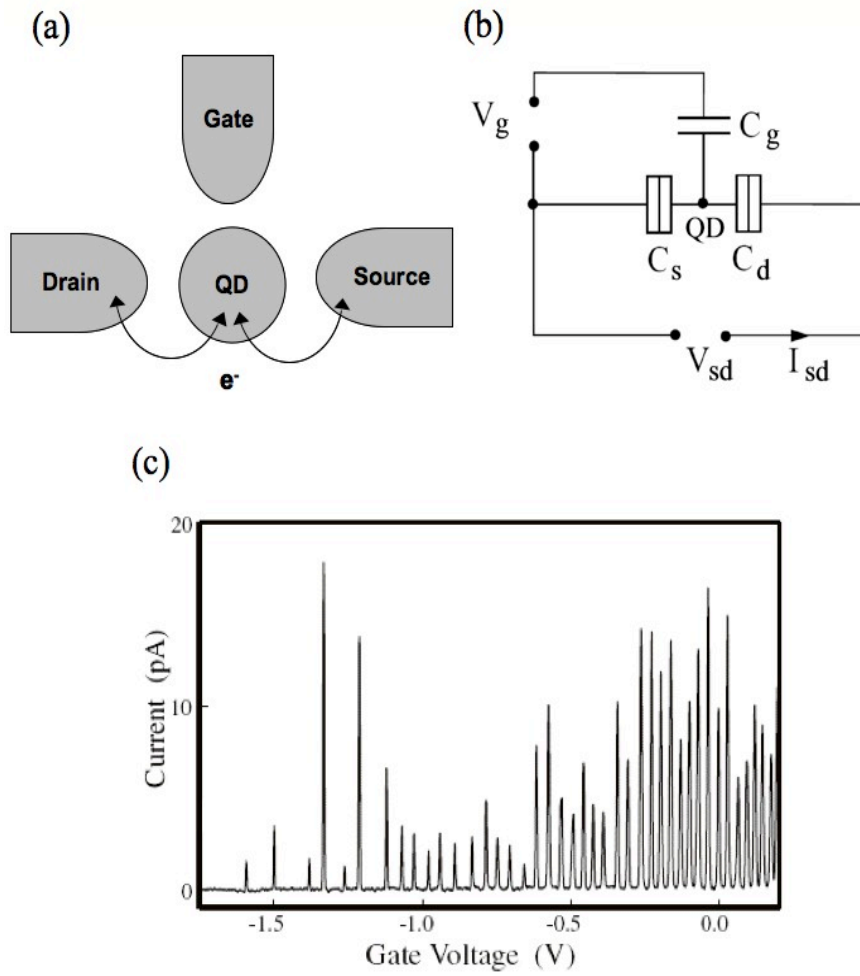


Figure 3.2.1 (a) A three-terminal quantum dot system. The electron tunnels between the dot and source/drain electrodes while the electrochemical potential is tuned by the gate. (b) Equivalent circuit diagram of the QD system. (c) Coulomb blockade peaks shown in the measurement of a QD (picture adopted from [KAT]).

$$U(N, V_g) = \sum_{p=1}^N E_p + \frac{1}{2C_\Sigma} [-e(N - N_0) - C_g V_g]^2. \quad (3.7)$$

where C_Σ is the sum of the capacitances of source, drain and gate (C_s , C_d and C_g) and E_p is the single-particle energy. The first term is the sum over the occupied states up to N electrons and the middle term is the Coulomb repulsion generated from the additional electrons ($N - N_0$) in the dot at V_g . The last term is a continuous variable induced by the gate voltage. The electrochemical potential μ_{QD} is then defined as

$$\mu_{QD}(N, V_g) \equiv U(N, V_g) - U(N-1, V_g) = E_N + \frac{(N - N_0 - 1/2)e^2}{C_\Sigma} - e \frac{C_g}{C_\Sigma} V_g. \quad (3.8)$$

where E_N is the topmost filled single-particle state. Electrons will go through the dot when μ_{QD} is between the μ_s and μ_d , i.e. $\mu_s > \mu_{QD}(N) > \mu_d$. At zero bias ($eV_{sd} = \mu_s - \mu_d = 0$), the Coulomb peak directly measures the ground-state electrochemical potential $\mu_{QD}(N)$ because only the lowest unfilled state of the dot is available for the electrons to tunnel through. The addition energy is then given by

$$\Delta \mu_{QD}(N \rightarrow N+1) = \mu_{QD}(N) - \mu_{QD}(N+1) = \Delta E + \frac{e^2}{C_\Sigma}, \quad (3.9)$$

which shows that if the thermal energy, kT , is smaller than $\Delta E + e^2/C_\Sigma$, the electrons will be blocked when there is no available state in the bias window, as shown in Figure 3.2.2a. To overcome the blockage energy, one can tune the μ_{QD} with the gate voltage and as long as the condition

$$\Delta \mu_{QD}(N \rightarrow N+1, V_g) = \mu_{QD}(N, V_g) - \mu_{QD}(N+1, V_g + \Delta V_g) = 0 \quad (3.10)$$

is met, the addition of the electron does not cost energy. Under this condition tunneling probability will largely increase and so does the measured conductance. From eq. 3.8 and 3.10 the addition voltage ΔV_g is:

$$\Delta V_g = \frac{C_\Sigma}{eC_g} \left(\Delta E + \frac{e^2}{C_\Sigma} \right) \quad (3.11)$$

According to eq. 3.11, the addition voltage reveals the information of the change of the single particle energy, ΔE , which represents the energy structure of the dot. The process of the electron addition is shown in Figure 3.2.2b and c.

The condition discussed above is the spectroscopy of the dot at its ground state (due to zero bias). At high V_{sd} , the electrons are more energetic and able to fill the excited states of the QD. This occurs when the states of the dot align with the Fermi level of the source or drain or simultaneously both of them, as shown in Figure 3.2.3. All of these conditions will increase the tunneling rate and hence induce conductance increases in the circuit. The transfer of the energetic electrons at larger V_{sd} contributes additional energy to the electrochemical potential of the dot, pushing it away from its ground state. Thus the μ_{QD} in

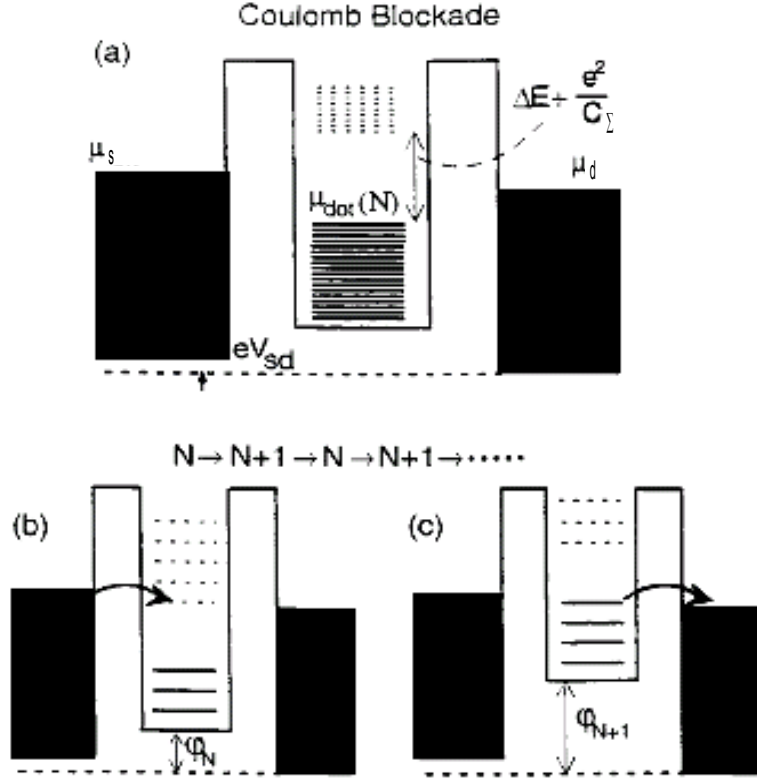


Figure 3.2.2 Potential profile through a quantum dot. The μ_s and μ_d are the upper most electrochemical potentials of the filled states of the electron reservoirs. The discrete 0D-states of the dot are represented by the lines within the barriers, where the filled and unfilled ones are solid and dashed respectively. (a) The addition of the $(N+1)^{\text{th}}$ electron into the dot is blocked at low temperature by the Coulomb energy of e^2/C_Σ . (b), (c) Given the the $\mu_{\text{QD}}(N+1)$ lies between the bias window, the tunneling probability over the barrier increases, leading to a current increase in the system. ϕ_N represents the total electrostatic potential resulted from the Coulomb repulsion and the gate voltage (the last two terms in e.q. 3.8). Pictures adopted from [KAT]

eq. 3.8 should be modified by taking the V_{sd} into account:

$$\mu_{\text{QD}}(N, V_g, V_{sd}) = E_N + \frac{(N - N_0 - 1/2)e^2}{C_\Sigma} - e \frac{C_g}{C_\Sigma} V_g - e \frac{C_d}{C_\Sigma} V_{sd}. \quad (3.12)$$

When μ_s aligns with μ_{QD} , the condition

$$\begin{aligned} & \Delta \mu_{\text{QD}}(N \rightarrow N+1, V_g, V_{sd}) \\ & = \mu_{\text{QD}}(N, V_g, V_{sd}) - \mu_{\text{QD}}(N+1, V_g + \Delta V_g, V_{sd} + \Delta V_{sd}) = 0 \end{aligned} \quad (3.13)$$

is fulfilled, enabling the tunneling of the electrons from the source into the dot. From the

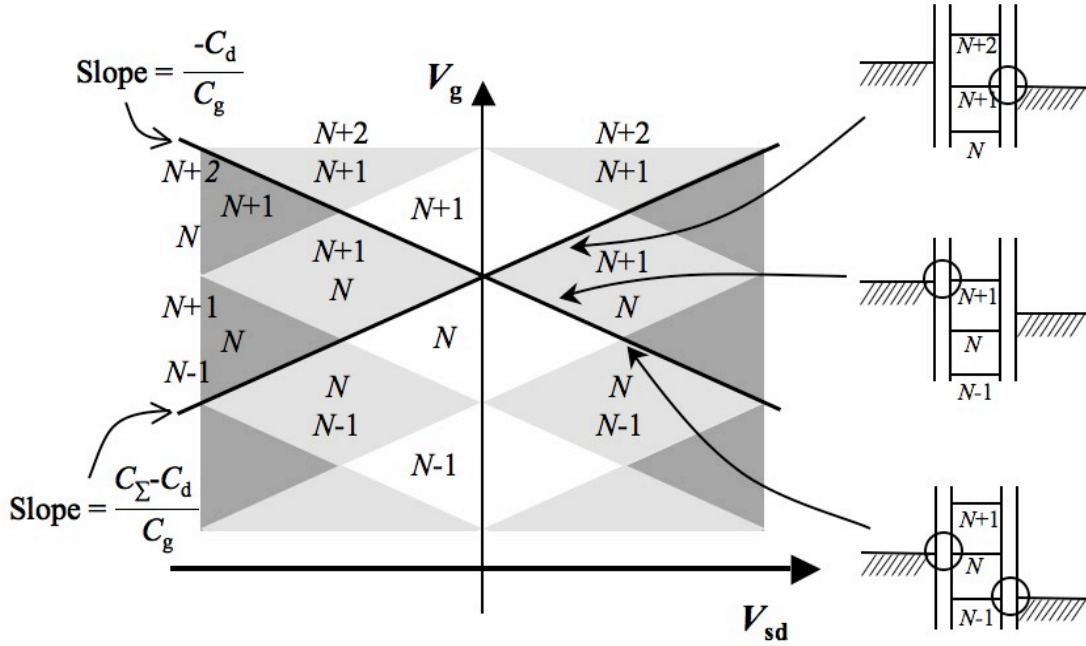


Figure 3.2.3 The tunneling spectrum of a QD system. The spectrum shows a diamond-like pattern and in each diamond there is a different charge configuration. The edge of the diamond represents the transport regime with high tunneling probability due to the alignment of the states of the dot with the Fermi level of either source or drain (shown in the right graphs). The different charge configurations are marked with different colors: white, gray and deep gray, and in each region the fluctuated numbers of the electrons in the dot are different.

eq. 3.13 the relation between ΔV_g and ΔV_{sd} is obtained accordingly:

$$\frac{\Delta V_g}{\Delta V_{sd}} = -\frac{C_d}{C_g}. \quad (3.14)$$

Similarly, the condition for the opened tunneling between the dot and the drain (the alignment between μ_d and μ_{QD}) can be also derived to show that the relation between ΔV_g and ΔV_{sd} is

$$\frac{\Delta V_g}{\Delta V_{sd}} = \frac{C_\Sigma - C_d}{C_g}. \quad (3.15)$$

If either the condition of eq. 3.14 or eq. 3.15 is fulfilled, the conductance of the system increases because of the increased tunneling probability. This results in a set of parallel lines with slopes of either $-C_d/C_g$ or $(C_\Sigma - C_d)/C_g$ when measuring the conductance as a

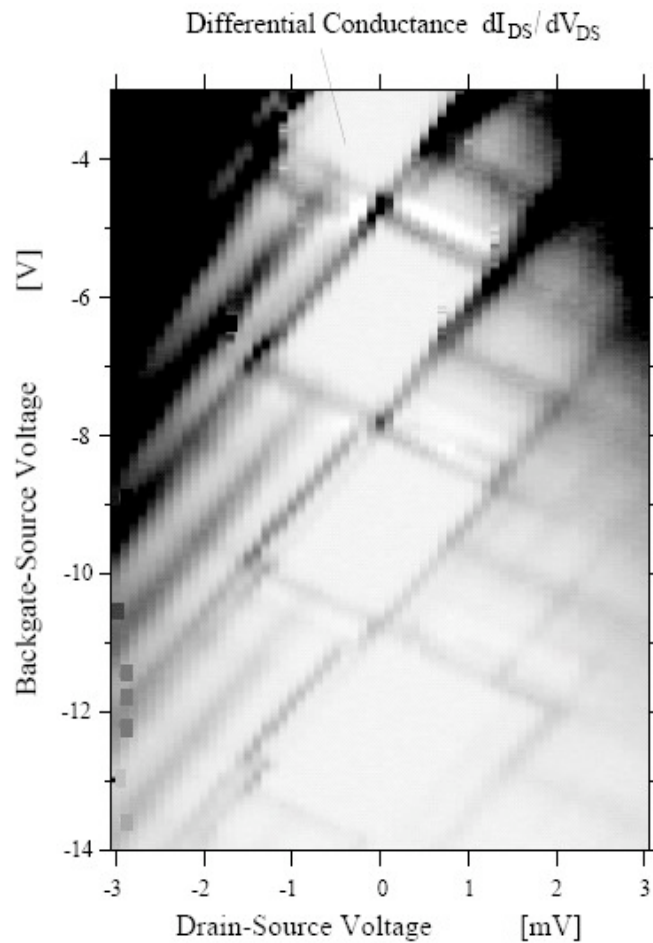


Figure 3.2.4 Stability diagram from a experimental measurement. The Coulomb diamonds near the zero bias and the excited states at higher source-drain voltage are clearly seen. Pictures adopted from [WHK].

function of V_{sd} and V_g simultaneously, as shown in Figure 3.2.3 (marked by two thick lines). The gray areas in Figure 3.2.3 represent the fluctuation of different numbers of electrons in the dot. Higher bias enables the electrons to fill the excited states with higher energy and leads to more possible configurations of the energy structures of the dot. The white diamond-like area in Figure 3.2.3 is the Coulomb blockade regime and is also called the *Coulomb diamonds*. The full spectroscopy of the ground and excited states plotted is called *stability diagram*, which can be, in reality, obtained by measuring the differential conductance dI/dV at different V_{sd} and V_g , as shown in Figure 3.2.4.

3.2.2 Quantum interference

When the length of a 1D channel is comparable to the phase relaxation length, the effect of the interference of electron waves becomes considerable. The interference can be constructive or destructive and hence results in a conductance variation because the absolute square of the amplitude of the wave function is the probability of the detection of the electrons. The amplified conductance of the 1D channel due to the constructive interference is similar to the vibration of the string wave, whose amplitude is larger as it interferes constructively.

When two electron reservoirs, e.g. metallic electrodes, connect to a QW, the narrow area at the junctions form barriers with limited transmission probability. Such a system can be modeled as a waveguide with two reflective interfaces at the two ends and has an optical counterpart: A transparent plate sandwiched by two mirrors. This is the so-called Fabry-Pérot interferometer.[Her] Figure 3.2.5a shows that when an electron wave (or an electromagnetic wave in the case of Fabry-Pérot interferometer) approaches the left interface, it will be partially reflected and partially transmitted. The transmitted wave then propagates through the plate to the right interface and is reflected/transmitted again. The reflected/transmitted waves will interfere with each other as well as other incoming waves. Since the total transmission, T , is the superposition of the multiple transmissions, T_1, T_2, \dots, T_n , it will increase if the superposition is a result of constructive interference. On the other hand, T drops if the interference is destructive. This process can be formulated as

$$T = \sum_{p=1}^n T_p = \frac{(1-R)^2}{1+R^2-2R\cos(\delta)}, \quad (3.16)$$

where T is the total transmission probability, T_p is the output wavelet at the right interface, δ is the phase difference between each succeeding reflection. By definition, the phase difference is

$$\delta = \frac{2\pi}{\lambda} 2nl\cos(\theta), \quad (3.17)$$

where the n is an integer number, λ is the wavelength, l is the length of the waveguide and θ is the incident angle. According to eq. 3.16 and 3.17, T reaches its maximum when $\cos(\delta)$ equals to 1 or, equivalently, $2nl\cos(\theta)$ is an integer number of the wavelength. Figure

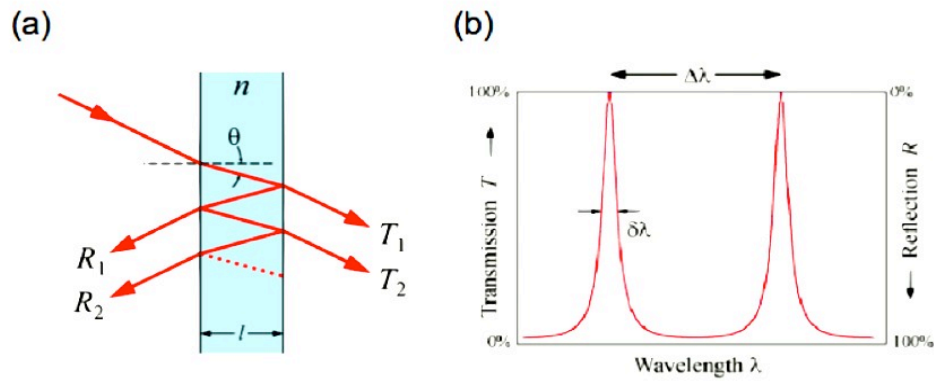


Figure 3.2.5 (a) A Fabry-Pérot interferometer consisting of two reflective mirrors. The incoming wave experiences multiple reflection and transmission at the two interfaces. (b) Transmission spectrum of the Fabry-Pérot interferometer. High transmission intensity is shown at certain wavelengths given the in-phase interference. (Picture adopted from [Wik])

3.2.5b shows a transmission spectrum of a Fabry-Pérot interferometer whose transmission intensity oscillates depending on the wavelength of the light wave. The high transmission rate in the spectrum occurs when the above condition is fulfilled.

3.2.3 Conductance quantization

For classical transport, electrons experience scatterings multiple times along their path through the material. The total resistance is the sum of the resistance produced by each scattering. However, when the system is in the ballistic regime, e.g. no scattering in the material, a fundamental question arises: what is the conductance of a transport channel without scattering? A conductor possessing this feature is called *ballistic* conductor.

Figure 3.2.6 illustrates the electrochemical potential profile of an 1D ballistic conductor sandwiched by two electrodes. The high electric potential of the left electrode drives the electron flow toward the right. Assuming that there is no reflection when the electrons enter the right electrode from the 1D conductor, the net current only has the contribution from those electrons with wave vectors $k > 0$ (going from the left to the right). Because of the energy quantization in the conductor due to its 1D geometry, electrons do not have infinite but limited choices of the transport channels, whose energy consist of discrete subbands, E_j . The total current I is then given by the sum of each subband current I_j , whose electrons have the energy $E_j(k)$ in the bias window $\mu_2 < E_j < \mu_1$. The subband current is

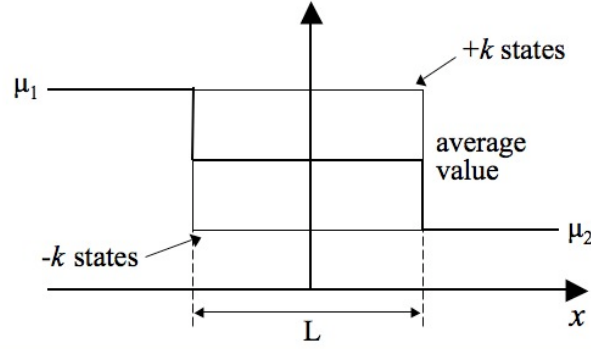


Figure 3.2.6 Variation of the electrochemical potential from one electrode, through a ballistic conductor, to another electrode. The k vector points to the direction of x . L is the length of the conductor. Note that the potential of the electrons is kept constant inside the conductor but changes only at the interfaces.

defined as $I_j = e/t_j$, where $t_j = L/v_j$ is the carrier transit time through the conductor, whose length is L . The group velocity v_j is, by definition, $\hbar^{-1}(\partial E/\partial k)$. If there are $2M$ spin-degenerate subbands in the 1D conductor, the total current can be calculated by

$$\begin{aligned}
 I &= \frac{e}{L} \cdot \frac{2L}{2\pi} \sum_j \int_{k>0} \frac{1}{\hbar} \frac{\partial E_j(k)}{\partial k} [f(E_j - \mu_1) - f(E_j - \mu_2)] dk \\
 &= \frac{2e}{h} \int [f(E - \mu_1) - f(E - \mu_2)] M(E) dE \\
 &= \frac{2e^2}{h} M \frac{(\mu_1 - \mu_2)}{e},
 \end{aligned} \tag{3.18}$$

where f is the Fermi function. The sum on k is converted to the integral with a spin degeneracy of two and the inverse of the level spacing $L/2\pi$. The result of eq. 3.18 has an universal constant: e^2/h , which is the conductance quantum. The total conductance of a ballistic conductor is therefore the number of the spin-degenerate subbands, $2M$, times the conductance quantum:

$$G_c = 2M G_0, G_0 = \frac{e^2}{h} = 38.7 \times 10^{-6} S, \tag{3.19}$$

As for the resistance:

$$R_c = R_0 \frac{1}{2M}, R_0 = \frac{h}{e^2} = 25.8 k \Omega, \tag{3.20}$$

The subscript c of G and R in eq. 3.19 and 3.20 represent ‘‘contact’’. This is because the

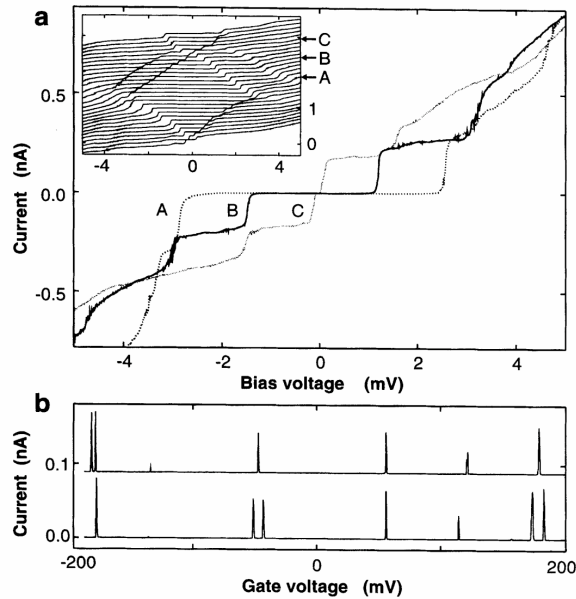


Figure 3.2.7 (a) I - V_{sd} curves of a SWNT device at temperature of 5 mK. The position of the plateaus is a function of gate voltage, as shown in the inset. Curve A, B and C mark the staircases at different gate voltage. (b) Current versus gate voltage. Between each peak are the Coulomb blockade regions. Two traces are shown with the measurement at different conditions. Pictures adopted from [TDD].

electrons dissipate no energy inside the ballistic conductor due to the lack of scatterings, but at the contacts, where the resistance arises (Figure 3.2.6), so that the total resistance has the most contributions from the contact. However, other factors like reflections at the contacts, inter-subband transport, quantum interference will cause deviations from the ideal model and result in additional resistance.[DAT] In the case of nanotubes, the theoretical resistant minimum is $R_0/2 = h/4e^2 = 6.4 \text{ k}\Omega$ because there are two subbands at the Fermi level.

3.2.4 Low-temperature transport in carbon nanotubes

The first study of the quantum transport of nanotubes was published on Ref[TDD], where an individual SWNT was laid on platinum electrodes, the same as the CNTFET structure shown in Figure 3.1.3. The degenerately doped Si/SiO₂ substrate serves as the gate electrode and the metal/CNT interface forms the tunneling barrier. Thus the CNTFET at low temperature imitates the QD system shown in Figure 3.2.1. The I - V_{sd} characteristics of the CNTQD are not linear but show staircase-like curves (Figure 3.2.7a). The positions of

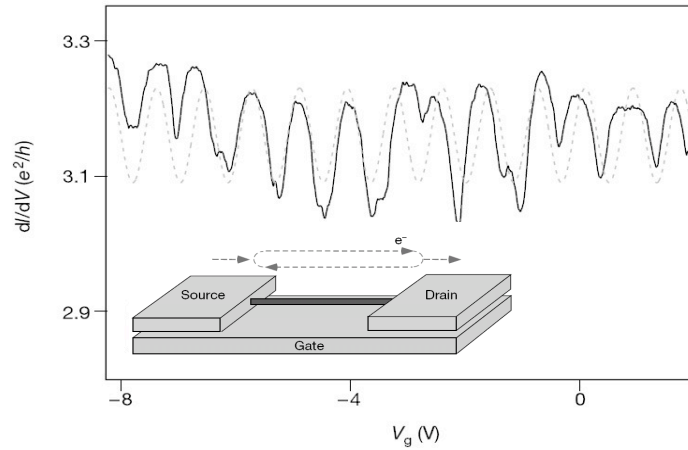


Figure 3.2.8 Differential conductance (dI/dV_{sd}) versus the gate voltage. Solid lines shows the measured curve that matches well with the sinusoidal function (dashed line) with the same period. The oscillated pattern is a result of the electron interference in the nanotube, as illustrated in the inset: schematic diagram of the multiple electron reflection. Pictures adopted from [LBB].

the current plateaus shift at various fixed gate voltage because the electrochemical potential of the SWNT is changed by V_g . While sweeping the gate voltage, conductance peaks due to the Coulomb blockade was observed. Therefore the transport behavior of the nanotube at low temperature resembles that of an SET.

In the Coulomb blockade regime, the transport mechanism at the metal/CNT interface is dominated by the quantum tunneling, giving the SET behaviors. However, when the tunneling barrier has smaller thickness or height, making the coupling of the electrode and the nanotube stronger, the electrons in the nanotube interfere with those in the electrodes. At the condition of strong coupling, the electrical transport is in the quantum interference regime and shows oscillating conductance as a function of gate voltage (Figure 3.2.8). [LBB][JGN] This is because the electron waves interfere, depending on the gate voltage, either constructively or destructively, and result in conductance maxima or minima respectively. The oscillating pattern of conductance recalls its optical counterpart shown in Figure 3.2.5. Another similar feature of the CNT waveguide is that the period of the oscillation is a function of the length of the nanotube.[LBB] This exactly corresponds to the theory shown in eq. 3.16: the phase difference depends on the length of the waveguide.

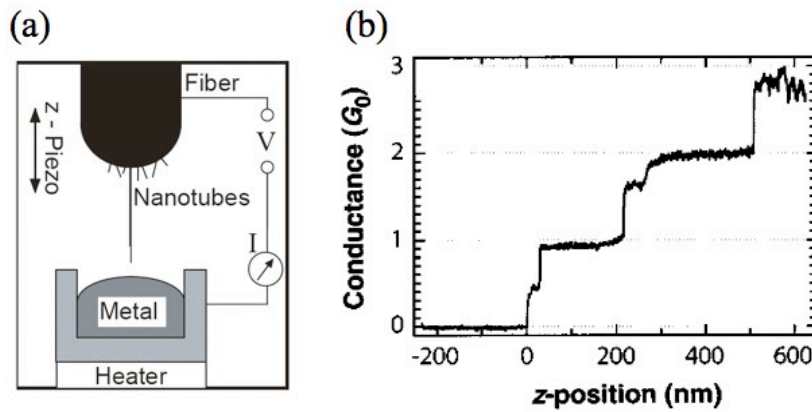


Figure 3.2.9 An experiment on ballistic transport in MWNTs. (a) Measurement set-up: An AFM tip attached with nanotubes is dipped into a liquid-metal-contact while its current flow is monitored with electrical devices. (b) Quantized conductance as a function of the z-position. The conductance is expressed in the unit of $G_0 = 2e^2/h$. Picture adopted from [FPW].

Ballistic transport in CNTs has been studied with various techniques. [LLL][FPW][JGW][KYT] Figure 3.2.9 demonstrates a measurement set-up with a MWNT bundle attached to a scanning-probe-microscopy (SPM) tip and inserted into a liquid-metal bath. During the insertion of the MWNT bundle, a trace of conductance with discrete increments was observed. It was found that the conductance increases because there is another MWNT among the bundle contacting the liquid metal while lowering down the tip. The increment resulting from the additional nanotube has the amount of G_0 and is therefore an evidence of ballistic transport. Another experiment employed the CNTFET to study the ballistic behavior, as shown in Figure 3.2.10. The CNTFET has palladium as the ohmic contact to reduce the contact resistance by lowering the Schottky barrier. As the contact resistance is closed to the quantum limit, R_0 , it was observed that the ON-state conductance, G_{ON} , of the transistor increases as the temperature decreases (Figure 3.2.10). This feature shows the ballistic transport in semiconducting nanotubes.

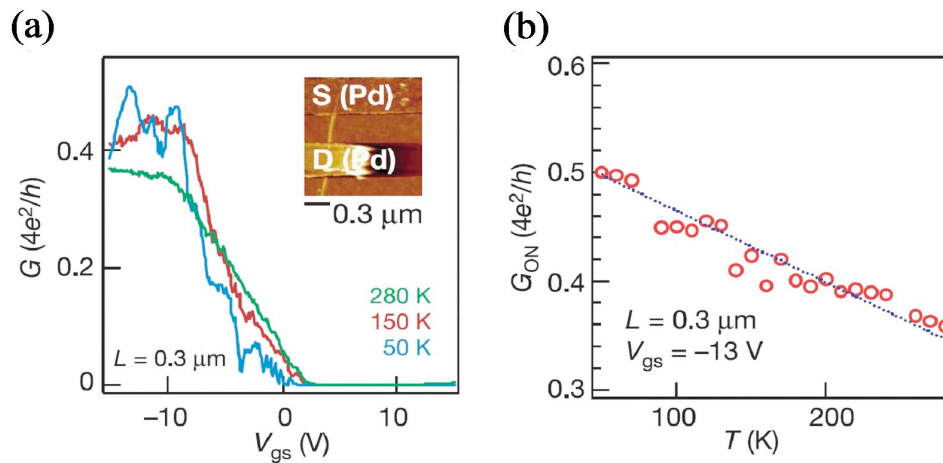


Figure 3.2.10 Ballistic transport in semiconducting SWNTs with source and drain electrodes made by palladium. (a) linear conductance versus gate voltage at various temperatures. (b) temperature dependence of the GON of the ballistic CNTFET. Picture adopted from [JGW].

3.3 Spin transport in carbon nanotubes

3.3.1 Introduction to spintronics

The employment of the electron spin as the information carrier is the central concept of spintronics.[WAB] Unlike conventional electronics, which controls electronic charges, the operation of spintronic devices is based on the manipulation of the electronic spin. There are three requirements for an applicable spintronic device: (1) generation, (2) transportation and (3) detection of the spin information.[ZFS] These goals can be achieved by manipulating the population and the phase of an ensemble of electron spin or building a single/few-spin system. In the development of spintronics, the magnetic tunneling junction (MTJ) is a milestone.[BBF][BGS] MTJs have been used as main component of a magnetic sensor, the read head of a hard disk drive, the galvanic isolator and the magnetoresistive random access memory (MRAM). The operation mechanism of the MTJ is based on the so-called giant magnetoresistive effect (GMR) or the spin-valve effect. The discovery of this effect is considered as the birth of spintronics and its scientific and economic impact

have been acknowledged so generally that its two discoverers, Peter Grünberg and Albert Fert, were both awarded with Nobel prize in 2007.[Nob]

The spin-valve effect is a result of the manipulation of an ensemble of electron spins. Its fundamental mechanism is based on the spin-dependent band structure of the transition metal proposed by Mott in 1936.[Kit] Mott suggested that the DOS of a transition metal is asymmetrical for spin-up and spin-down states when it is magnetized (Figure 3.3.1a). Consequently, the electrons with different spin have different population at the Fermi level. Given that the electrons at the Fermi level contribute the most to the electrical current, the electron transport of a magnetized transition metal is *spin-polarized*: one of the two spin states dominates the conductive electron ensemble. The degree of the spin polarization P is then defined as

$$P = \frac{N_{ma} - N_{mi}}{N_{ma} + N_{mi}}, \quad (3.21)$$

where the N_{ma} and N_{mi} are the DOS at the Fermi energy of the majority and minority spin respectively. When two transition metals (or other conductive ferromagnets) are separated by a nonferromagnetic conductor or a tunneling barrier, (Figure 3.3.1b and c), the resistance varies according to the magnetized direction of the ferromagnets. Two different cases are shown in Figure 3.3.1d: (1) parallel or (2) antiparallel magnetization. When the two ferromagnets are magnetized in parallel, the electrons with majority spin find available states in both sides more than the those with minority spin do. This results in a low-resistance state because most of the electrons are not scattered as being transported through the junction. In the other case, because the magnetization is antiparallel, both of the electrons with majority and minority spin in one of the ferromagnets can hardly find available states in the other side. Therefore to they have to flip their spin via scattering when going through the junction and hence dissipate their energy. This results in a high-resistance state. Figure 3.3.1e shows a typical measurement results of the MTJ, where the resistance is lower at higher magnetic field (parallel magnetization) but higher near the zero field (antiparallel magnetization). Thus the three criteria of a spintronic devices, mentioned at the beginning of this section, are fulfilled by the MTJ: the spin states is controlled by the magnetic field; the spin is transported coherently through the

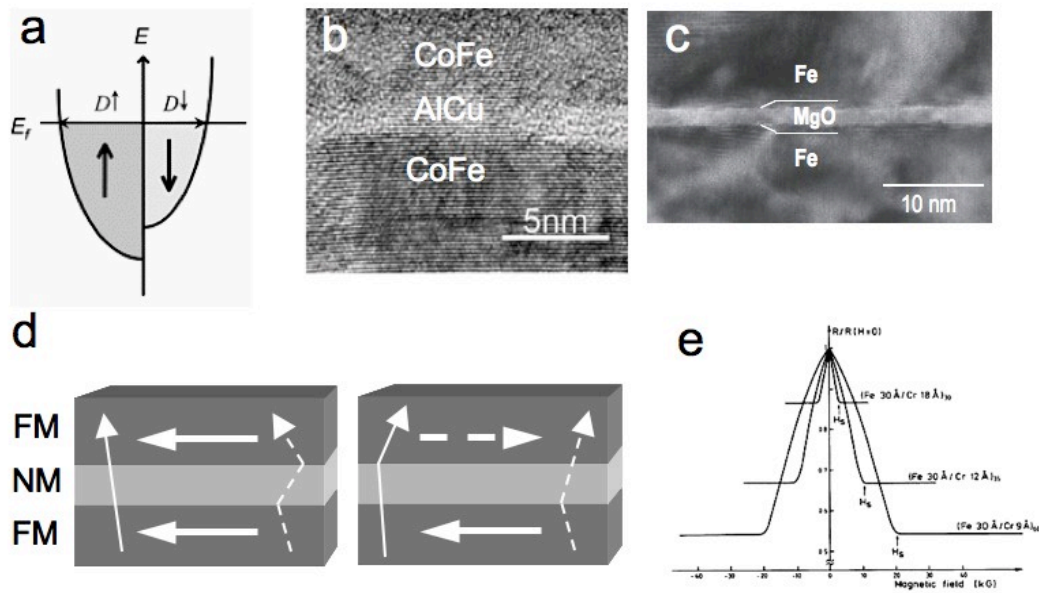


Figure 3.3.1 (a) DOS of the ferromagnetic materials based on Mott's model. (b) A GMR device with metallic AlCu as the nonferromagnetic conductor.[NIM] (c) A spin valve device with insulating MgO as tunneling barrier.[YNF] (d) Schematic diagram illustrating the transport model of the GMR effect. (f) Experimental data of the GMR effects from devices using Cr as the nonferromagnetic layer. It was observed that thinner Cr gives larger GMR. Picture adopted from [BBF].

nonferromagnetic layer; the spin state is discriminated via the device resistance.

Although the MTJ has been used for many applications, other spintronic devices, e.g. spin field-effect transistor (SpinFET),[DD] have not yet succeeded in fulfilling all of the three criteria for application. Challenges still exist and further improvement is needed. For the generation of spin information, using the transition metals to generate the spin-polarized electrons is not the most efficient way due to their limited degree of polarization. Several new materials and new approaches have been adopted to increase the polarization. and the results show that a almost 100%-polarized system is possible. New materials like GaMnAs, CrO₂ and La_{1-x}Sr_xMnO₃ possess almost 100%-polarized electrons at the Fermi level as they are magnetized.[OSM][WG][WWM] Highly efficient MTJs made by these materials have been demonstrated.[RGJ] However, issues like scalable production, process integration and so on require more studies. Other approaches like optical polarization or employing the so-called *Spin Hall effect* also induce high degree of polarized electrons.

[DP][Hir][KMG][VT] But most of the approaches are still under study.

After the issue of spin generation, follows the question “how to transport the spin coherently?” In the case of MTJs, the spin state is transported through the nonferromagnetic layer of only a few nm, where the spin coherence is kept. However, such a distance is too short to extend its applications in other functional devices. If a system cannot preserve the spin coherency within a reasonable time or distance, it fails to keep the information. There are several factors causing spin relaxation in solids. Defects and phonons are two common factors for spin relaxation. Their influence can be reduced by the use of single crystals and performing the operation at low temperature. Another cause of the spin relaxation is the spin-orbit interaction induced by the ions and the hyperfine interaction. These issues specially concern the single or few-spin systems.

The last challenge for spintronics is the methodology to read out the spin information. Unlike the electrical signals that can be detected directly by an ammeter or a voltmeter, so far the spin signals are detected indirectly via either optical or electrical means. The optical method is based on the *magneto-optic Kerr effect* (MOKE), which describes the interaction between the polarization of light and the electron spin. Therefore one can detect the spin state by sending light to a sample and comparing the polarization of the reflected light and that of the original one and hence obtain the information about the spin state of the sample. [KMG] The electrical method is to measure the magnetoresistance (MR) or the voltage induced by spin accumulation. Both methods transform the spin signals into electrical ones. The MR method has the same concept as the spin-valve effect does, measuring the field-dependent resistance to differentiate the spin states. As for the spin-accumulation, a technique called non-local measurement is utilized to generate electron accumulation that is spin-dependent and can be probed by measuring the voltage generated therefrom. [JS] [JFW]

3.3.2 Spin transport in carbon-related materials

Carbon-based materials are suggested to be promising for spin transport because of the weak spin-orbit interaction and the absence of a nuclear spin for the ^{12}C atom. Consequently the spin coherence time is expected to be long. Spin-transport experiments on various carbon-based materials have been carried out, including pure carbon materials

like CNTs[TAA][SKF][JHN] and graphene[HGN][TJP][CCF], conjugated molecules like 8-hydroxy-quinoline aluminium (Alq3)[XWV] and sexithienyl (T6)[DMM], self-assembled monolayer (SAM) like octanethiol and 1,4-benzene-dithiolate (BDT)[WHL]. Results show that the spin coherence length of these materials can be scaled up to μm , supporting the idea to build carbon-based spintronics.[TJP]

Although these carbon-based materials show very positive results in terms of spin coherency, issues like the instability under ambient conditions as well as the integration with the inorganic system are still open questions to be solved. Among the various materials, CNT and graphene attract the most attention for their special geometry and size

3.3.3 Spin transport in carbon nanotubes

To study the spin transport through nanotubes, the device structure of CNTFET is applicable, as shown in the inset of Figure 3.3.2a, where a SWNT is contacted by two ferromagnetic electrodes. This structure is able to send a spin-polarized current into the nanotube from one ferromagnetic contact and to detect the spin state of the output current by the other one. The working principle of this device is the same as that of MTJs. But comparing with MTJs, the spin-polarized electrons travel a much longer distance in the CNT. Results from the CNT device show clear spin-valve effect (Figure 3.3.2a), indicating that the spin coherence is indeed preserved through hundreds of nm (the distance between the two electrodes). To the best of my knowledge, the largest spin coherent length reported so far in CNT is $1 \mu\text{m}$ and the highest temperature, at which the spin-valve effect is still observable, is 120 K.[HPF]

The uniqueness of CNT for spin transport experiments is its tunable gate property. It enables the study of the coherent single spin transport because at low temperature one can control the current in the CNT down to single electron level. As shown in Figure 3.3.2b, the Coulomb peaks were observed in the SWNT with PdNi contacts, a proof of the single-electron transport. The spin-valve effect measured in the same regime showed that MR also oscillates. Further analysis suggests that MR oscillates depending on whether the Fermi level of the nanotube aligns with that of PdNi. The oscillation of MR was then explained by the resonant tunneling in a QD system. In the case of misalignment, the electrons goes through the nanotube by direct tunneling and the whole device mimic the

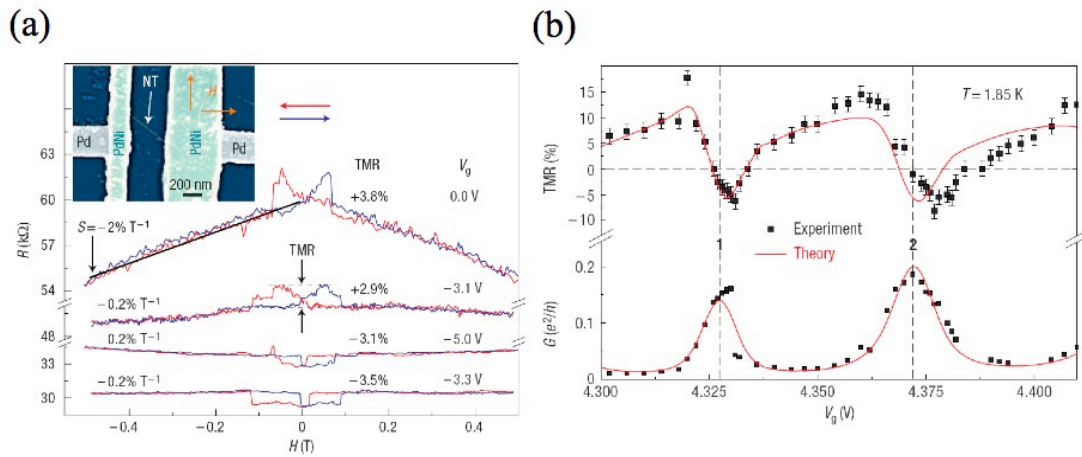


Figure 3.3.2 (a) Experimental results from a spin-valve device using nanotube as the nonferromagnetic conductor. It was found that the gate voltage influences the MR. Inset: the device image. (b) The variation of the MR according to the gate voltage. Comparing with the conductance, G , at the same voltage scale, the positions where MR shows dips at the gate voltage where there are Coulomb peaks. Picture adopted from [STF].

MTJ. Therefore positive MR (higher resistance at smaller field) was observed. On the other hand, when the Fermi level of the SWNT aligns with that of PdNi, the tunneling rate is larger and the CNTQD resonates with the leads. In such condition, anomalous negative MR appears (lower resistance at smaller field). The sign change of MR at single electron level shows that the nanotube is indeed able to manipulate the electron spin down to single spin level.

However, even it has been shown that the CNT can transport spin up to a distance of 1 μm , the efficiency of a working CNT spin valve is usually low. It implicates that there is spin relaxation in the CNT devices. In the F-CNT-F junction (F: ferromagnet), there are two places, which could relax the spin: (1) the interfaces between the ferromagnet and nanotube; (2) the body of the nanotubes. For the interface, it has been proved that the ferromagnet/nonferromagnet interface limits the efficiency of the spin injection due to the resistance mismatch.[ZFS] The resistance mismatch originates from the different DOS structures in the ferromagnet and nonferromagnet. The former has an asymmetric DOS for spin-up and spin-down but the later has a symmetric structure. To overcome this problem, interface engineering is necessary. As for the relaxation in the body of the CNTs, the spin-orbit interaction should not be a serious issue because the split-off energy of the CNT

caused by the spin-orbit interaction is 0.37 meV,[KIR] which is much weaker than that of conventional semiconductors, GaAs (330 meV) and Si (44 meV). However, the extrinsic sources like impurity scattering may play an important role in flipping the spin. It has been reported that shortening of the distance between the two ferromagnetic leads decreases the number of defects along the CNT body, and hence increases the yield of working devices. [NBS] Nevertheless, effort is still needed to find out the cause of the spin relaxation and to improve the performance.

Chapter 4

Carbon Nanotube Electronics with Different Contact Configurations

4.1 Introduction

The transport characteristics of the CNTFET strongly depend on the electrodes due to the different chemical and electrical properties of the metals, resulting in different contact resistance, transistor polarity, etc. Consequently the choice of the contact metals is important when employing the nanotubes for different applications. In this chapter, results of the electrical characterization of the devices with various metal contacts are presented. Two different types of devices will be discussed: Devices (1) with symmetrical contacts and (2) with asymmetrical contacts. The symmetrically contacted devices are those with two electrodes made by the same metal. As for the asymmetrically contacted ones, different metals are used as the source and drain electrodes.

4.2 Materials and methods

Laser ablated single-walled carbon nanotubes (SWNTs), commercially available from SINEUROP Nanotech GmbH, are used to make the devices. The process begun with suspending the SWNTs in 1% aqueous solution of sodium dodecyl sulfate (SDS) and then transferring the nanotubes onto a p-doped Si substrate, which has 200-nm-thick thermally oxidized SiO₂ layer and serves as the back-gate electrode. Samples were rinsed in deionized water to remove the SDS molecules on the nanotube after transferring. Electron-beam lithography was applied to pattern the electrodes after locating the nanotubes by atomic force microscopy (AFM) according to the metal markers. Measurements of the devices are carried out at both room temperature and low temperature (4.2 K). More details

about the device fabrication and the measurement set-up are given in Appendix A.

4.3 CNT with symmetrical contacts

Two types of symmetrically contacted devices were tested and compared. One is made of AuPd electrodes and the other one uses aluminum. Figure 4.3.1a shows the I - V_{sd} curves of a semiconducting nanotube with AuPd contacts. These curves have a linear feature, which is the same as the results from the samples with aluminum as electrode. However, the device resistance is found to be larger at negative gate voltage for the samples with AuPd contacts while it is larger at positive gate voltage for those with Al contacts. The gate responses corresponding to each one are shown in Figure 4.3.1b, where the different polarities of the CNTFET with different contact metals are clearly shown. Therefore the AuPd-contacted device behaves like a p-type FET while the Al-contacted one is n-type. These features were found reproducibly in both AuPd- and Al-contacted nanotubes. In some cases, ambipolar behaviors were also observed, though rarely, when the tested nanotube has small bandgap (inset of Figure 4.3.1b). The on/off ratio of the CNTFETs with

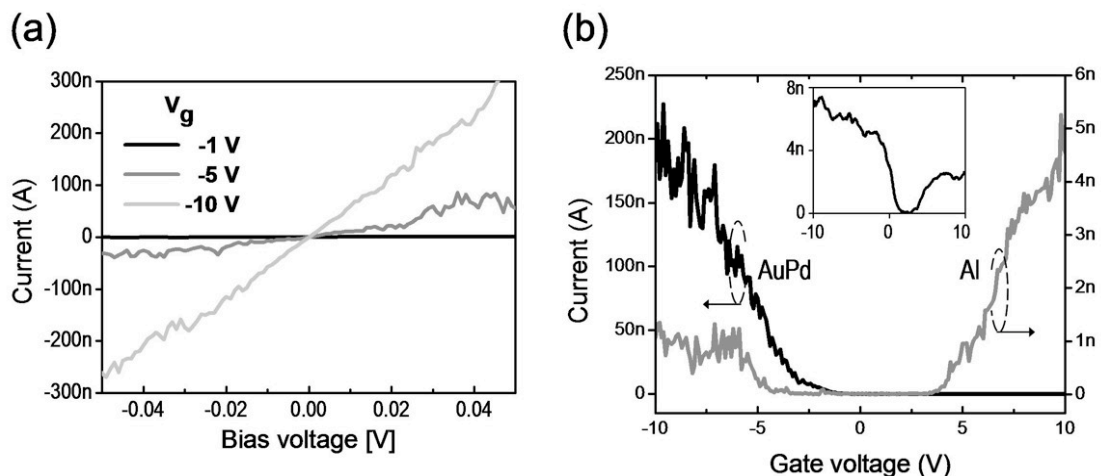


Figure 4.3.1 (a) I - V_{sd} curves of a CNTFET with AuPd contacts at different gate voltage. (b) Gate responses from semiconducting nanotubes with AuPd and Al contacts. The former shows a p-type behavior ($V_{sd} = 50$ mV) while the later is a n-type transistor ($V_{sd} = 1$ V). Inset: Gate response from a small bandgap nanotube, which is conductive at both positive and negative gate voltages.

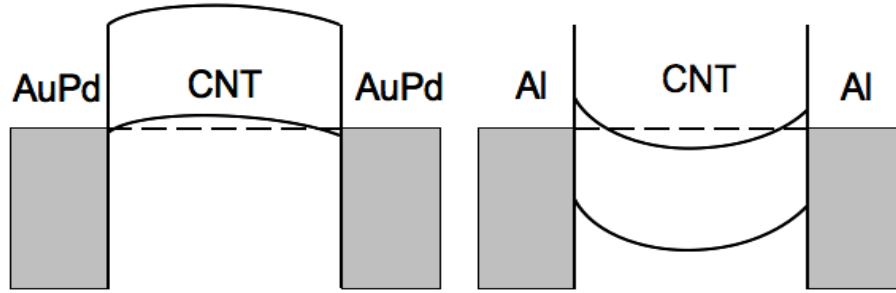


Figure 4.3.2 Schottky barrier model for the metal/CNT interface. Contacts between AuPd and nanotubes is nearly ohmic due to its high work function while Schottky barrier forms at the Al/SWNT interface.

AuPd contacts is 10^5 and with Al contacts is 10^3 . The device resistance depends on the metal contacts as well. In general, the contact resistance of the devices with AuPd leads is in the range of tens to hundreds of $k\Omega$ but is about tens to hundreds of $M\Omega$ for the Al-contacted ones. Two factors are the main causes of this difference: the Schottky barrier at the CNT/metal interface as well as the wettability of the metals. The former concerns the semiconducting nanotubes only while the latter is effective both to the metallic and semiconducting ones. Metals with high work function like Au or Pd show nearly ohmic hole-transport through the CNT/metal interfaces due to the alignment of their Fermi level with the valence band of the nanotubes. Since the work function of Al ($\Phi_{Al} = 4.1$ eV) is smaller than that of AuPd ($\Phi_{AuPd} = 5.4$ eV), the Schottky barrier forming at the CNT/Al interface impedes the holes and shows electron-transport with larger resistance. Figure 4.3.2 illustrates the Schottky barrier model to explain the different transport behaviors of the CNTFETs with different contacts. Results from the room-temperature characterization of the CNTFET show that all types of transistors (n-type, p-type or ambipolar) can be made by using different metals as the electrodes. The accessibility of the CNT to multifunctional transistors is important to build a CNT-based complementary circuit system. Furthermore, the relatively poor wettability of the aluminum, comparing with Pd, on the nanotubes has been reported. As shown in Error: Reference source not found, when Pd is deposited on an suspended CNT, it forms a continuous film on the CNT walls. However, Al tends to form discrete particles. This helps to explain the unstable and relatively high contact resistance observed in Al-contacted nanotube devices.

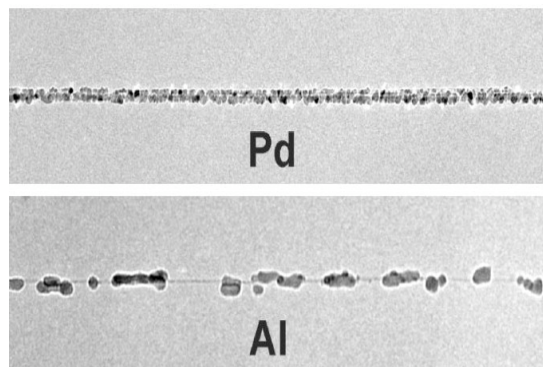


Figure 4.3.3 Deposition of metals on suspended SWNTs. Palladium tends to form a continuous thin film on the nanotube while segregation of clusters is formed for aluminum due to its poor wettability. Picture adopted from [ZFC].

Nanotubes with small bandgap are further characterized at low temperature for the study of different transport regimes, which can be achieved by controlling the Schottky barrier to vary the transparency of the contacts via the gate electrode. The device with its room-temperature $I-V_g$ curve shown in the inset of Figure 4.3.1b was studied at 4.2 K with the results shown in Figure 4.3.4a. A non-conducting region was observed near the zero gate voltage, showing the semiconducting gap of this tube. The Coulomb blockade regime evolves when the gate voltage is larger than 0.8 V, at which the Schottky barrier is reduced and electrons are not prohibited to tunnel into the nanotube. The structure of the Coulomb diamond is shown in Figure 4.3.4b, where the SET behavior is clearly observed. While increasing the gate voltage further, the device enters a transition region where the differential conductance shows sharp oscillations. This is because the Schottky barrier, as shown in Figure 4.3.4c, is thinned due to the strong bending of the electron bands of the nanotube. When the gate voltage is above 6 V, the Schottky barrier perishes and the CNT/metal interface becomes transparent, resulting in a transport pattern of Fabry-Pérot interference. The evolution of the transport regime shows that by changing the gate voltage, semiconducting nanotube can function either as a single-electron transistor or as an 1D electron waveguide. In addition, a so-called negative differential conductance (NDC) was observed in the Fabry-Pérot regime (Figure 4.3.4d), where the current decreases while increasing the bias voltage. Since the stability diagram represents the tunneling spectroscopy of a system and the dI/dV represents the electron tunneling rate in different regimes, the NDC can then be ascribed to the weak link of some states in the

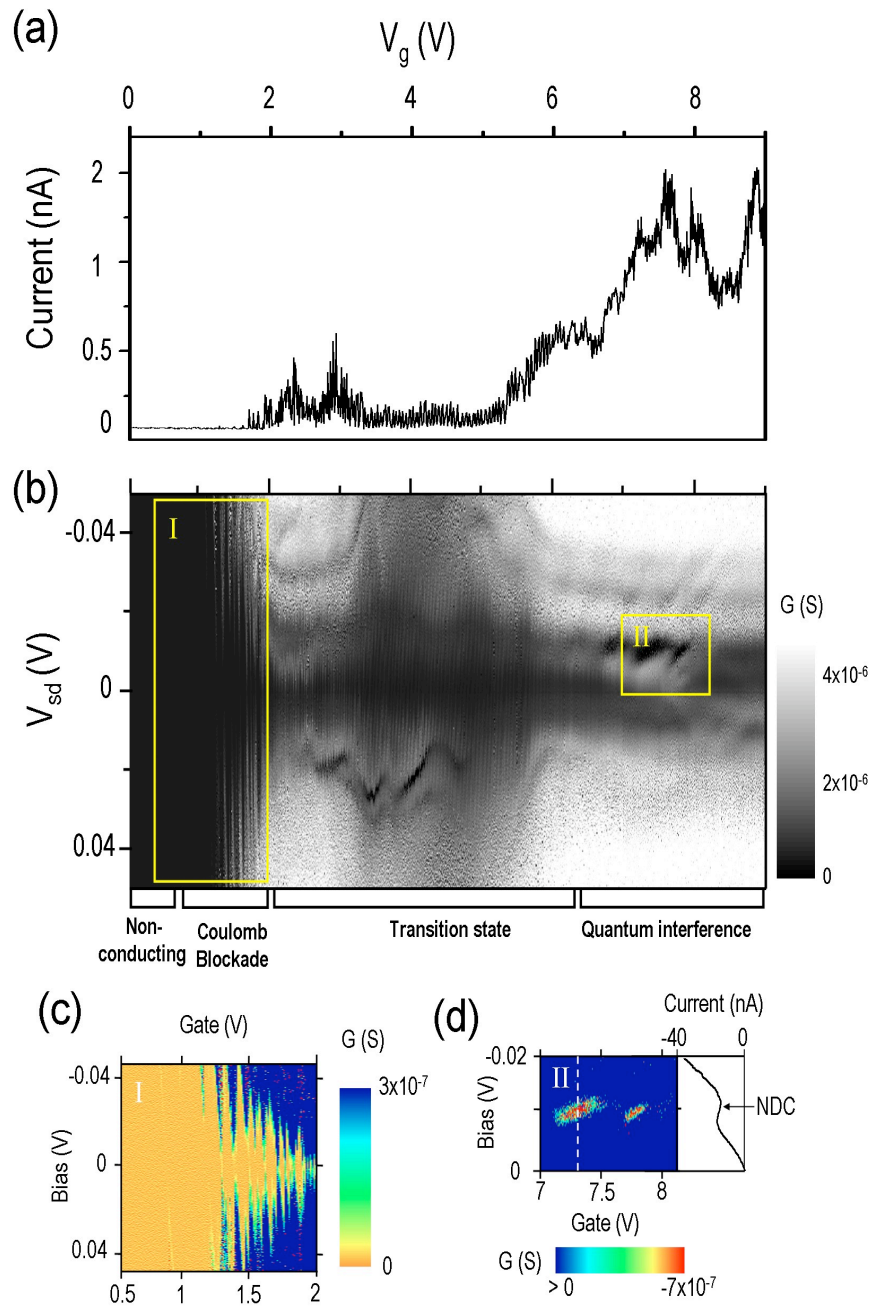


Figure 4.3.4 (a) Current versus gate voltage in the small bandgap nanotube. (b) The stability diagram in the same range of the gate voltage. The evolution of the each transport regime is indicated. (c) A zoom-in of region I, marked by the left rectangle in (b). Coulomb diamonds evolving from the non-conducting region are shown. (d) Zoom-in of the region II marked in (b). The negative differential conductance (NDC) in the quantum interference regime is clearly shown. An I - V_{sd} curve in the NDC region (marked with the dashed line) is shown.

nanotube to the electrodes.[SMB] This also explains the dependence of the NDC on the gate voltage, by which these weakly linked states are tuned.

4.4 CNT with asymmetrical contacts

A nanotube device with asymmetrical contacts is sketched in the inset of Figure 4.4.1, in which two different electrodes (AuPd and Ti) are used. Results of the current-voltage characteristics from three similar devices are shown in Figure 4.4.1. Robust rectifying characteristics were observed in all of these devices, which behaved very differently from those CNTFET made with symmetrical contacts. Current increases dramatically when a positive bias is applied to the AuPd contact (forward bias regime) but is blocked as the bias turns to be negative (reverse bias regime). The threshold voltage is about 0.1 V for device #2 and #3, and is much smaller for device #1. All of the asymmetrically contacted CNTFETs show a p-type behavior in their gate responses: current increases with negative gate voltage but is suppressed at positive gate voltage. A representative result from device #2 is shown in Figure 4.4.2. The Schottky barrier model discussed in section 4.3 can explain the p-type rectifying behavior of the asymmetrically contacted nanotubes. AuPd and Ti form different Schottky barrier at the metal/CNT interfaces due to their different work function ($\Phi_{\text{AuPd}} = 5.4$ eV, $\Phi_{\text{Ti}} = 4.3$ eV). The high work function of AuPd makes its contact with nanotube ohmic, so the total energy barrier seen by the *holes* can be then approximated as the sum of the Schottky barrier at the Ti/CNT contact and the bias voltage, $\Phi_{\text{Ti}} + eV_{\text{sd}}$. Therefore

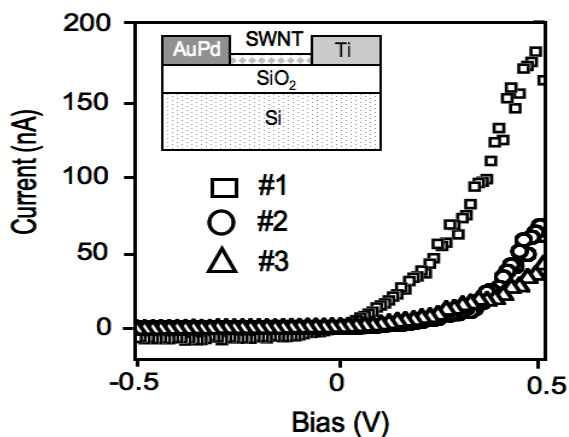


Figure 4.4.1 I - V_{sd} curves ($V_g = 0$) of three nanotubes with asymmetrical contacts: AuPd and Ti. A schematic diagram illustrating the device is shown in the inset. All of the three devices exhibits high conduction as the bias on AuPd is positive.

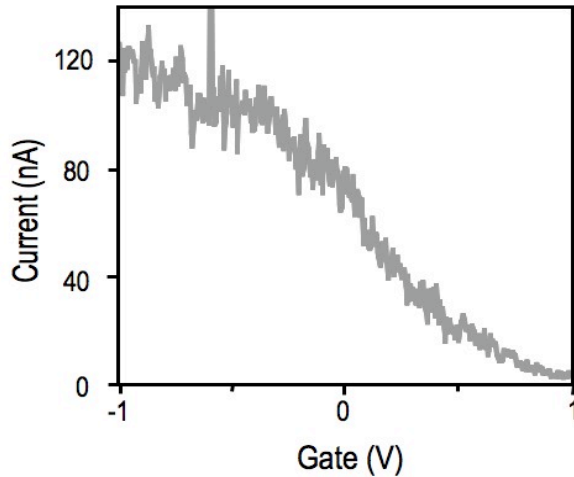


Figure 4.4.2 Current versus gate voltage ($V_{sd} = 0.5$ V). A p-type transistor behavior is observed.

changing the source-drain voltage simultaneously modifies the energy barrier, which is then either reduced or increased by biasing the Pd electrode positively or negatively (see the illustration of Figure 4.4.3). This gives the observed rectifying behavior. Thus a nanotube with asymmetrical contacts functions as a Schottky diode (CNTSD). However, other than the conventional thin-film diode is the additional gate-tunability of the CNTSD, which enable it to serve as an alternative electronic element. It should be emphasized that the rectifying current is only observed in the semiconducting nanotubes with asymmetrical contacts. For the metallic ones, they still showed ohmic transport when the electrodes are asymmetric.

The CNTSDs have also been characterized at low temperature. At 4.2 K the $I-V_{sd}$ curve of device #2 shows a clear stepwise structure in both forward and reverse bias regions (Figure 4.4.4). This is the so-called *Coulomb staircase*, a typical feature of a quantum dot with asymmetrical tunneling barriers.[KAT] Because of the high tunneling rate at the AuPd/CNT transparent contact, the electrochemical potential of the nanotube is mainly controlled by AuPd due to its strong coupling with the CNT. Therefore the energy states of the nanotube move up or down along with the Fermi level of the AuPd lead, and the nanotube is fast charged or discharged by the AuPd electrode. The blockage of the current flow is mainly at the Ti/CNT interface, where the Schottky barrier is higher and thicker. The tunneling of the electrons through this barrier requires a voltage threshold so that no current at the vicinity of the zero bias is observed. When the bias voltage is large enough for the electrons to tunnel through the barrier and, at the same time, there is an available

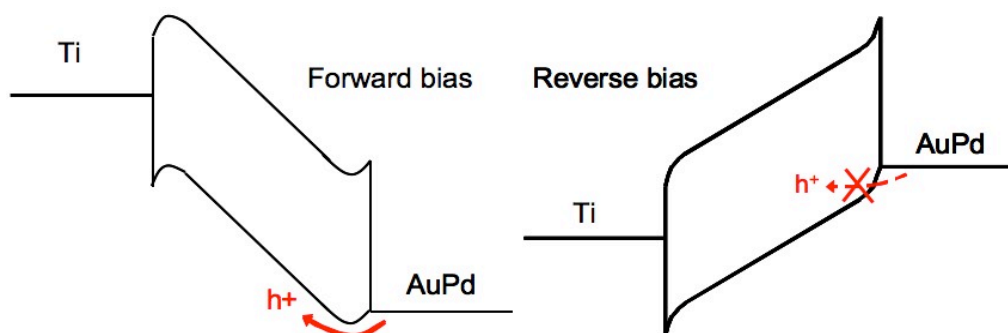


Figure 4.4.3 Mechanism of the rectifying transport of the asymmetrically contacted nanotube. At the interfaces of Ti/CNT, holes see a larger Schottky barrier than they do at AuPd/CNT.

state in the nanotube within the bias window, the tunneling probability at the Ti/CNT largely increases, resulting in a sharp increase of the current. Further increase of voltage will not induce more current until a new energy state is added to the bias window, causing the current plateau between two sharp increments. Interestingly, features of the Coulomb staircase is also observable in the CNTSD at high temperature. Figure 4.4.5 and Figure 4.4.6 show the I - V_{sd} curves taken from 4.2 K up to room temperature at forward and reversed bias regimes respectively. The Coulomb staircase is still visible up to 120 K in the forward-bias region and 250 K in the reverse-bias region. The stepwise curve is smeared at higher temperatures because the thermal energy acquired by the electrons is large enough to overcome the Coulomb blockade.

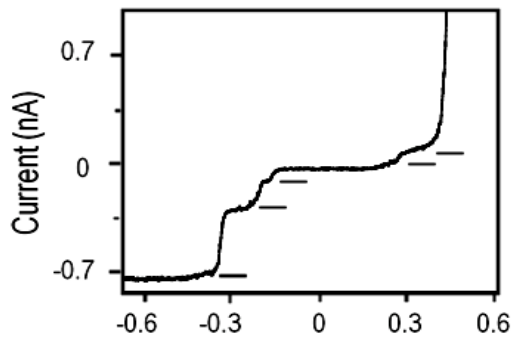


Figure 4.4.4 $I-V_{sd}$ curve of an asymmetrically contacted nanotube (device #2) shows a stepwise structure (marked by strokes) at 4.2 K.

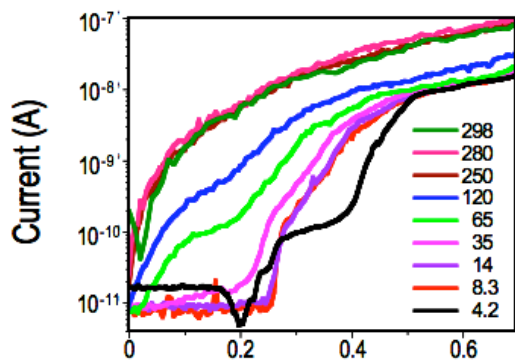


Figure 4.4.5 $I-V_{sd}$ curves of device #2 at forward bias at various temperatures.

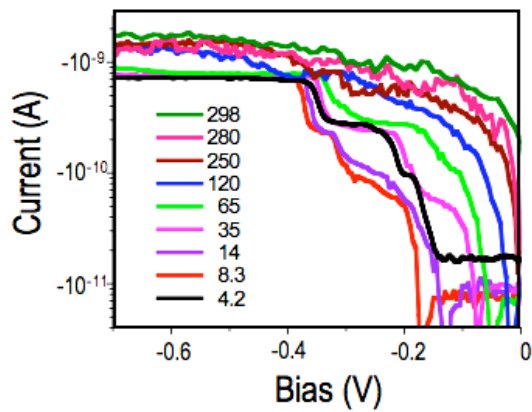


Figure 4.4.6 $I-V_{sd}$ curves of device #2 at reverse bias at various temperatures.

4.5 Conclusions

Individual nanotubes contacted with different metals were characterized at room temperature and liquid Helium temperature. Devices of symmetrical and asymmetrical contacts were both made. AuPd and Al are used for the study of the devices with symmetrical contacts. It is found that AuPd forms a transparent metal/CNT interface, reducing the device resistance down to tens of $k\Omega$. But the devices with Al contacts often show $M\Omega$ resistance. This is due to the poor wetability of Al on nanotubes as well as the high Schottky barrier at the Al/CNT contacts. Semiconducting nanotubes with the AuPd electrodes show a p-type transistor behavior but the Al-contacted ones have a n-type transistor. When the device consists of a small band-gap nanotube, it shows an ambipolar behavior. A device made of a small band-gap nanotube demonstrates a change in transport property by controlling the transparency of the Schottky barrier. At low gate voltage, Coulomb diamonds show because the tunneling mechanism dominates the transport, while at large gate voltage a Fabry-Pérot pattern appears, resulting from the interference of electron waves. In the devices with asymmetrical contacts, AuPd and Ti is used as source and drain electrodes respectively. These devices show strong current rectification. This is because the Schottky barrier at the Ti/CNT interface is larger than the AuPd/CNT interface. At low temperature, the asymmetrical barriers form asymmetrical tunneling barriers, leading to a pronounced Coulomb staircase in the $I-V_{sd}$ characteristics. The stepwise feature disappears at temperatures higher than 120 K in the forward bias region but remains observable at the reverse bias up to 250 K.

Chapter 5

Semiconductor/Carbon Nanotube Heterojunction

5.1 Introduction

Interfaces play an important role in nanotechnology. For the mechanical, chemical, electrical, or biological properties of a system consisting of both macro- and microscale materials, the interface is often a determinant factor.[Sur][ABC][MUG] When applying nanotechnology as a tool for cross discipline research, knowledge of the interface is essential.[PTZ] Carbon nanotube (CNT), as a prototype nanomaterial, is not an exception either. To develop CNT electronics research from science to technology, detailed information about the electrical characteristics of the interfaces between nanotubes and other materials is not trivial. Most of the CNT-based electronics nowadays are built with metallic contacts, where the nanotube/metal interfaces have been discussed in the previous chapter. But from the history of the semiconductor industry, people have learned that semiconductor heterostructures have a very wide range of applications, e.g., high-speed computation, solar cells, and high-frequency communication. However, due to the extreme size of nanotubes and the limited applicable process technologies, often it is difficult to contact a single nanotube with other materials to investigate their interfaces (except metal, which can be made by evaporator.) Confronted by this issue, we have designed a simple structure for the study of heterojunctions between semiconductor (GaAs) and nanotubes. GaAs is selected because of its well-developed industrial application and better, compared with Si, electrical performance in certain aspects like higher carrier mobility.

5.2 Materials and methods

Figure 5.3.1a shows the prototype of the GaAs/SWNT heterojunction. A SWNT lies on a highly doped GaAs substrate with an end isolated by a thin insulating layer. The sample preparation began with chips ($4 \times 4 \text{ mm}^2$) sliced from a GaAs wafer, which was pre-patterned with metal markers by e-beam lithography. Substrates were then half-covered with thermally evaporated SiO_2 (100 nm) via optical lithography. Laser-ablated SWNTs were transferred from the SDS suspension onto the GaAs substrate. After locating the nanotube lying across the edge of SiO_2 by AFM, a second e-beam lithography was applied to make the electrical contacts (AuPd). There are two electrodes for each GaAs/SWNT junction. One caps the nanotube (the part on the SiO_2 layer) and the other contacts the GaAs substrate. This assures that current goes through the GaAs/SWNT interface. Similar devices were reproduced on both n- and p-doped GaAs (five devices on n-doped GaAs and three on p-doped GaAs).

5.3 Charge transport of GaAs/CNT heterojunctions

The current-voltage characteristics of the n-doped GaAs/SWNT and p-doped GaAs/SWNT heterojunctions (denoted as n-GaAs/SWNT and p-GaAs/SWNT, respectively) are shown in Figure 5.3.1b. A rectifying behavior is observed in n-GaAs/SWNT: Current is blocked when the SWNT is biased negatively but starts to increase while the polarity is switched to the opposite. Therefore the device is at forward (reverse) bias when the voltage applied to SWNT is positive (negative). There is a voltage threshold of 0.2 V, until which the current does not increase, at the positive bias. This indicates a built-in electrical field at the interface between n-GaAs and SWNT. Contrary to n-GaAs/SWNT, the p-GaAs/SWNT heterojunction shows an ohmic-like behavior instead of rectifying current. This clearly shows a different transport mechanism inside the p-GaAs/SWNT from the n-GaAs/SWNT. Figure 5.3.1c shows that the n-GaAs/SWNT junction is rectifying in the temperature range from room temperature to 4 K with a decrease of forward current from 107 to 1.5 nA at 2 V. Meanwhile, the threshold voltage increases from 0.2 to 1 V. Staircase-like curves are observed in the forward current at temperature equal or lower than 66 K. This results from the effect of Coulomb blockade, a typical signature of single electron tunneling in the

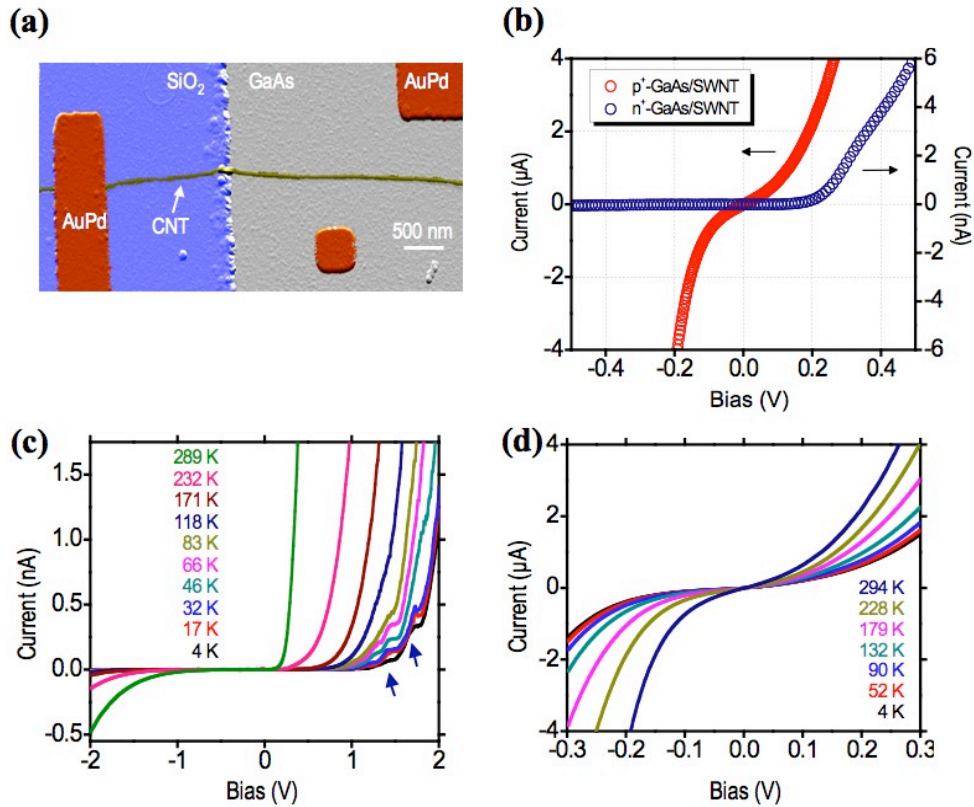


Figure 5.3.1 (a) Colored AFM image of an GaAs/SWNT heterojunction. (b) Comparison of the $I-V_{sd}$ curves of n- and p-GaAs/SWNT devices. To the extended voltage range, the current amount of n-GaAs/SWNT at forward bias (2 V, 107 nA) is 3 orders of magnitude larger than it is at reverse bias (-2 V, -485 pA). For p-GaAs/SWNT, the current at both voltage polarities was observed having comparable values (-20.5 μA at -0.3 V; 5.4 μA at 0.3 V) instead of being strongly blocked. (c) $I-V_{sd}$ curves of n-GaAs/SWNT at different temperatures. Arrows point out the staircaselike structure as a consequence of the Coulomb blockade. (d) Temperature-dependent $I-V_{sd}$ curves of the p-GaAs/SWNT heterojunction.

lowdimensional system.[TDD] On the other hand, the p-GaAs/SWNT holds the ohmic behavior also from room temperature down to 4 K (Figure 5.3.1d). The $I-V_{sd}$ curve is symmetrical to the zero bias up to 132 K. The conductance at 4 K is 4.53 μS ($0.12 e^2/h$) at ± 0.3 V but is 18 μS ($0.46 e^2/h$) for -0.3 V and 68.3 μS ($1.76 e^2/h$) for 0.3 V at room temperature. Due to the high conductance of the p-GaAs/SWNT junction, p-GaAs, like (Ga,Mn)As, has been proposed as a contact material for CNTFETs in addition to metals. [JHN] It should be emphasized that although the same behaviors (rectifying for n-

GaAs/SWNT and ohmic for p-GaAs/SWNT) as well as their temperature dependence have been observed in all of our devices, the measured values are not always identical. This is due to the variation of the diameter, length, contact area with GaAs and the metal-contact resistance of the nanotubes.

The reproduction of the rectifying behaviors from all of the n-GaAs/SWNT heterojunctions indicates the nanotubes belong to the same type and their polarity shows that holes are transported in the nanotubes. Hole transport is a distinct feature of semiconducting nanotubes due to their near ohmic contacts with high work function metals like Au or Pd.[JGW][JWK] If the nanotube is metallic, the device is then modeled as metal/n-GaAs/metal, where the transport should be dominated by electrons instead of holes. As for the p-GaAs/SWNT, although the current is larger when the p-GaAs is biased positively, indicating its hole transport mechanism, this is not sufficient to suggest the type of the nanotube because hole transport may exist in either semiconductor/p-GaAs/metal (with a semiconducting nanotube) or metal/p-GaAs/metal (with a metallic nanotube).

The logarithmic version of the I - V_{sd} curves at various temperatures, as shown in panels a and b of Figure 5.3.2, reveals the transport details. According to the theory of thin-film semiconductor heterojunctions, two possible models account for the transport mechanism: the thermionic and the tunneling ones.[RF][ZA] The mathematical formulations of the former and the latter are

$$\log(I) = \log(I_0) + \frac{qV_{sd}}{kT} \quad (5.1)$$

and

$$\log(I) = \log(I_0) + \alpha V_{sd} \quad (5.2)$$

respectively, where k_b is the Boltzmann constant, q is the electron charge, I_0 is the saturation current extrapolated from the logarithmic I - V_{sd} curve, and α is a constant related to the tunneling barrier of the junction. The determinant difference between the two mechanisms is the temperature dependence of the slope of the $\log(I)$ - V_{sd} curve. The slope is temperature dependent in the thermionic model but is insensitive to temperature in the tunneling model. It is noticed that the slope of the curves in both panels a and b of Figure 5.3.2 are not sensitive to temperature. This ascribes the transport of the GaAs/SWNT

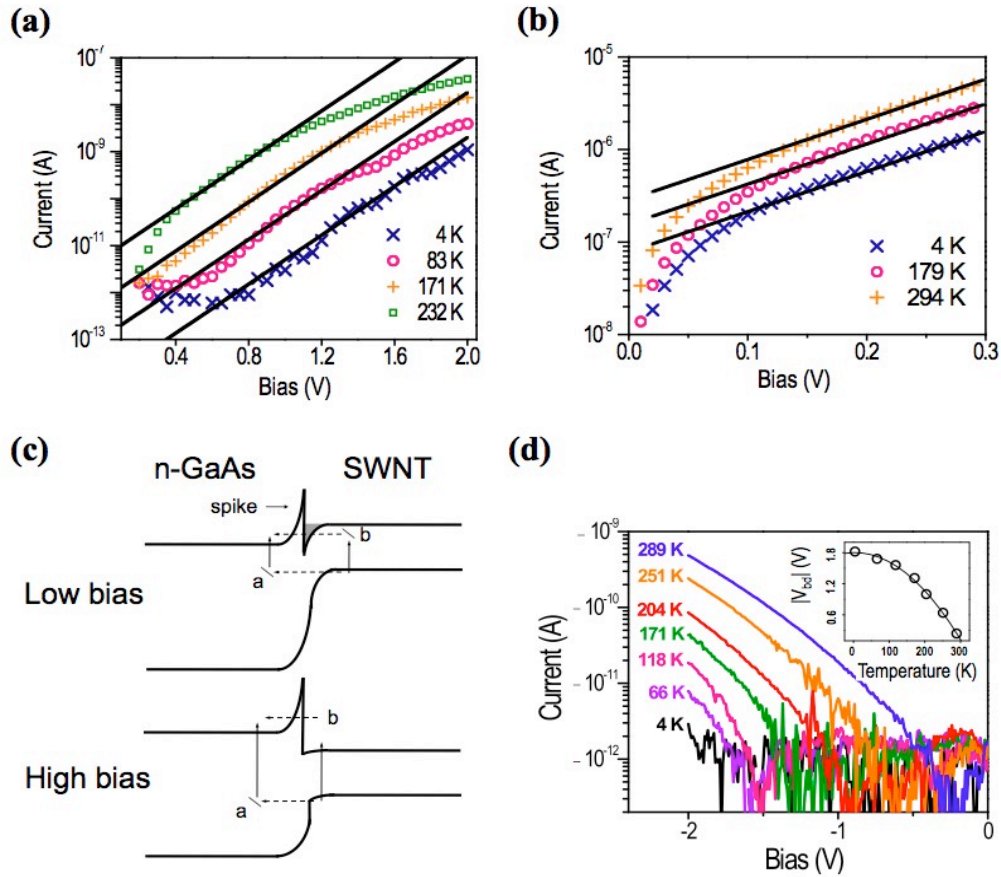


Figure 5.3.2 Logarithmic I - V_{sd} curves of the GaAs/SWNT heterojunctions and the tunneling processes: (a) n-GaAs/SWNT junction; (b) p-GaAs/SWNT. Each panel shows the $\log(I)$ - V_{sd} curves of the GaAs/SWNT heterojunctions at temperatures from 4 K to room temperature in the forward-bias regime. The black lines are the calculated curves using the tunneling transport model. (c) Tunneling processes of the high- and low-bias transport through the n-GaAs/SWNT junction. (d) The $\log(I)$ - V_{sd} curves of the n-GaAs/SWNT junctions in the reverse-bias regime. Inset: absolute values of the breakdown voltage V_{bd} as a function of temperature.

heterojunctions to the tunneling model. Calculations using eq. 5.2 fit the experimental data well when taking $\alpha = 3.3$ for n-GaAs/SWNT and 13.3 for p-GaAs/SWNT. However, the data points of the n-GaAs/SWNT junction deviate from the theoretical curves at larger bias (>1 V) and higher temperatures (171 K and 232 K). To explain the deviation, a tunneling model introduced by Zeidenbergs et al. is adopted.[ZA] This approach is based on the Anderson model[And] of thin-film semiconductor heterojunction, which introduces a spike in the band structure at the interface of the heterojunction. Zeidenbergs et al. argued that

when tunneling is the dominating transport mechanism, the tunneling barriers of a degenerate semiconductor heterojunction at high and low bias are different. As illustrated in the Figure 5.3.2c, holes in the SWNTs can tunnel across the n-GaAs/SWNT through two routes: (process a) tunneling from the SWNT valence band edge to the interband states in the n-GaAs and then recombining with electrons in the conduction band of n-GaAs, or (process b) jumping from the valence band to the interband states of SWNT and then tunneling through both the inversion layer (gray area) and the spike to the GaAs conduction band. The difference between the low/high-bias transport is the existence of the inversion layer. The inversion layer is negligible at high bias but is not at low bias. This results in a different tunneling barrier seen by electrons, causing a different slope of the $\log(I)-V_{sd}$ curve (denoted as α previously) for low and high bias regions. Since the calculations in Figure 5.3.2a use the same α value throughout the whole bias range, deviation occurs.

The tunneling transport of the n-GaAs/SWNT junction is further characterized by the transport results at reverse bias region. When the reverse bias is sufficiently high (larger than the so-called breakdown voltage, V_{bd}), a sharp increase of the reverse current is observed. This is often called “junction breakdown”. Figure 5.3.2d shows the breakdown regime of the n-GaAs/sWNT at different temperature. Two main mechanisms account for the breakdown phenomena: the Zener breakdown and the avalanche breakdown. The Zener breakdown comes from the direct tunneling through depletion region at the junction. The amount of the reverse current rises because of the thinning of the depletion region at higher bias. However, the avalanche breakdown resulted from impact ionization: when the electrons are energized by the bias voltage and injected into the depletion layer, they will collide with atoms and induce ionization thereof. A distinction between the two mechanisms is their temperature dependence.[Sze] The breakdown voltage is larger at higher temperature for the avalanche breakdown because at high temperature the energy of the electrons is relaxed by the phonons in the depletion region. Opposite to the avalanche breakdown, the breakdown voltage decreases at higher temperature in the case of Zener breakdown. This is because the semiconductor bandgap decreases at high temperature, [Var] resulting in a reduction of the tunneling barrier at the depletion region.[Sze] The

breakdown behavior of the n-GaAs/SWNT (Figure 5.3.2d) shows a V_{bd} decrease with increasing temperature and is then ascribed to the Zener breakdown. The temperature dependence of the V_{bd} (in absolute value) is plotted in the inset of Figure 5.3.2d. The decrease of the absolute value of V_{bd} is linear at higher temperatures (>100 K) but nonlinear at lower temperatures. This may be explained by the decrease of the bandgap that is nonlinear at low temperature and linear at sufficiently high temperature for both GaAs and SWNT.[CST][SPK]

In addition to the above analysis based on the band structure of the semiconductor heterojunction, some other factors may contribute to the tunneling behavior of the GaAs/SWNT junction. From the theoretical point of view, the adoption of the semiclassical model should be considered as a qualitative approach rather than a complete interpretation because the GaAs/SWNT junction is not an infinitive two-dimensional interface due to the small diameter of the nanotubes. Therefore it would be necessary to incorporate the low-dimensional theory for a more detailed analysis. In the case of CNTFETs, light electron effective mass in nanotubes is proposed to be the main reason of tunneling transport. [ARK] Further, the native oxide layer of GaAs (Ga_2O_3 , 1-2 nm) may also contribute to the tunneling barrier in this experiment.

The n-GaAs/SWNT junction was further characterized electrically with illumination, and a photovoltaic effect was observed. The device responds to the green laser light with a short-circuit current, I_{sc} . Switching on/off the laser causes the generation/annihilation of I_{sc} alternatively (Figure 5.3.3a). In addition to the I_{sc} , the open-circuit voltage V_{oc} was also measured. Figure 5.3.3b shows that V_{oc} increases (vanishes) while moving the laser spot close to (away from) the position of the tested nanotube on the substrate. This confirms that the photovoltaic effect is not induced spuriously from other places remote to the device. The I - V_{sd} curves with and without illumination are compared in Figure 5.3.3c, from which a filling factor f of 0.33 is obtained. The short-circuit current density, J_{sc} , of 2 A/cm^2 is obtained by dividing I_{sc} by a junction area, which is estimated conservatively via a methodology of using the projected area by multiplying the length of the SWNT with its diameter. The photovoltaic efficiency of the n-GaAs/SWNT junction is then calculated and found to be 3.8% by the conversion equation:

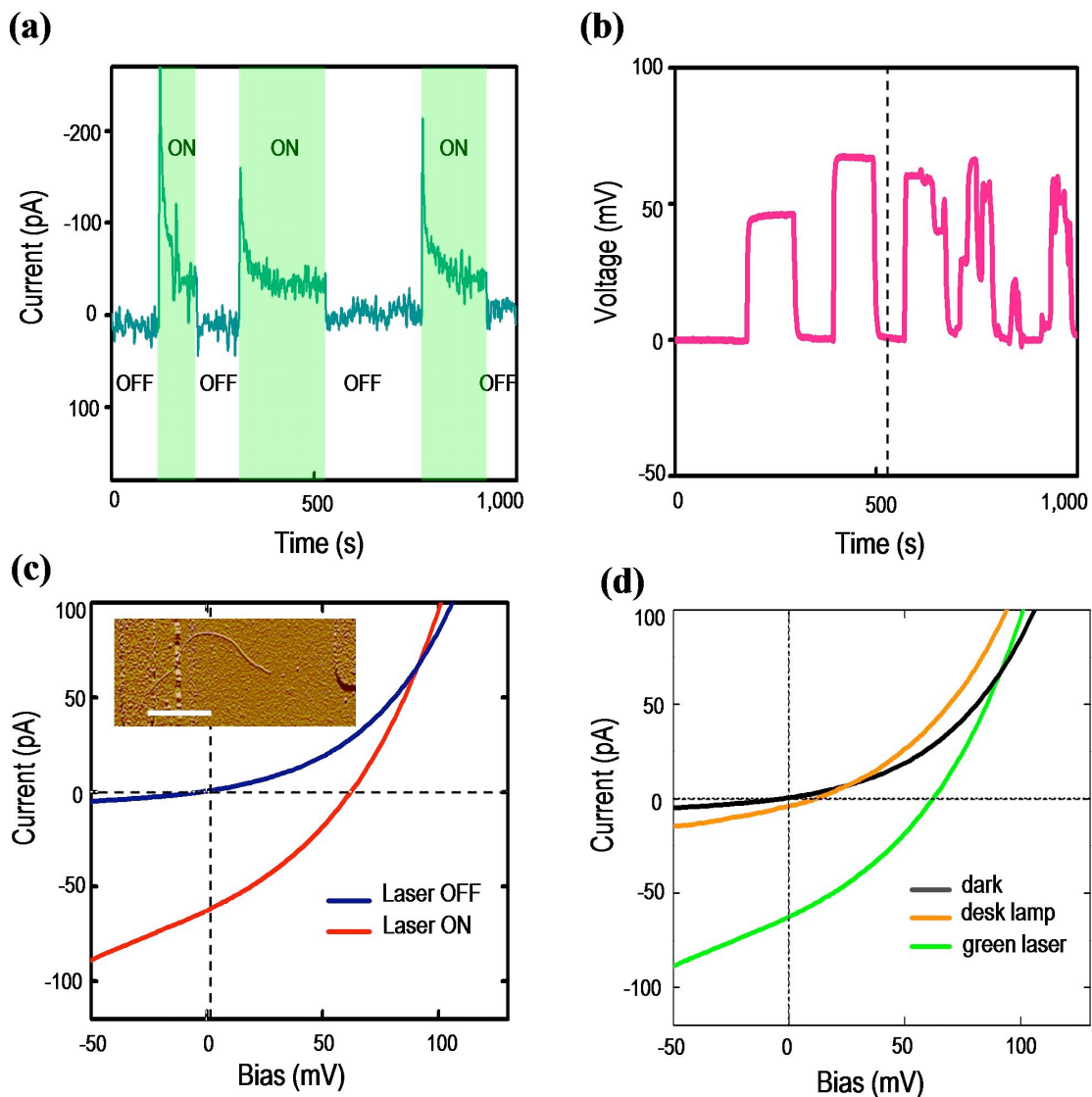


Figure 5.3.3 (a) Real-time record of the I_{sc} of a n-GaAs/SWNT device illuminated by a green laser spot (wavelength, 532 nm; power, 10 mW; diameter, 1 mm). (b) Real-time record of the V_{oc} with the shift of the position of the laser spot. In the first half of the measuring period (prior to the time marked by the dashed line) the spot was moved completely inside/outside the area with metal markers (active area, where the devices are made). No V_{oc} was observed while the laser spot was positioned outside the active area. Later than the marked time, the spot was shaken at the vicinity of the active area. An irregular response of the V_{oc} was then observed. (c) I - V_{sd} curves with and without laser illumination. In this measurement, I_{sc} and V_{oc} are 62 pA and 72 mV, respectively. Inset is the AFM image of the tested device. The scale bar represents 1 μ m. (d) Photovoltaic effects from different light sources. I - V_{sd} curves of a n-GaAs/SWNT junction illuminated by green laser and a desk lamp are compared. Data of dark transport are also included.

$$\eta = \frac{f \times J_{sc} \times V_{oc}}{P_{input}} \quad (5.3)$$

where η is the efficiency, f is the filling factor, and P_{input} is the input power density obtained by dividing the total laser power with its spot area. Beside the green laser, photovoltaic effects have also been observed when illuminating the same device with a regular desk lamp (Figure 5.3.3d). According to the results of the optical transport, n-GaAs/SWNT heterojunctions have potential for energy-transformation technologies such as solar cells. There are several foreseeable advantages when using SWNTs as an active component in a solar cell. For example, its different bandgap increases the absorption spectrum bandwidth by forming different barrier heights at the semiconductor/nanotube interface; its flexibility facilitates the integration of the cell into other systems. However, these benefits would not be available until some technical challenges are overcome, e.g., separation of semiconducting/metallic nanotubes, or a practical design of the device structure, e.g. a well defined semiconductor/nanotube contact.

5.4 Conclusions

In conclusion, both n- and p-GaAs/SWNT heterojunctions have been prepared and their transport properties have been investigated. The n-GaAs/SWNT junction showed a strong rectifying behavior, while ohmic-like contact formed in the p-GaAs/SWNT junction. Photovoltaic effects were observed in the n-GaAs/SWNT junction when the device is illuminated. This experiment lays the groundwork for further studies on semiconductor/nanotube hybrid devices, which may open the access to new technologies: the p-GaAs could be used as a ohmic-contact material for SWNT electronics; n-GaAs/SWNT junctions can be applied as either diode components for high-frequency communication or photovoltaic devices for renewable energy technologies.

Chapter 6

Charge-Molecule Interaction in Carbon Nanotubes

6.1 Introduction

According to the discussion in chapter 3, three out of the four valence electrons for each carbon atom form sp^2 hybridized bonds with the adjacent atoms and the last one forms π bond with wave function spreading over the carbon atoms and contributing to the electrical conduction. Consequently, an ideal carbon nanotube has no dangling bonds, by which the carbon atoms are able to connect with other atoms or molecules covalently. Given its chemical inertness, nanotubes should show stable electrical properties under different ambient conditions. However, many studies have shown violations of this hypothesis in both semiconducting and metallic nanotubes. This is because in the realistic situation, the characteristics of a nanotube are influenced by (1) structural defects and (2) adsorbed substances. Defects create dangling bonds and enable the chemical reaction with other species. As for the adsorbates, which form weaker links to the nanotube, they may scatter the electrons and reduce the mean free path. Although the influences from the foreign objects will mask the intrinsic properties of nanotubes, the high sensitivity of electrical properties of CNT to ambient conditions makes it a good candidate for sensing technologies. However, to get more insight into the interaction between the nanotube and the foreign objects, it is necessary to study the transport phenomena of *the same* nanotube with and without molecules attaching to it. In this chapter, a technique called current-induced annealing (CIA) is demonstrated to be able to fulfil the above requirement by desorbing the gas molecules from the CNTs and revealing their intrinsic properties. With the assistance of this technique, the influences of the foreign objects on the transport properties of the nanotube is further studied. Both

charge and spin transport are studied in this experiment.

6.2 Materials and methods

The CNTFET devices were used in this experiment. Once the samples have been processed, they are loaded into a sealed stainless-steel tube for further measurements. The atmosphere inside the tube can be controlled, enabling the study of the environmental impact to the electrical properties of the device. Figure 6.2.1 shows the AFM image of the device as well as the measurement set-up. Transport measurements were carried out at both room temperature and liquid helium temperature (4.2 K).

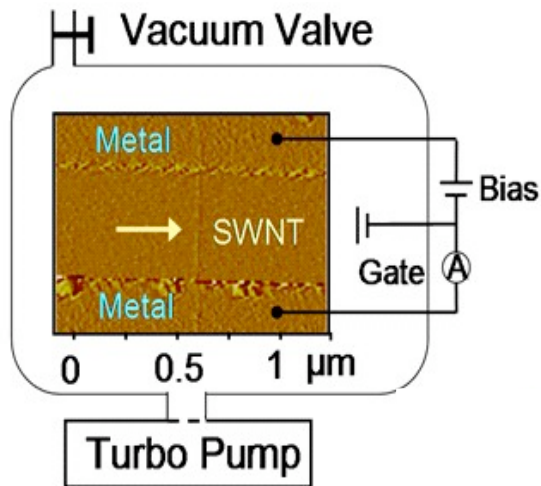


Figure 6.2.1 AFM image of a SWNT device and the measurement setup.

6.3 Current-induced annealing (CIA)

6.3.1 Gas desorption induced by CIA

The CIA process starts with slowly increasing the bias voltage in a vacuum ($\sim 3 \times 10^{-5}$ mbar) to the annealing voltage and then maintaining the target voltage for 1 min. The bias voltage is subsequently lowered to zero and the CIA process is complete. The $I-V_{sd}$ curves of a sequence of CIA cycles are shown in Figure 6.3.1a. The annealing voltage is increased for each CIA cycle. Figure 6.3.1b shows that for each cycle, the device resistance decreases as voltage increases and then saturates at a minimum value, ~ 1.2 M Ω . We also observed in other devices that the resistance

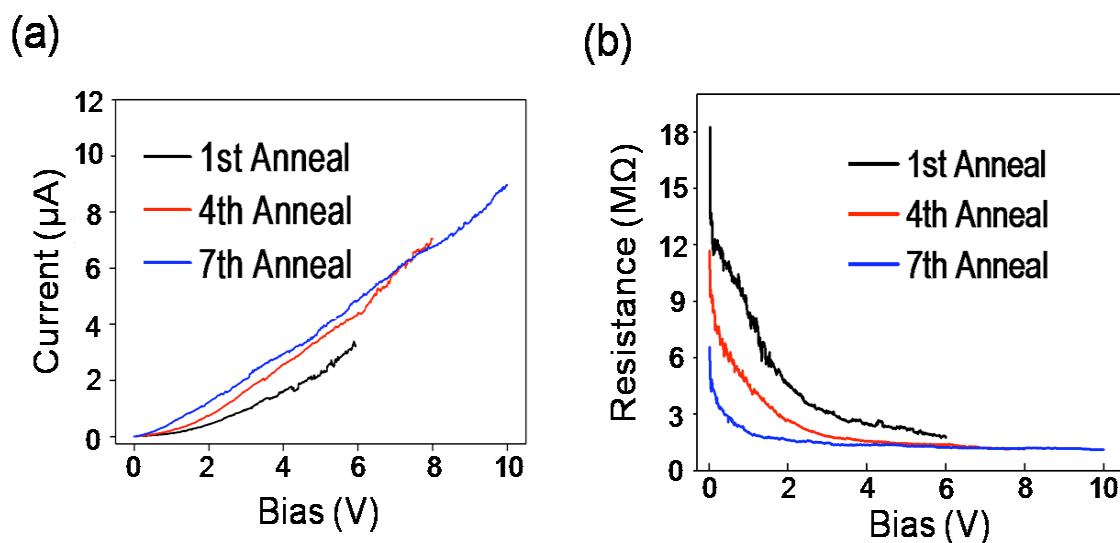


Figure 6.3.1 (a) $I-V_{\text{sd}}$ curves of a sequence of CIA processes. (b) Calculated resistance versus bias.

even increases after reaching its minimum in the high electric field transport regime. This non-linear $I-V_{\text{sd}}$ characteristic in SWNTs at high bias voltage is attributed to high-energy phonon scattering.[YKD][PRY][PMC]

In the low bias region show in Figure 6.3.1b, the resistance decreases from 18 $\text{M}\Omega$ to 5 $\text{M}\Omega$ after several cycles of CIA. This phenomenon is independent of the materials used for electrical contacts. CIA was applied to five devices with AuPd contacts and the influence of CIA on their electrical performance is similar and shows the same trend. In order to confirm the role of adsorbates in the reduction of the resistance we studied the transport behaviour under different ambient conditions. Figure 6.3.2a illustrates the results of a time-resolved measurement. After the CIA process in vacuum the resistance is 9 $\text{M}\Omega$ at low bias voltage ($V_{\text{sd}} = 20 \text{ mV}$). When the chamber is flooded with air, the resistance immediately increases to 13 $\text{M}\Omega$ and saturates later to 18 $\text{M}\Omega$. This result is reproducible by repeating the procedure of evacuating, annealing and exposing the sample to air again.

The $I-V_{\text{sd}}$ characteristics at low bias before and after CIA are compared in Figure 6.3.2b. The current measured in air prior to CIA (green) is less than that measured in a vacuum after CIA (blue). However, it drops to the value close to the unannealed

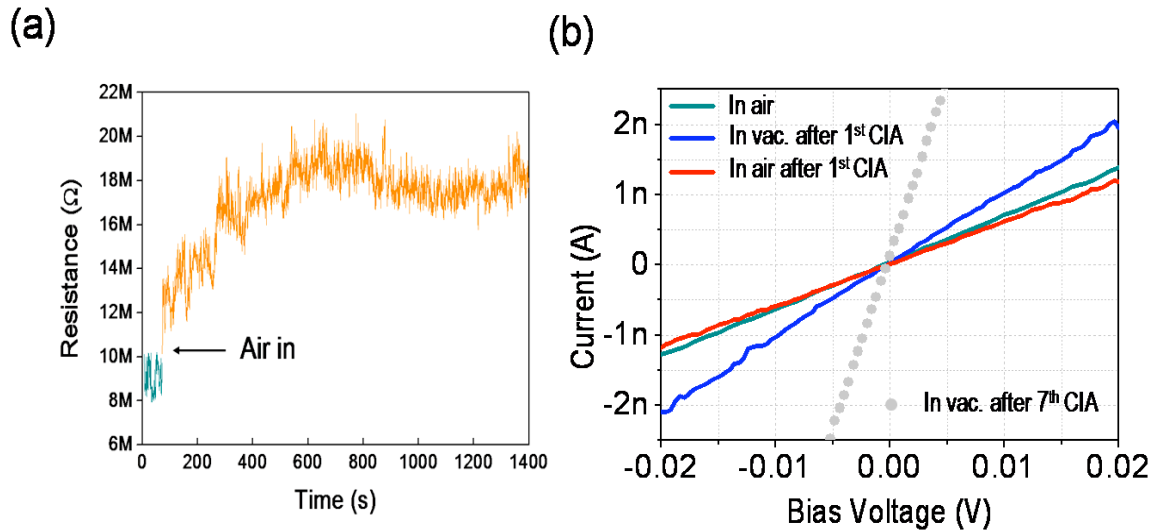


Figure 6.3.2 (a) Time-resolved measurement, which monitored change in resistance while venting the vacuum chamber. (b) $I-V_{sd}$ curves at low bias under different conditions.

one (red) as the device is re-exposed to air. After re-pumping the chamber and applying CIA multiple times without exposure to air, the $I-V_{sd}$ curve shows even less resistance (gray dots). It should be emphasised that annealing is only effective if the bias voltage reaches the high-energy-phonon scattering regime, under which the saturation or increase of resistance is observed. Sweeping bias voltage in low range has no influence on the transport property of CNT devices. The gate-dependent characteristic of the same device, shown in Figure 6.3.3, indicates it consists of a thin SWNT bundle whose transport property is dominated by metallic tubes for the current is slightly modulated by the gate voltage but can not be completely turned off up to ± 10 V.

There are two possible sources to account for the total resistance of our SWNT devices: the metal/SWNT interface and the body of the SWNT. From our previous experiments we can conclude that the decrease in resistance induced by CIA is due to changes in the area of the device exposed to air. Changes at the interface of SWNT and metal can be excluded because in our devices the contact area has the SWNTs beneath the metal electrode. It has been shown that gas desorption can lower the resistance of CNT devices. [SAF] Therefore our data suggests that CIA results in gas desorption from the surface of SWNTs. The process is more efficient (measured by the amount of resistance

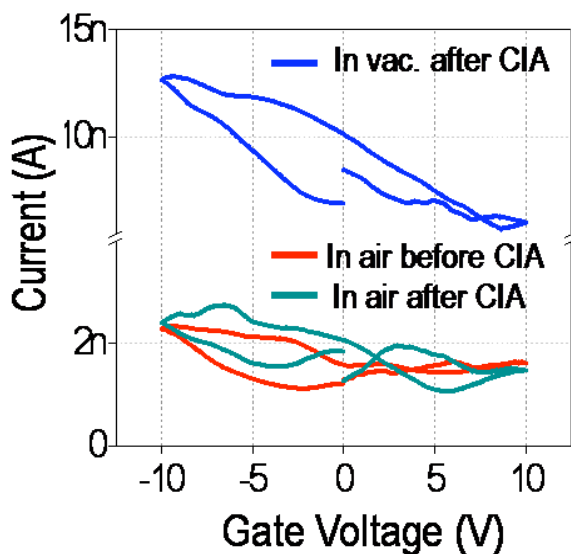


Figure 6.3.3 Current versus gate voltage before and after performing the CIA process. The bias voltage is 20 mV.

decrease) with higher current (bias), longer annealing times or a greater number of annealing cycles. When the SWNTs devices are exposed to air, the resistance rises immediately and then saturates slowly. This indicates that the main adhesion sites, e.g. grooves in bundles or defects in SWNTs, are covered by gas molecules instantly after venting. Afterwards, molecules are adsorbed onto other places of the SWNT at a slower rate. The existence of hysteresis reveals the details of the influence of CIA. One of the main causes of hysteresis is due to the charge trapping by the water molecules, including those directly adsorbed on the nanotubes as well as SiO_2 surface-bound water proximal to the nanotubes, and it has been shown that the former can be removed via pumping in vacuum but additional processes like heating or chemically modifying the surface are needed to remove the latter.[KJV] The remained hysteresis after performing CIA in vacuum indicates that CIA only affects the molecules which adsorb directly on nanotubes but is not efficient enough to heat the SiO_2 to desorb the water on the substrates. Therefore only slight change in hysteresis can be observed.

The influence of the gas desorption on the electrical properties of the metallic SWNTs is different from the semiconducting ones. Previous study has shown that, with a similar method, the atmospheric gas molecules were also removed from the semiconducting SWNTs.[CF] However, differing from our results, the annealing on semiconducting nanotubes decreases the conductance and the exposing of the devices to the air makes the

conductance increase again. Such a phenomenon is attributed to the doping effect caused mainly by the O₂ in the air, which increases free carriers in nanotubes and varies the depletion width at the interface between the nanotubes and metal contacts. Since the carrier density can be scarcely changed in metallic tubes, therefore the opposite response of the metallic nanotubes to the gas molecules results from a different mechanism: gas molecules behave more like scattering centers rather than dopants.

6.3.2 Annealing mechanism

The observation that CIA is effective only when the bias is high enough to generate high-energy phonons suggests that phonons play an important role in the CIA process. At low bias voltage, the electrons are scattered by acoustic phonons, which have lower energy ($\hbar\omega_{ac} \ll kT$, ω_{ac} is the acoustic phonon frequency) and larger scattering length (on the scale of μm). Such weak electron-acoustic-phonon scattering has been demonstrated experimentally.[PRY] The energy transfer between electrons and acoustic phonons is small, explaining the weak annealing effect at low bias voltage. Phonons generated at high field, however, have higher energy ($\hbar\omega_{hp} \gg kT$) and shorter scattering length (tens of nm). Consequently we conclude that CIA is caused by high-energy phonons instead of acoustic phonons (more detailed discussions about the electron-phonon interaction can be found in the appendix B). The energy of the high-energy phonons, according to ref [PRY], is in the range of 0.1 to 0.2 eV. This value is in the same order as the adsorption energy of some regular gas molecules in air, e.g. O₂, H₂O and CO₂, on SWNTs.[ZBH] Several preliminary trials, in which the devices were exposed to He and N₂, have been carried out to study the influence of certain gas species but no clear change of the resistance was observed. As pointed out by Ref. [CF], dry gas sources (He, O₂ and N₂) does not affect the nanotube devices but moist O₂ has the most influence, therefore the moisture might be the dominant factor in our experiment.

Figure 6.3.4 compares the I - V_{sd} curves at room temperature and 4.2 K on the same device. The scattering length of emitted phonons can be obtained by

$$R_{high} = R_{low} + \frac{h}{4e^2} \left(\frac{L}{l_{eff}} \right), \quad (6.1)$$

where $R_{high(low)}$ is the high (low) -field resistance, L is the length of SWNTs and l_{eff} is

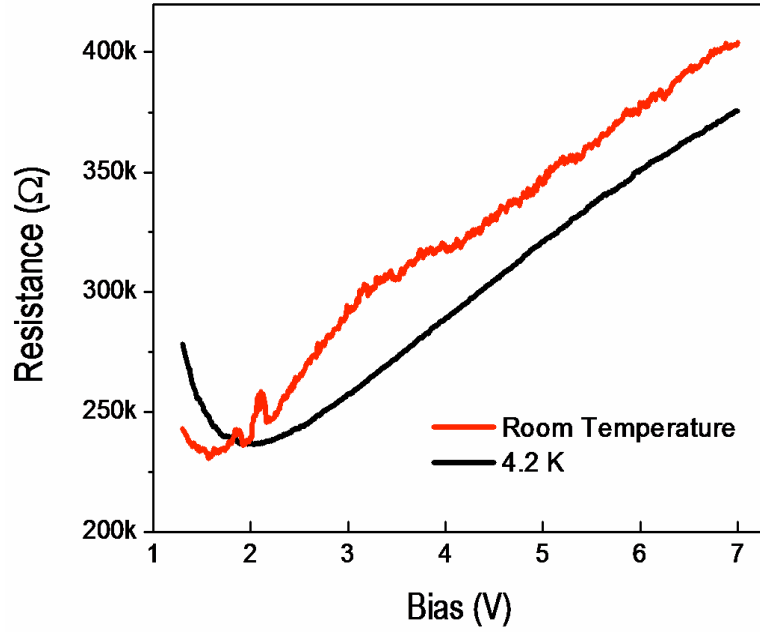


Figure 6.3.4 Comparison of resistance versus V_{sd} at room temperature and 4.2 K.

the effective scattering length, which is dominated by high-energy phonons at high bias voltage.[PRY] To calculate the effective scattering length at 4.2 K, we take $R_{high} = 374 \text{ k}\Omega$ (resistance at 7 V), $R_{low} = 236 \text{ k}\Omega$ (resistance at 2 V) and $L = 500 \text{ nm}$, and an effective scattering length of 23 nm is obtained. The effective scattering length at room temperature is also calculated with the same procedure and is found to be 19 nm. Between two subsequent scattering events, electrons accelerated by the electric field gain kinetic energy. This kinetic energy is then transferred to phonons while scattering occurs. Therefore the phonon energy can be calculated by

$$E_{ph} = \frac{l_{eff}}{L} V_{sd}, \quad (6.2)$$

where E_{ph} is the phonon energy. When applying 7 V as the bias voltage at 4.2 K, Phonon energy obtained from eq. 6.2 is 0.32 eV. As for the room temperature measurement, it is found to be 0.27 eV. Since both the scattering length and the phonon energy have similar values at room temperature and at 4.2 K, phonons generated at room temperature and at 4.2 K are of the same type. This is consistent with our observation that CIA is independent of temperature.

Two mechanisms are suggested to explain the effect of CIA. The first is Joule heating to thermal equilibrium and raise the temperature of SWNTs. This is the same mechanism for thermal annealing. Since SWNTs in this experiment lie on a Si substrate, which behaves as a thermal reservoir, and CIA is still effective when the device is immersed into a liquid helium bath, the independence of CIA from temperature indicates the insignificance of heat dissipation if Joule heating is responsible for CIA. Another possible mechanism is based on the concept of nonequilibrium optical phonons.[LPM] Nonequilibrium optical phonons have higher energy but do not equilibrate with other phonons with lower energy. Taking this model further, CIA would then cause random collisions between adsorbates and nonequilibrium optical phonons. As long as the energy of phonons is higher than the adsorption energy higher than the adsorption energy, adsorbates are dislodged and desorption occurs. From this consideration the independence of CIA on temperature can be directly inferred. However, further investigation is needed in order to determine the dominating mechanism of CIA.

6.4 Influences of molecules on CNTs

6.4.1 Molecules as momentum-scattering centers

Low-temperature transport measurements have been carried out to study the detailed influences of the gas molecules on the nanotubes. Surprisingly, the effect of CIA at 4 K is comparable or even stronger than it is at room temperature. Figure 6.4.1 shows the representative results obtained from two metallic nanotubes, device 1 (D1) and device 2 (D2), undergoing a sequence of CIA processes. The conductance of both devices becomes larger, but ceases increasing after certain times of CIA, as shown in Figure 6.4.1a, 6.4.1c and their insets. The same behavior was also observed in other tested devices. This is because the final resistance is limited by the contact, on which CIA has less influences, and the amount of reduction of the resistance caused by CIA depends on the degree of the influence of gas molecules. Therefore the larger increase of conductance in D2 caused by CIA (D1: 0.03 to $0.33 e^2/h$; D2: 4×10^{-4} to $0.17 e^2/h$) may be due to its longer nanotube (D1: 300 nm; D2: 600 nm), which likely adsorbs more molecules. Comparing the gate response of the conductance of the two devices (Figure 6.4.1b and d), it was found that the four

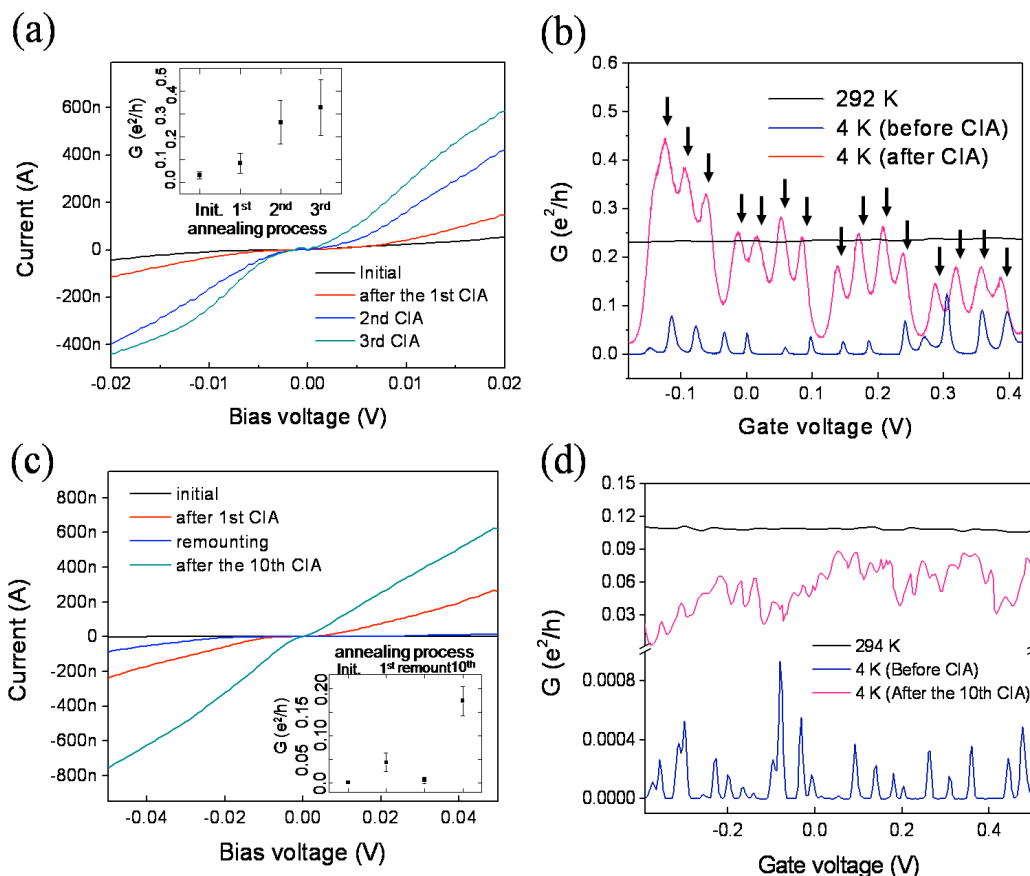


Figure 6.4.1 Effects of CIA on low-temperature transport of SWNTs; two devices are tested and compared. (a) $I-V_{sd}$ curves of device 1 (D1). (b) Gate responses of D1. Arrows show the four-electron periodicity (one missing in the leftmost hump). (c) $I-V_{sd}$ curves of device 2 (D2). (d) Gate responses of D2. Insets of (a) and (c): the conductance of D1 and D2 after various CIA steps. The increase of the conductance after CIA was observed in both devices, thus showing the trend as the measurement is performed at room temperature. In the sequential CIA processes of D2, the sample was warmed and removed from the cryostat. A recovery of the conductance back to the lower value was observed after remounting the sample into the cryostat.

peaks on each hump in D1 do not appear in D2. The four-peak structure in D1 is due to the shell-filling of the CNTQD with two spin-degenerate sub-bands.[LBP][CWD] This properties was shielded by the molecules before CIA but shows afterwards. This indicates that the revelation of the intrinsic electronic structure of the SWNTs is a consequence of the cleaning of the nanotube surface — an oversimplified interpretation. Missing of the four-electron periodicity in D2 implies the complexity of the real situation

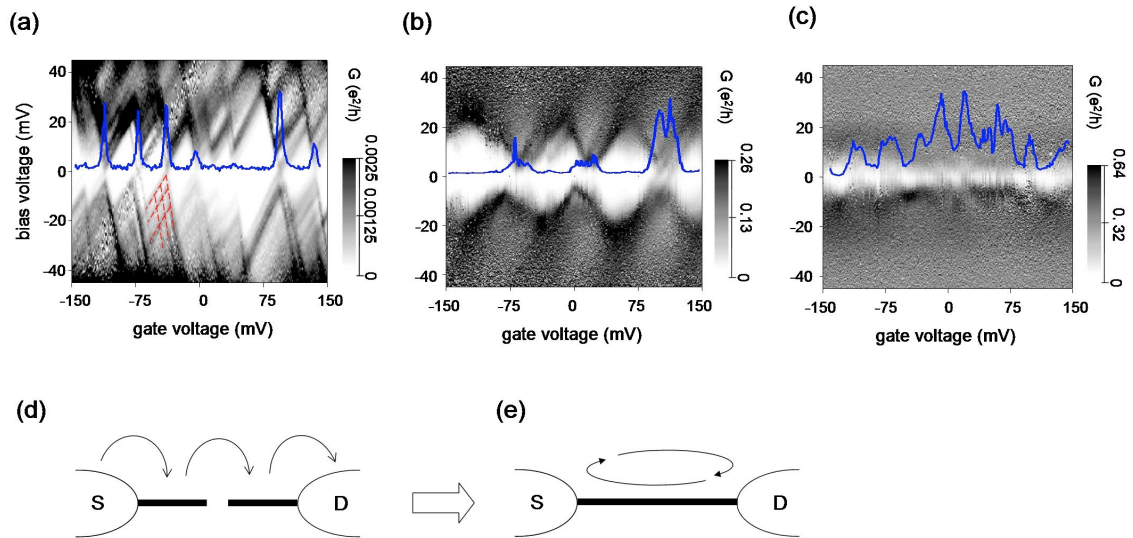


Figure 6.4.2 Evolution of the stability diagrams of D2 at different stages of CIA. (a) Before CIA. The red dashed lines mark the excited states of the SWNT QD. (b) After the third CIA cycle. (c) After the tenth CIA cycle. The blue curves embedded in the three stability diagrams show the differential conductance near the zero-bias regime ($V_{sd} = 0.1$ mV). (d) Series-coupled double QDs forming in a sectioned SWNT. The electrons enter the first dot in the nanotube from the source electrode (S), tunnel through the barrier created by the gas molecules into the second dot, and then enter the drain electrode (D). (e) Interference of the electron waves, which are reflected back and forth by the source and drain contacts, inside the nanotube.

during the annealing

Studies on the stability diagrams of the CNTQD help understand more details of the interaction between the gas molecules and nanotubes. As shown in Figure 6.4.2a, b and c, dramatic variation of the stability diagrams of D2 displays the different electronic structures of the CNTQD. The width of the Coulomb peaks near the zero bias increases along with the repetition of CIA and the charging energy after each annealing process also changes. Nine diamond-like patterns are seen before CIA (Figure 6.4.2a) but there are only three after the 3rd CIA (Figure 6.4.2b). Patterns of excited states are clear in Figure 6.4.2a but smeared out after annealing at the same V_{sd} range (± 40 meV). After the 10th CIA features become more blurred and the diamond structure is hardly visible (Figure 6.4.2c). This indicates the onset of Fabry–Pérot interference inside the nanotubes. The stability diagram stops evolving after the 10th CIA and further annealing does not cause obvious

changes of the property. A similar trend of the evolution was also seen in D1.

The transport measurement of a nanotube at zero-bias regime reveals its energy structure at ground state. This implies that the single QD model is not applicable to explain the evolutionary behaviors observed in D1 and D2 because a single QD should have fixed ground-state energies. Therefore a series-coupled multi-QD model[MBM] is suggested: The gas molecules attaching on the defective sites of the nanotube scatter the electrons and create local energy barriers, which section the nanotube into a serial multi-dot system. Transport through the system can occur only if the energy levels of each dot are aligned, allowing the electrons to tunnel from one dot to another (Figure 6.4.2d). Once the molecules are removed the energy barrier is reduced or diminished. This increases the coupling between the series-coupled QDs or even merges them into a single dot (if the defect has only minor influence on the charge transport). In the extreme case of very clean tube, the electron is transported ballistically. Lacking of the relaxation of momentum inside the nanotube, the electron waves can only interfere with those reflected back from the contacts (Figure 6.4.2e). Such an interference is the origin of the Fabry–Pérot oscillations shown in the transport data of CNTs.[CWD][LBB] This is consistent with what we have observed in both D1 and D2. However, since the nanotube of D2 is twice as long as the nanotube of D1, the structural defects in D2 might have stronger influences that make the intrinsic properties of SWNTs not fully recoverable. This may be the reason why the four-electron periodicity observed in D1 is not shown in D2.

6.4.2 Molecules as spin-relaxation centers

The development of the CNT-based spintronics is concerned by the spin relaxation centers existing inside the nanotubes, causing the low-yield of CNT-based spin valves. Hinted by the results obtained from the CIA experiment, one can apply the technique to study the influences of gas molecules on the spin coherency of the nanotubes and to possibly identify the origin of the spin-relaxation mechanism inside the nanotubes. For this purpose nine devices with cobalt contacts have been made and tested. The length of the nanotubes is in the range of 400 – 500 nm (Figure 6.4.3a). At room temperature, p-type behavior was observed in these cobalt-contacted devices (Figure 6.4.3b). The spin-transport measurement was carried out at 4.2 K with the application of magnetic field from the

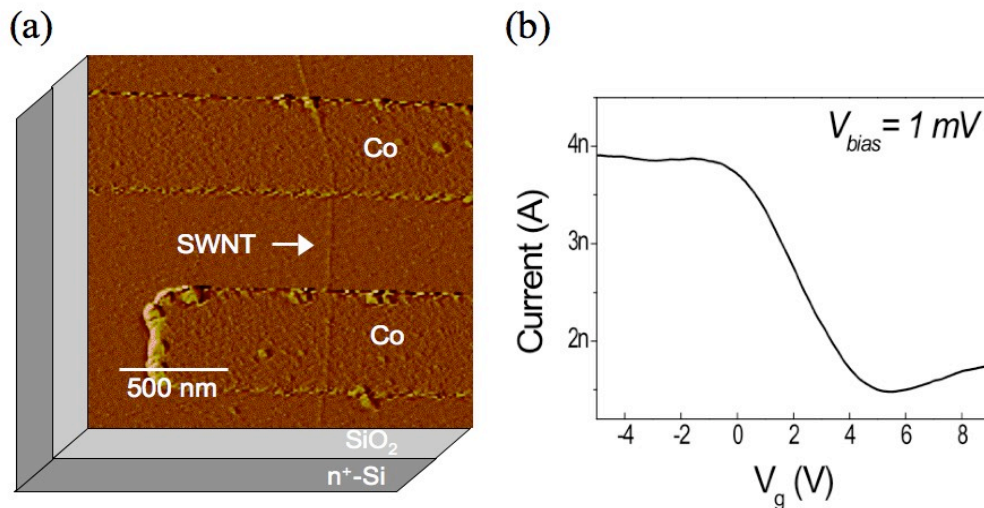


Figure 6.4.3 (a) AFM image of a CNT spin-valve with Co contacts. The magnetic field is applied in the direction parallel to the substrate surface but perpendicular to the tube axis. (b) Current vs. gate voltage (V_g) characteristic of the CNT spin-valve at room temperature. Current is larger at negative gate voltage. The source-drain bias (V_{sd}) is 1 mV.

superconducting magnet in the cryostat. Although the spin diffusive length of an ideal carbon nanotube was estimated to be $50 \mu\text{m}$, [HPF] which is much larger than the tested devices, non of the nine devices showed the spin-valve effect, meaning no hysteretic switching in the MR when sweeping the magnetic field back and forth was observed. The left panels of Figure 6.4.4 is shown as the examples. However, after performing CIA on these devices, abrupt switches of MR appeared on five devices (the right panels of Figure 6.4.4), indicating the spin-valve effect is resolved therefrom. The efficiency of the spin-valve effect can be characterized by the equation: $(R_{AP} - R_P)/R_P$, where R_{AP} (R_P) is the device resistance at anti-parallel (parallel) magnetization. The efficiency is found to be different from device to device in its absolute value as well as its sign. The disappearance and appearance of the spin-valve effect on the same nanotube demonstrate that the spin-relaxation centers are removed by annealing the sample electrically. As pointed out by the discussion in 6.3.1 as well as the Ref. [SNN][CF], these are either structural defects or gas molecules adsorbing on the SWNTs. Therefore the spin relaxation in the CNTs can be attributed to the defects and attached gas molecules.

Figure 6.4.5a depicts the mechanism of spin-relaxation in nanotubes caused by the imperfections (defects or adsorbates). As spin-polarized current is injected into the

nanotubes, the electrons tend to occupy the energy states separately instead of sharing the same one due to the Pauli exclusion principle. However the allowed empty states for the conducting electrons is limited due to the quantization of the 2D Brillouin zone of graphite into 1D discrete lines in the nanotubes. Therefore once the momentum of a conducting electron is changed by the scattering, the electron would have to adjust its spin in order to enter another state that is most likely to be pre-occupied by another electron with the same spin. Consequently the scattering does not only relax the electron momentum but also spin.

If the diameter of a nanotube is infinitely large, its Brillouin zone is a smooth surface in k -space rather than discrete lines. In this case, it has much more empty states comparing with a nanotube with a finite diameter. This largely increases the possibility for the spin-polarized electrons to find available states, which are not pre-occupied by other electrons with the same spin, and hence conserve their spin state while being scattered. The influence of the imperfections is consequently weaker. A graphene sheet meets this hypothetical condition. Several experiments have shown that graphene is able to transport spin coherently over larger distance and at higher temperature than CNTs do (CNT: 1 μm and 120 K, graphene: 2 μm and room temperature)[HPF][TJP], even though its large surface area should, in principle, cause graphene to have more imperfections than SWNTs. In addition to the viewpoint from k -space, the spin relaxation can be also explained from the geometric point of view. As shown in Figure 6.4.5b, the probability for the electrons to encounter imperfections and bounce over them is higher in nanotubes than in graphene, simply because a CNT is quasi one-dimensional and graphene is two-dimensional. From point of view, spin transport in graphene is more immune to scattering than it is in the CNTs.

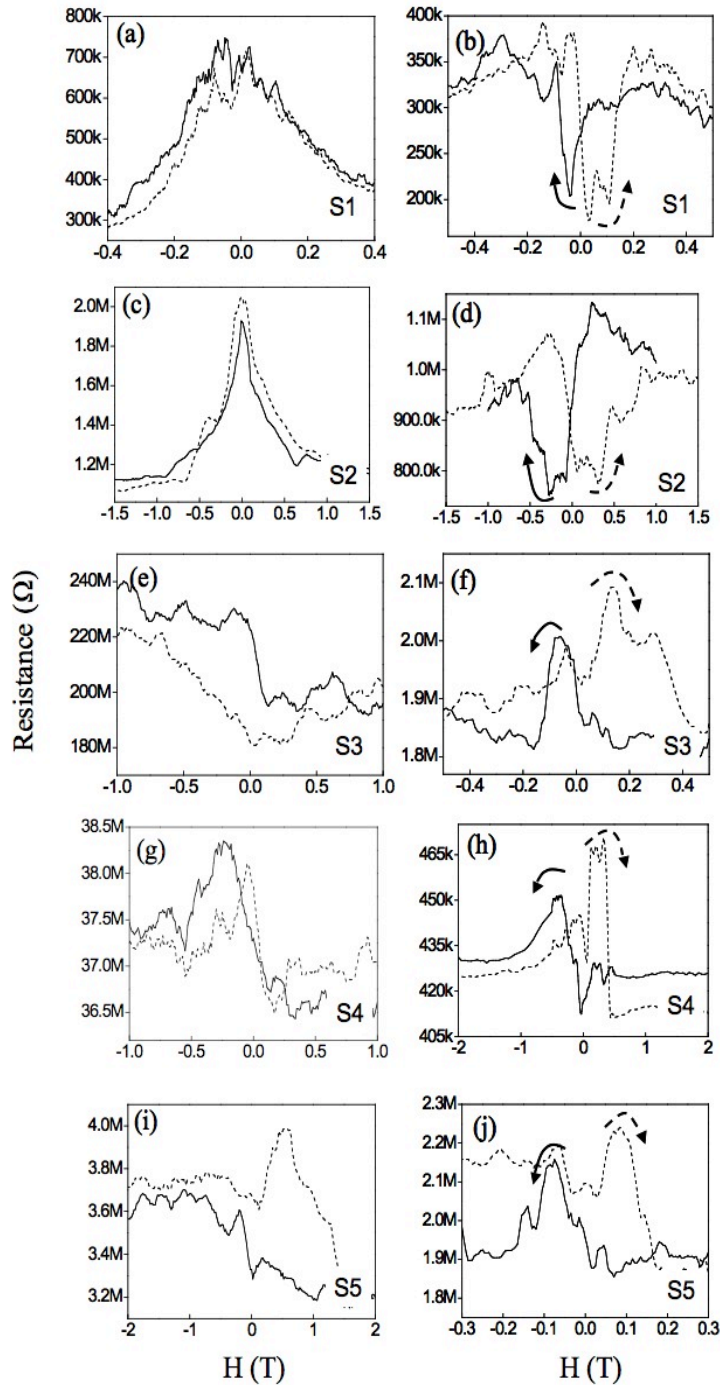


Figure 6.4.4 Magnetoresistance of ferromagnetically contacted nanotubes at 4.2 K. Five samples out of nine showed spin-valve effect after annealing. Samples are numbered from S1 to S5. Graphs in the left column show the magnetoresistance of the five samples before annealing and those in the right column show the responses from the corresponding samples after annealing. The dashed (solid) lines illustrate the positive (negative) sweeping direction of the magnetic field.

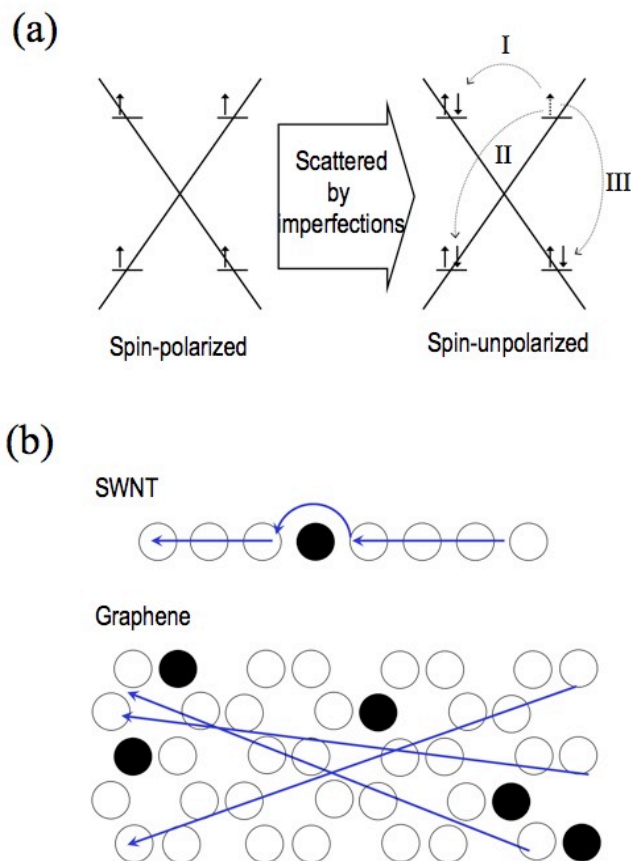


Figure 6.4.5 (a) Schematic showing of the mechanism of spin relaxation inside the carbon nanotubes. Quantized energy states near the Fermi level (cross point) are occupied by the spin-polarized electrons (short arrows) injected from the ferromagnet electrode. After scattered by imperfections (defects or adorbates), electrons flip their spin in order to enter other half-filled states (Path I, II and III). The spin-polarization is then lost after scattering. (b) The scattering processe in real-space. Empty (filled) circles represent the lattice points (imperfections). Arrows show the path of electrons through the materials. It should be noticed that the percentage of the imperfections among the lattice is the same for nanotubes and graphene.

6.5 Conclusions

The effect of CIA on the CNTs by applying large electric field has been studied. The impact of CIA is independent of the contact materials as well as the temperature of the environment. CIA generates high-energy phonons, which induce gas-desorption from the CNTs, resulting in a reduction in device resistance and revealing the intrinsic properties of the nanotubes. The influence of the gas molecules attached to the nanotubes is then confirmed to be a strong scattering effect, which creates the multi-QD structure inside an individual nanotube in some cases. The effect of such scattering on the spin transport is further studied in the CNT spin-valve devices. It is found that after removing after removing the adsorbates, which relax the spin coherency in the nanotube, by CIA, spin-valve effect can be observed from those devices. Therefore the yield of the working devices is increased by this technique. Further analyses show that the spin-relaxation due to the scattering is dimension-dependent for the graphitic materials: graphene is less affected than CNT is.

Chapter 7

Summary

The study of carbon nanotubes is an epitome of the complexity in the nanoscience. Since its discovery in 1991, the measurement of the transport properties of an individual nanotube was not reported until 1997 and then a few years of debates on its intrinsic characteristics followed in the science community. All of this reflects the difficulties in conducting the experiments and the interpretation of the results.

This thesis focuses on the characterization of various nanotube electronics. The transistor behaviors of individual nanotubes with various contact configurations were first studied. CNTs with AuPd electrodes show a p-type transistor behavior while those contacted by aluminum are n-type. Such a difference is explained by the Schottky barrier model, in which the high/low work function of the metal causes the p/n-type behavior. We further studied a CNT devices with asymmetrical contacts and found that these devices show a rectifying characteristic. These devices are conductive when positively biasing the electrode of high working function (AuPd in our experiment). Such a result is also consistent with the Schottky barrier model. These data show that the transport characteristic of nanotubes are very sensitive to the contact materials and what the measurement probes is actually a combined result.

The following topic is GaAs/CNT heterojunctions, where we studied the interface between the nanotubes and a semiconductor instead of a metal. Results show that the transport properties are sensitive to the doping type of GaAs: the n-GaAs/CNT is rectifying while the p-GaAs/CNT is ohmic. The transport mechanism through the interface is found to be dominated by tunneling. Photovoltaic effects are also observed in the n-GaAs/CNT when the device is illuminated.

Finally we also investigated the effect of foreign objects attached on the bodies of the nanotubes. It was found that gas molecules on the nanotubes behave as scattering centers,

which increase the device resistance and relax the electron spin polarization. By passing high currents through the nanotubes, the molecules are dislodged and the intrinsic properties are revealed. For example, the long spin coherence length in CNT is shown by observation of spin valve effect in nanotube devices with channel length of several hundreds of nanometers, after annealing the devices with current. Such an effect is then attributed to the interaction between the molecules and the high-energy phonons excited by electron-phonon coupling.

All of the studies indeed demonstrate the complexity of nanoscience, as mentioned above, but simultaneously help us understand more about the mesoscopic world. Standing on the contributions from many others, this thesis also contributes to the knowledge database of the mesoscopic world. If the study of the mesoscopic system is a journey to explore the linkage between the macroscopic and microscopic worlds, it is the journey that this thesis has joined.

Appendix A

Device Fabrication and Measurement Set-up

In this appendix, details of sample-fabrication processes are described. They include the sample preparation, electrical measurement set-up and the low-temperature technique. The description of each of them is given separately in the following sections

A.1 Sample preparation

The substrates used in the experiments presented in chapter 4 and 6 are made by silicon wafers and in chapter 5 are made by GaAs. Except for the difference in the substrate materials, all of these devices share the same techniques, e.g. nanotube adsorption and electron-beam lithography (EBL). The full process of the sample preparation is illustrated in Figure A.1

Nanotube adsorption

The nanotube raw material used for the experiments in this thesis is made by the laser ablation technique. Once it is made and extracted from the production chamber, it is in the form of powder or entangled whiskers (Figure A.1 **I**). In order to make devices from individual nanotubes, it is necessary to isolate the nanotubes and place them on to the substrate. Figure A.1 **I** to **III** show the process of the nanotube adsorption, which is applied to both of the Si and GaAs substrates. In detail, the process starts with making liquid suspension of nanotubes. Since nanotubes are hydrophobic and insoluble in water, surfactant is needed to make a water-based nanotube suspension. It has been reported that sodium dodecyl sulfonate (SDS) serves as a suitable surfactant, being able to homogeneously suspend and de-bundle the nanotubes in water. In our experiment, the raw material is suspended in a 1-weight-percent (wt%) aqueous solution of SDS by sonication, as shown in Figure A.1 **II**. SDS molecules ionize in water, leaving a charged end in the

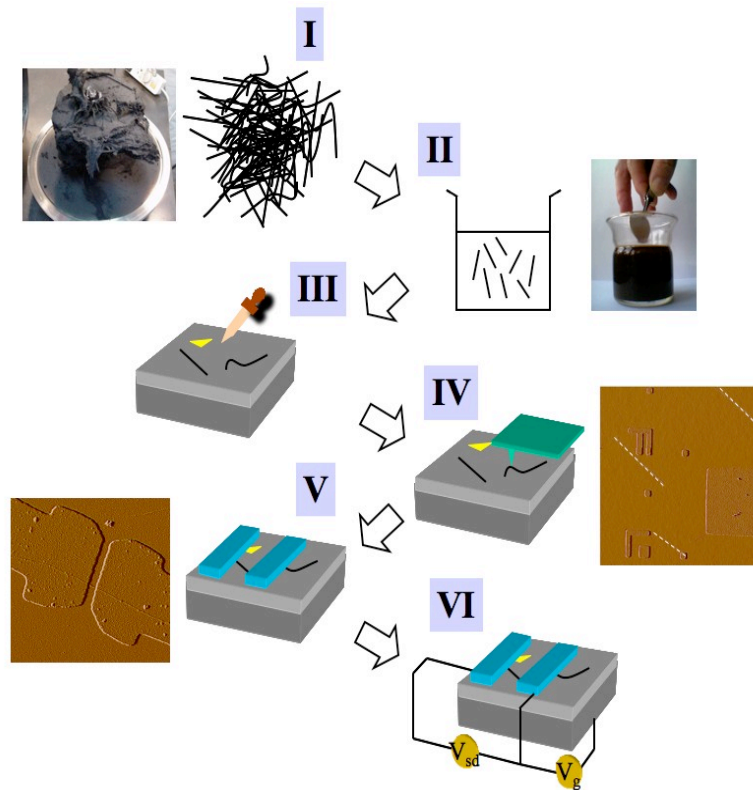


Figure A.1 Process flow of the fabrication of nanotube devices (sketches and images). **I.** Production of raw materials. **II.** Dispersion of the nanotubes in the solvent. **III.** Transfer of the nanotubes to the substrate. **IV.** Locating the nanotubes with respect to the markers by AFM. White dashed lines mark the nanotubes laying on the substrate. **V.** Making the metal electrodes **VI.** Installation of measurement set-up.

water and keeping another end attached to the nanotubes. CNTs covered by SDS thus become polarized and water-soluble. Instead of steady equilibrium, the solution is actually in a dynamic one: SDS attaches to the SWNT surface and leaves alternatively.[BDP]

After suspending and isolating the nanotubes they are to be transferred to the substrate. A simple method to adsorb the nanotubes is to put a droplet of the suspension on the substrate and to wait for nanotubes to fall onto the substrate surface. After removing the droplet by the blow-drying with argon gas, samples are immersed in deionized water to wash away the SDS from the nanotube surface. An atomic force microscope (AFM) is used to locate the isolated nanotubes on the substrate according to the previously fabricated markers, as shown in Figure A.1 **IV**. With the AFM images, one can proceed with the lithography process to make the metal contacts. Here we noticed that nanotubes adsorbed in this way

tend to incline toward the direction of the Ar flow.

Electron beam lithography (EBL)

Figure A.2 shows the flowchart illustrating the EBL technique, which is commonly applied to the device fabrication on the nanoscale. The substrate is first covered with PMMA resist (Poly-methyl-methacrylate) via spin-coating and baked in the oven (160 °C, 1 hour). To make a desired pattern on the PMMA, the substrate is then loaded into an electron beam (e-beam) writer that exposes the PMMA with accelerated electrons. After the exposure, substrates are washed in a mixed organic solvent with methyl-isobutyl-ketone (MIBK) diluted in 2-propanol (IPA) in 1:3 volume ratio. The exposed area of PMMA dissolves in the MIBK while the other unexposed part remains stable, resulting in the development of the written structure. The development process lasts for 45 s and afterwards samples are transferred to pure IPA for another 45 s. A fully developed substrate is ready for thin film metal deposition. To do so, the substrates are loaded into a machine like evaporator or sputterer, depending on the required materials to deposit the thin films. After the thin film deposition, the substrate is transferred to a warm n-Methylpyrrolidone (NMP) bath (55 °C, 2 hours) to remove the rest of the PMMA. Once the PMMA has been removed completely, the substrate is cleaned with acetone and then IPA. This step is called lift-off. It should be emphasized here that in our experiments, double-layer PMMA (300K, 950K) with different e-beam sensitivities was used to improve the undercut structure. The undercut structure increases the yield of successful lift-off process. After the lift-off, a metal thin-film was left on the substrate at the desired place.

A.2 Electrical measurements

To perform the electrical measurement on an individual nanotube, the substrate with contacted nanotubes is attached to a chip carrier with multiple metal pins, as show in Figure A.3. The contact pads on the chip are bonded by gold wires to the metal pins. The carrier is further installed into a stick with cables connecting to a switch box. But prior to the chip carrier installation, all of the metal pins is short-circuited by additional gold wires, which will be removed after the installation. This is to protect the device against distruction by charge pulses (electrostatic discharge). The switch box has an array of BNC connectors

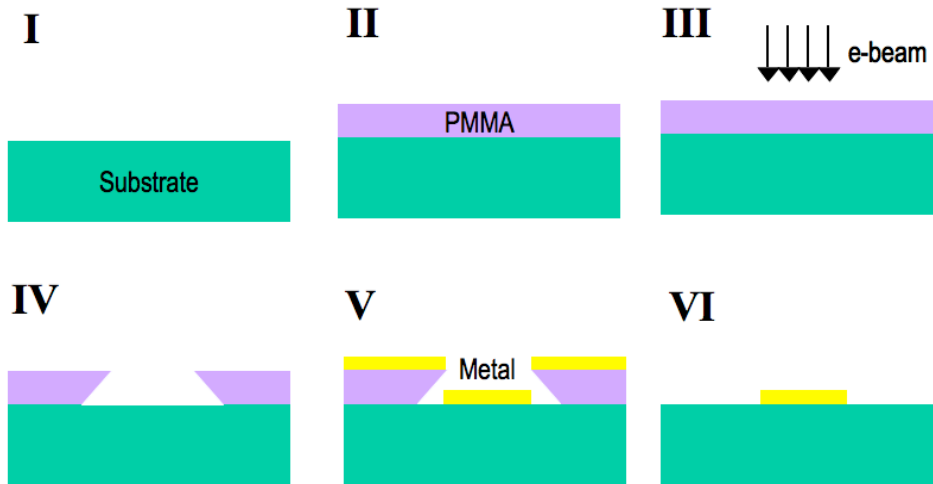


Figure A.2 Electron beam lithography. I. Preparation of substrates. II. Spin coating of PMMA. III. E-beam exposure. IV. Development of the resist after exposure. V. Deposition of the metal film. VI. Remove the PMMA with lift-off process.

and each of them independently connects to the metal pins of the chip carrier. With this set-up, one can switch the metal pins between ground and floating separately. The electronics for sourcing and reading the electrical signals are collected in a rack together with the switch box. Sourcemeters (Keithley 2400) are used to apply the voltage and current. Multimeters (Keithley 2000) are employed to read the voltage signals. The current signals are first amplified and converted into voltage signals by an amplifier and then read by the multimeter. When performing the measurement, the stick is enclosed in a sealed steel tube. This allows to perform the measurement under different atmospheres.

A.3 Low-temperature techniques

In addition to the measurements at room temperature, low-temperature measurements were also carried out down to 4.2 K in a cryostat (Cryogenic Ltd.) whose inner chamber is filled with liquid Helium. On the top of the cryostat, there is a hole left for the insertion of the stick into its inner chamber. The cryostat is equipped with a superconducting magnet, with which magnetic fields up to 6T can be generated. While inserting (pulling) the stick, the temperature experienced by the sample gradually decreases (increases). This enables

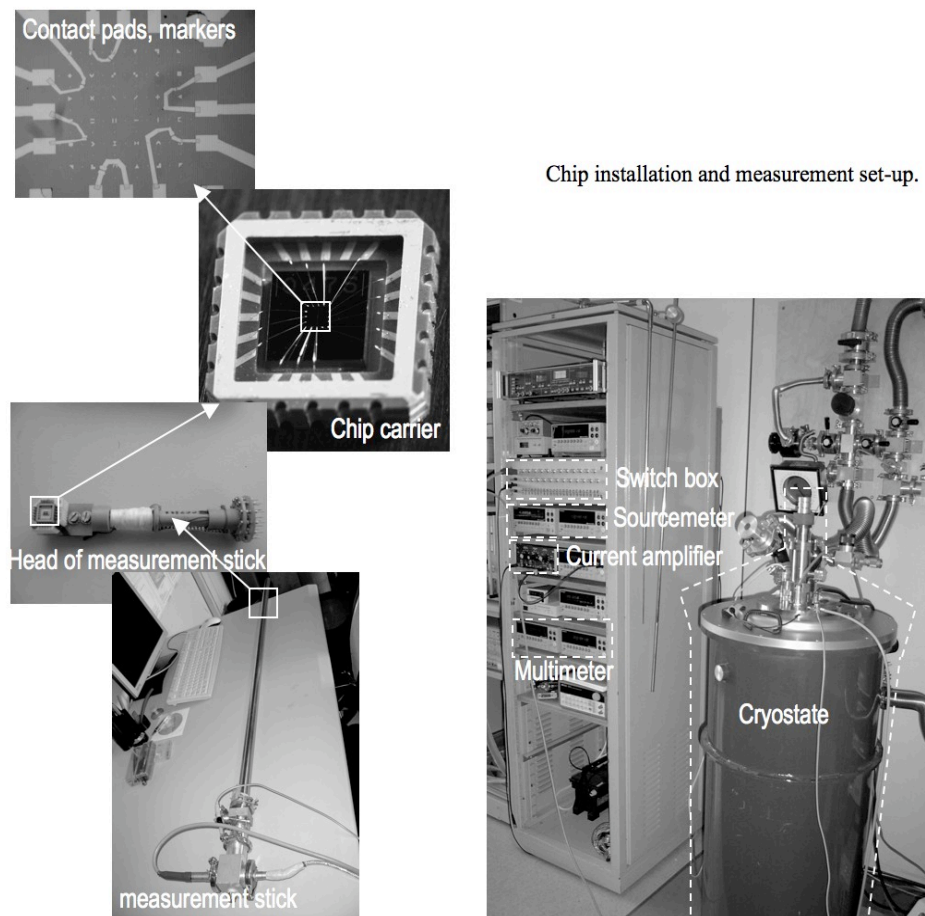


Figure A.3 Measurement set-up for the nanotube electronics.

the measurement over a temperature range from 4.2 K to room temperature.

Appendix B

High-Bias Transport in Carbon Nanotubes

The transport properties of a nanotube are different in the two regimes: electrons with energy (1) close to or (2) significantly in excess of the Fermi level. Electrons with Fermi energy have a long mean-free path due to the suppression of elastic backscattering by the long-range disorder. When their energy rises to a level well above the Fermi energy, it was observed that another scattering mechanism evolves and results in a increasing resistance at the high-field transport regime, as shown in Figure B.1a. Such a phenomenon was first observed by Yao, et al. The resistance increases with the increase of the bias voltage. Higher voltage impedes the current more and finally makes it saturate at a certain value. This result was followed by a series of studies and it was found that current saturates with

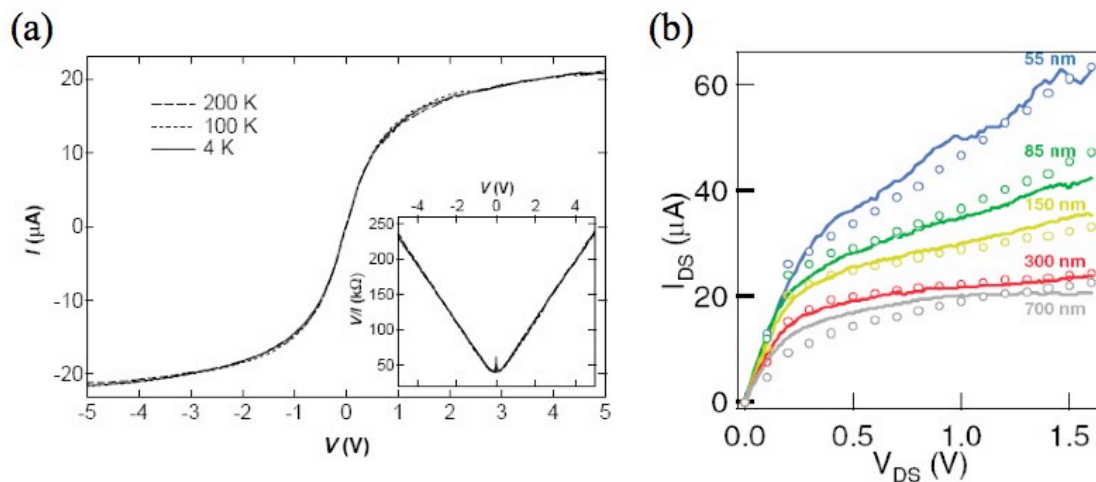


Figure B.1 High-field transport of nanotubes. (a) non-linear behavior shows at the high-voltage region, where the saturation of current is expected to be $25 \mu\text{A}$. Inset: the resistance increases along with the increase of bias voltage (picture adopted from [YKD]). (b) comparison of the high-field transport of nanotubes with different length. The current saturation increases with shorter nanotubes (picture adopted from [JGP]).

higher value at large bias voltage in shorter nanotubes (Figure B.1b). At an extreme condition like a suspended nanotube, the current even decreases while increasing the bias voltage, resulting in a regime of negative differential conductance (Figure B.2a).

The mechanism behind the result is ascribed to the electron-phonon coupling (EPC) in the nanotube. The coupling of the electron and phonon is described as

$$E_{k+q} = E_k \pm \hbar \Omega_q, \quad \text{B.1}$$

where the E is the electron energy, k and q is the electron and phonon wave vectors, Ω is the Debye frequency. The plus/minus sign refers to the adsorption/emission of the phonon. Eq. B.1 formulates the exchange of the energy and the momentum between the electron and phonon through the coupling. As shown in Figure B.2b and c, electrons and phonons couple in different ways, depending on the exchange. This results in the different scattering rate, τ , and different mean-free path, L_m , for the phonon-assisted scattering.

At lower bias, the electrons have smaller energy and couple only with the acoustic phonons with smaller energy exchange. The scattering rate, τ_{ac} , and the mean-free path, L_{ac} , in this condition are in the range of ps and μm respectively.[PRY] It should be noticed that when the nanotube length is smaller than the L_{ac} , such a scattering can be then neglected. In the absence of acoustic-phonon scattering, ballistic transport is exhibited in the nanotubes even up to room temperature. However, when the bias is increased, energetic electrons injected into the nanotube are able to exchange larger amount of energy with phonons, resulting in the emission of the high-energy phonons. The scattering rate, τ_{hp} , and the mean free path, L_{hp} , of the electrons scattered by the high-energy phonons is about sub-ps and hundred nm respectively. This is a scattering mechanism much stronger than the acoustic-phonon scattering.

The high-energy-phonon scattering becomes more severe when the nanotube is suspended. The population of the high-energy phonons in a suspended nanotube will build up quickly because the emitted phonons cannot be dissipated to the substrate. This results in the negative differential conductance. However, for those nanotubes shorter than 100 nm, the scattering rate becomes less important because the length is smaller than L_{hp} . Therefore the transport is ballistic at higher bias and the current saturation appears at higher voltages.

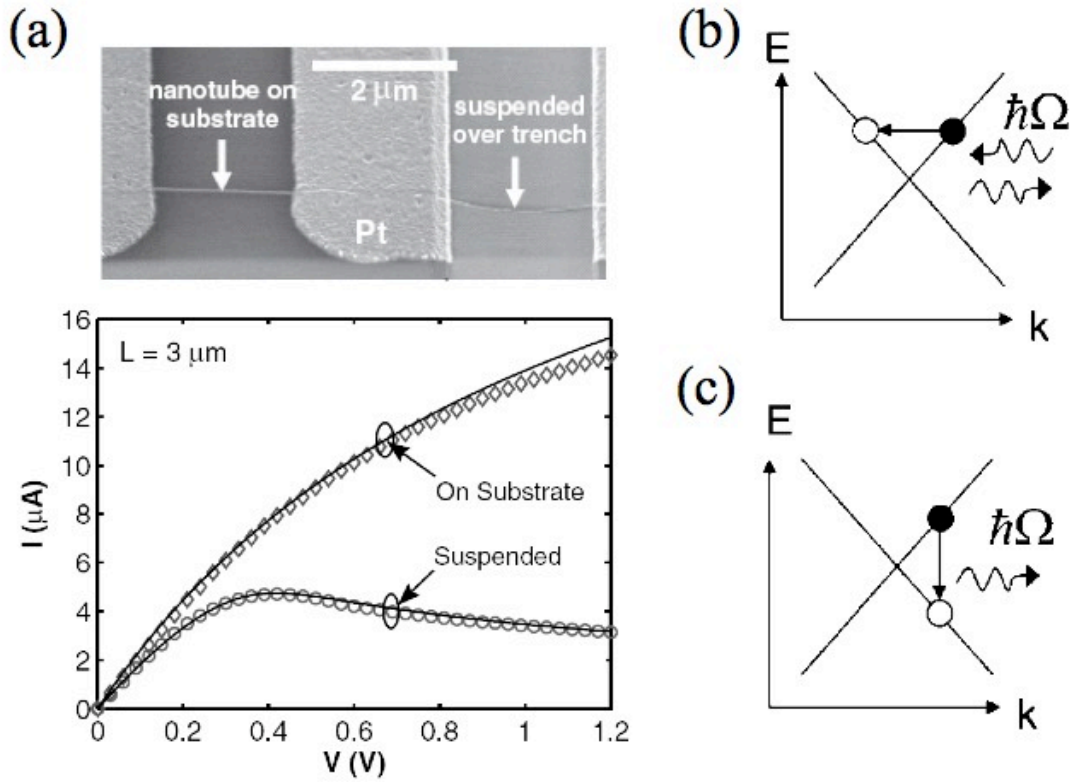


Figure B.2 (a) High-field transport of the nanotubes with or without the support of substrate. For the suspended nanotube, the negative differential conductance appears when the voltage is larger than 0.4 V. Picture adopted from [PMC] (b) Emission and absorption of an acoustic phonon with low energy and small momentum. (c) Emission of an optical phonon with high energy and small momentum (Picture adopted from [PRY]).

Bibliography

[AA] H. Ajiki and T. Ando, Electronic states of carbon nanotubes. *J. Phys. Soc. Jpn.* **62**, 1255, 1992.

[ABC] D. M. Adams, L. Brus, C. E. D. Chidsey, S. Creager, C. Creutz, C. R. Kagan, P. V. Kamat, M. Lieberman, S. Lindsay, R. A. Marcus, R. M. Metzger, M. E. Michel-Beyerle, J. R. Miller, M. D. Newton, D. R. Rolison, O. Sankey, K. S. Schanze, J. Yardley and X. Zhu, Charge transfer on the nanoscale: Current status. *J. Phys. Chem. B* **107**, 6668, 2003.

[ACP] Ph. Avouris, Z. Chen and V.i Perebeinos, Carbon-based electronics. *Nat. Nanotechnol.* **2**, 605, 2007.

[AM] N. Aschroff and H. Mermin, *Solid state physics*. Brooks Cole, 1976.

[And] R. L. Anderson, Experiments on Ge-GaAs heterojunctions. *Solid-State Electron.* **5**, 341, 1962.

[ARK] J. Appenzeller¹, M. Radosavljević, J. Knoch and Ph. Avouris, Tunneling versus thermionic emission in one-dimensional semiconductors. *Phys. Rev. Lett.* **92**, 048301, 2004.

[Bas] Nano-Electronics at University Basel, <http://pages.unibas.ch/phys-meso/Pictures/Pictures/Images/cavity.gif>.

[BBF] M. N. Baibich, J. M. Broto, A. Fert, F. Nguyen Van Dau, F. Petroff, P. Eitenne, G. Creuzet, A. Friederich and J. Chazelas, Giant magnetoresistance of (001)Fe/(001)Cr magnetic superlattices. *Phys. Rev. Lett.* **61**, 2472, 1988.

[BBF] M. N. Baibich, J. M. Broto, A. Fert, F. Nguyen Van Dau, F. Petroff, P. Eitenne, G. Creuzet, A. Friederich and J. Chazelas, Giant magnetoresistance of (001)Fe/(001)Cr magnetic superlattices. **61**, 2472, 1988.

[BDP] M. Burghard, G. Duesberg, G. Philipp, J. Muster, S. Roth, Controlled adsorption of carbon nanotubes on chemically modified electrode arrays. *Adv. Mater.* **10**, 554, 1998.

[BGS] G. Binasch, P. Grünberg, F. Saurenbach, and W. Zinn, Enhanced magnetoresistance in layered magnetic structures with antiferromagnetic interlayer exchange. *Phys. Rev. B* **39**, 4828, 1989.

[BHN] A. Bachtold, P. Hadley, T. Nakanishi and C. Dekker, Logic circuits with carbon nanotube transistors. *Science* **294**, 1317, 2001.

[BHW] R. H. Blick, R. J. Haug, J. Weis, D. Pfannkuche, K. v. Klitzing and K. Eberl, Single-electron tunneling through a double quantum dot: The artificial molecule. *Phys. Rev. B* **53**, 7899, 1996.

[BJC] K. Bradley, S. H. Jhi, P. G. Collins, J. Hone, M. L. Cohen, S. G. Louie and A. Zettl, Is the intrinsic thermoelectric power of carbon nanotubes positive?. *Phys. Rev. Lett.* **85**, 4361, 2000.

[BSJ] K. I. Bolotin, K. J. Sikes, Z. Jiang, M. Klima, G. Fudenberg, J. Hone, P. Kim and H. L. Stormer, Ultrahigh electron mobility in suspended graphene. *Solid State Comm.* **146**,

351, 2008.

[CAK] Z. Chen, J. Appenzeller, J. Knoch, Y. M. Lin and Ph. Avouris, The role of metal-nanotube contact in the performance of carbon nanotube field-effect transistors. *Nano Lett.* **5**, 1497, 2005.

[CBI] P. G. Collins, K. Bradley, M. Ishigami and A. Zettl, Extreme oxygen sensitivity of electronic properties of carbon nanotubes. *Science* **287**, 1801, 2000.

[CCF] S. Cho, Y. Chen and M. S. Fuhrer, Gate-tunable graphene spin valve. *Appl. Phys. Lett.* **91**, 123105, 2007.

[CCH] M. T. Chang, L. J. Chou, C. H. Hsieh, Y. L. Chueh, Z. L. Wang, Y. Murakami and D. Shindo, Magnetic and electrical characterizations of half-metallic Fe₃O₄ nanowires. *Adv. Mat.* **19**, 2290, 2007.

[CF] Y.-F. Chen and M. S. Fuhrer, Tuning from Thermionic Emission to Ohmic Tunnel Contacts via Doping in Schottky-Barrier Nanotube Transistors. *Nano Lett.* **6**, 2158, 2006.

[CMG] S. Chopra, K. McGuire, N. Gothard, A. M. Rao and A. Pham, Selective gas detection using a carbon nanotube sensor. *Appl. Phys. Lett.* **83**, 2280, 2003.

[CNR] Laboratory for Photonics and Nanostructures, CNRS,
http://www.lpn.cnrs.fr/en/ELPHYSE/FaitsMarquants/FM_ELPHYSE_Resonano.php.

[CST] R. B. Capaz, C. D. Spataru, P. Tangney, M. L. Cohen and S. G. Louie, Temperature Dependence of the Band Gap of Semiconducting Carbon Nanotubes. *Phys. Rev. Lett.* **94**, 036801, 2005.

[CWD] J. Cao, Q. Wang and H. Dai, Electron transport in very clean, as-grown suspended carbon nanotubes. *Nat. Mater.* **4**, 745, 2005.

[DAT] S. Datta, *Electronic transport in mesoscopic system*. Cambridge University Press, 1995.

[DCA] J. J. Davis, K. S. Coleman, B. R. Azamian, C. B. Bagshaw, M. L. H. Green, Chemical and biochemical sensing with modified single walled carbon nanotubes. *Chem. Eur. J.* **9**, 3732, 2003.

[DD] S. Datta and B. Das, Electronic analog of the electro-optic modulator. *Appl. Phys. Lett.* **56**, 665, 1990.

[DGC] T. Dürkop, S. A. Getty, Enrique Cobas and M. S. Fuhrer, Extraordinary mobility in semiconducting carbon nanotubes. *Nano Lett.* **4**, 35, 2004.

[DMA] V. Derycke, R. Martel, J. Appenzeller and Ph. Avouris, Controlling doping and carrier injection in carbon nanotube transistors. *Appl. Phys. Lett.* **80**, 2773, 2002.

[DMM] V. Dediu, M. Murgias, F. C. Maticotaa, C. Taliania and S. Barbanerab, Room temperature spin polarized injection in organic semiconductor. *Solid State Comm.* **122**, 181, 2002.

[DP] M. I. Dyakonov and V. I. Perel, Possibility of orientating electron spins with current. *Sov. Phys. JETP Lett.* **13**, 467, 1971.

- [FPW] S. Frank, P. Poncharal, Z. L. Wang and W. A. de Heer, Carbon nanotube quantum resistors. *Science* **280**, 1744, 1998.
- [FVY] S. M. Frolov, A. Venkatesan, W. Yu, S. Luescher, W. Wegscheider and J. A. Folk, Electrical generation of pure spin currents in a two-dimensional electron gas, *arXiv:cond-mat/0801.4021*, 2008.
- [GD] H. Grabert and M. H. Devoret (Eds), *Single Electron Tunneling: Coulomb Blockade Phenomena in Nanostructure*. Plenum New York, 1992.
- [GI] Graphene Industries, <http://www.grapheneindustries.com/?Products>.
- [GN] A. K. Geim and K. S. Novoselov, The rise of graphene. *Nat. Mat.* **6**, 183, 2007.
- [Her] G. Hernandez, *Fabry-Pérot Interferometers*. Cambridge University Press, 1986.
- [HGN] E. W. Hill, A. K. Geim, K. Novoselov, F. Schedin and P. Blake, Graphene spin valve devices. *IEEE Trans. Mag.* **42**, 2694, 2006.
- [Hir] J.E. Hirsch, Spin hall effect. *Phys. Rev. Lett.* **83**, 1843, 1999.
- [HPF] L. E. Hueso, J. M. Pruneda, V. Ferrari, G. Burnell, J. Valdés-Herrera, B. Simons, P. B. Littlewood, E. Artacho, A. Fert and M. D. Mathur, Transformation of spin information into large electrical signals using carbon nanotubes. *Nature* **445**, 410, 2007.
- [HSO] N. Hamada, S. Sawada and A. Oshiyama, New one-dimensional conductors: Graphitic microtubules. *Phys. Rev. Lett.* **68**, 1579, 1992.
- [HTM] S. Heinze, J. Tersoff, R. Martel, V. Derycke, J. Appenzeller and Ph. Avouris, Carbon nanotubes as schottky barrier transistors. *Phys. Rev. Lett.* **89**, 106801, 2002.
- [Iij] S. Iijima, Helical microtubules of graphitic carbon. *Nature* **354**, 56, 1991.
- [JFW] F. J. Jedema, A. T. Filip and B. J. van Wees, Electrical spin injection and accumulation at room temperature in an all-metal mesoscopic spin valve. *Nature* **410**, 345, 2001.
- [JGN] H. I. Jørgensen, K. Grove-Rasmussen, T. Novotny, K. Flensberg and P. E. Lindelof, Electron transport in single-wall carbon nanotube weak links in the Fabry-Perot regime. *Phys. Rev. Lett.* **96**, 207003, 2006.
- [JGP] A. Javey, J. Guo, M. Paulsson, Q. Wang, D. Mann, M. Lundstrom and H. Dai, High-field quasiballistic transport in short carbon nanotubes. *Phys. Rev. Lett.* **92**, 106804, 2004.
- [JGW] A. Javey, J. Guo, Q. Wang, M. Lundstrom and H. Dai, Ballistic carbon nanotube field-effect transistors. *Nature* **424**, 654, 2003.
- [JHN] A. Jensen, J. R. Hauptmann, J. Nygård and P. E. Lindelof, Magnetoresistance in ferromagnetically contacted single-wall carbon nanotubes. *Phys. Rev. B* **72**, 035419, 2005.
- [JIN] R. A. Jishi, D. Inomata, K. Nakao, M. S. Dresselhaus and G. Dresselhaus, Electronic and lattice properties of carbon nanotubes. *J. Phys. Soc. Jpn.* **63**, 2252, .
- [JLC] S. H. Jhi, S. G. Louie and M. L. Cohen, Electronic properties of oxidized carbon nanotubes. *Phys. Rev. Lett.* **85**, 1710, 2000.

- [**JS**] M. Johnson and R. H. Silsbee, Interfacial charge-spin coupling: Injection and detection of spin magnetization in metals. *Phys. Rev. Lett.* **55**, 1790, 1985.
- [**JWK**] A. Javey, Q. Wang, W. Kim and H. Dai, Advancements in complementary carbon nanotube field-effect transistors. *IEEE Int. Electron Devices Meet.* , 32.2.1, 2003.
- [**KAT**] L. P. Kouwenhoven, D. G. Austing and S. Tarucha, Few-electron quantum dots. *Rep. Prog. Phys.* **64**, 701, 2001.
- [**Ken**] P. Kent, <http://www.physics.uc.edu/~pkent/pictures/c60.html>.
- [**KHL**] R. Krupke, F. Hennrich, H. v. Löhneysen, M. M. Kappes, Separation of metallic from semiconducting single-walled carbon nanotubes. *Science* **301**, 344, 2003.
- [**KHO**] H. W. Kroto, J. R. Heath, S. C. O'Brien, R. F. Curl and R. E. Smalley, C60: Buckminsterfullerene. *Nature* **318**, 162, 1985.
- [**KIR**] F. Kuemmeth, S. Ilani, D. C. Ralph and P. L. McEuen, Coupling of spin and orbital motion of electrons in carbon nanotubes. *Nature* **452**, 448, 2008.
- [**Kit**] C. Kittel, *Introduction to solid state physics*. Wiley, 1995.
- [**KJV**] W. Kim, A. Javey, O. Vermesh, Q. Wang, Y. Li and H. Dai, Hysteresis caused by water molecules in carbon nanotube field effect transistors. *Nano Lett.* **3**, 193, 2003.
- [**KM**] L. P. Kouwenhoven and C. Marcus, Quantum dots. *Physics World June*, 35, 1998.
- [**KMG**] Y. Kato, R. C. Myers, A. C. Gossard and D. D. Awschalom, Observation of the spin hall effect in semiconductors. *Science* **306**, 5703, 2004.
- [**KNG**] M. I. Katsnelson, K. S. Novoselov and A. K. Geim, Chiral tunnelling and the klein paradox in graphene. *Nature Physics* **2**, 620, 2006.
- [**KYT**] J. Kong, E. Yenilmez, T. W. Tombler, W. Kim, H. Dai, R. B. Laughlin, L. Liu, C. S. Jayanthi and S. Y. Wu, Quantum interference and ballistic transmission in nanotube electron waveguides. *Phys. Rev. Lett.* **87**, 106801, 2001.
- [**LBB**] W. Liang, M. Bockrath, D. Bozovic, J. H. Hafner, M. Tinkham and H. Park, Fabry - Perot interference in a nanotube electron waveguide. *Nature* **411**, 665, 2001.
- [**LBP**] W. Liang, M. Bockrath and H. Park, Shell filling and exchange coupling in metallic single-walled carbon nanotubes. *Phys. Rev. Lett.* **88**, 126801, 2002.
- [**LLL**] H. J. Li, W. G. Lu, J. J. Li, X. D. Bai and C. Z. Gu, Multichannel ballistic transport in multiwall carbon nanotubes. *Phys. Rev. Lett.* **95**, 086601, 2005.
- [**LLY**] J. Li, Y. Lu, Q. Ye, M. Cinke, J. Han and M. Meyyappan, Carbon nanotubes sensors for gas and organic vapor detection. *Nano Lett.* **3**, 929, 2003.
- [**LPM**] M. Lazzeri, S. Piscanec, F. Mauri, A. C. Ferrari and J. Robertson, Electron transport and hot phonons in carbon nanotubes. *Phys. Rev. Lett.* **95**, 236802, 2005.
- [**LWS**] J. H. Lee, Zh. M. Wang, N. W. Strom, Yu. I. Mazur and G. J. Salamo, InGaAs quantum dot molecules around self-assembled GaAs nanomound templates. *Appl. Phys. Lett.* **89**, 202101, 2006.

- [**MBM**] N. Mason, M. J. Biercuk and C. M. Marcus, Local gate control of a carbon nanotube double quantum dot. *Science* **33**, 655, 2004.
- [**MDL**] R. Martel, V. Derycke, C. Lavoie, J. Appenzeller, K. K. Chan, J. Tersoff and Ph. Avouris, Ambipolar electrical transport in semiconducting single-wall carbon nanotubes. *Phys. Rev. Lett.* **87**, 256805, 2001.
- [**MDW**] J. W. Mintmire, B. I. Dunlap and C. T. White, Are fullerene tubules metallic?. *Phys. Rev. Lett.* **68**, 631, 1992.
- [**MG**] J. C. Meyer, A.K. Geim, M. I. Katsnelson, K. S. Novoselov, T. J. Booth and S. Roth, The structure of suspended graphene sheets. *Nature* **446**, 60, 2007.
- [**MNK**] S. V. Morozov, K. S. Novoselov, M. I. Katsnelson, F. Schedin, D. C. Elias, J. A. Jaszczak and A. K. Geim, Giant intrinsic carrier mobilities in graphene and its bilayer. *Phys. Rev. Lett.* **100**, 016602, 2008.
- [**MSS**] R. Martel, T. Schmidt, H. R. Shea, T. Hertel and Ph. Avouris, Single- and multi-wall carbon nanotube field-effect transistors. *Appl. Phys. Lett.* **73**, 2447, 1998.
- [**MUG**] I. L. Medintz, H. T. Uyeda, E. R. Goldman and H.i Mattoussi, Quantum dot bioconjugates for imaging, labelling and sensing. *Nat. Mater.* **4**, 435, 2005.
- [**MWS**] H. M. Manohara, E. W. Wong, E. Schlecht, B. D. Hunt and P. H. Siegel, Carbon nanotube Schottky diodes using Ti-Schottky and Pt-ohmic contacts for high Frequency Applications. *Nano Lett.* **5**, 1469, 2005.
- [**NBS**] B. Nagabhirava, T. Bansal, G. U. Sumanasekera, B. W. Alphenaar and L. Liu, Gated spin transport through an individual single wall carbon nanotube. *Appl. Phys. Lett.* **88**, 023503, 2006.
- [**NG04**] K. S. Novoselov, A. K. Geim, S. V. Morozov, D. Jiang, Y. Zhang, S. V. Dubonos, I. V. Grigorieva and A. A. Firsov, Electric field effect in atomically thin carbon films. *Science* **306**, 666, 2004.
- [**NG05**] K. S. Novoselov, A. K. Geim, S. V. Morozov, D. Jiang, M. I. Katsnelson, I. V. Grigorieva, S. V. Dubonos and A. A. Firsov, Two-dimensional gas of massless dirac fermions in graphene. *Nature* **438**, 197, 2005.
- [**NIM**] NIMS, <http://www.nims.go.jp/apfim/gif/CCP-CPP-GMR.gif>.
- [**NJZ**] K.S. Novoselov, Z. Jiang, Y. Zhang, S.V. Morozov, H.L. Stormer, U. Zeitler, J.C. Maan, G.S. Boebinger, P. Kim and A.K. Geim, Room-temperature quantum hall effect in graphene. *Science* **315**, 1379, 2007.
- [**NKZ**] J. Kong, N. R. Franklin, C. Zhou, M. G. Chapline, S. Peng, K. Cho, H. Dai, Nanotube molecular wires as chemical sensors. *Nature* **287**, 622, 2000.
- [**Nob**] Nobel2007, http://nobelprize.org/nobel_prizes/physics/laureates/2007/index.html.
- [**OSM**] H. Ohno, A. Shen, F. Matsukura, A. Oiwa, A. Endo, S. Katsumoto and Y. Iye, (Ga,Mn)As: A new diluted magnetic semiconductor based on GaAs. *Appl. Phys. Lett.* **69**, 363, 1996.
- [**PMC**] E. Pop, D. Mann, J. Cao, Q. Wang, K. Goodson and H. Dai, Negative differential

conductance and hot phonons in suspended nanotube molecular wires. *Phys. Rev. Lett.* **95**, 155505, 2005.

[PPG] J. Park, A. N. Pasupathy, J. I. Goldsmith, C. Chang, Y. Yaish, J. R. Petta, M. Rinkoski, J. P. Sethna, H. D. Abruña, P. L. McEuen and D. C. Ralph, Coulomb blockade and the Kondo effect in single-atom transistors. *Nature* **417**, 722, 2002.

[PRY] J.-Y. Park, S. Rosenblatt, Y. Yaish, V. Sazonova, H. Üstünel, S. Braig, T. A. Arias, P. W. Brouwer and P. L. McEuen, Electron-phonon scattering in metallic single-walled carbon nanotubes. *Nano Lett.* **4**, 517, 2004.

[PTZ] F. Patolsky, B. P. Timko, G. Zheng and C. M. Lieber, Nanowire-based nanoelectronic devices in the life sciences. *MRS Bull.* **32**, 142, 2007.

[QPH] L. Qin, S. Park, L. Huang, C. A. Mirkin, On-wire lithography. *Science* **309**, 113, 2005.

[RF] A. R. Riben and D. L. Feucht, nGe---pGaAs Heterojunctions. *Solid-State Electron.* **9**, 1055, 1966.

[RGJ] C. Rüster, C. Gould, T. Jungwirth, J. Sinova, G. M. Schott, R. Giraud, K. Brunner, G. Schmidt and L. W. Molenkamp, Very large tunneling anisotropic magnetoresistance of a (Ga,Mn)As/GaAs/(Ga,Mn)As stack. *Phys. Rev. Lett.* **94**, 027203, 2005.

[SAF] G. U. Sumanasekera, C. K. W. Adu, S. Fang and P. C. Eklund, Effects of gas adsorption and collisions on electrical transport in single-walled carbon nanotubes. *Phys. Rev. Lett.* **85**, 1096, 2000.

[SDD] R. Saito, G. Dresselhaus and M. S. Dresselhaus, *Physical properties of carbon nanotubes*. Imperial College Press, 1998.

[SGK] R. V. Seidel, A. P. Graham, J. Kretz, B. Rajasekharan, G. S. Duesberg, M. Liebau, E. Unger, F. Kreupl and W. Hoenlein, Sub-20 nm short channel carbon nanotube transistors. *Nano Lett.* **5**, 147, 2004.

[SKF] S. Sahoo, T. Kontos, J. Furer, C. Hoffmann, M. Gräber, A. Cottet and C. Schönenberger, Electric field control of spin transport. *Nat. Phys.* **1**, 99, 2005.

[SMB] S. Sapmaz, C. Meyer, P. Beliczynski, P. Jarillo-Herrero and L. P. Kouwenhoven, Excited state spectroscopy in carbon nanotube double quantum dots. *Nano Lett.* **6**, 1350, 2006.

[SNN] O. Suekane, A. Nagataki, Y. Nakayama, Current-induced curing of defective carbon nanotubes. *Appl. Phys. Lett.* **89**, 183110, 2006.

[SPK] F. Simon, R. Pfeiffer and Hans Kuzmany, Temperature dependence of the optical excitation lifetime and band gap in chirality assigned semiconducting single-wall carbon nanotubes. *Phys. Rev. B* **74**, 121411, 2006.

[STF] S. Sahoo, T. Kontos, J. Furer, C. Hoffmann, M. Gräber, A. Cottet and C. Schönenberger, Electric field control of spin transport. *Nat. Phys.* **1**, 99, 2005.

[Sur] S. Suresh, Graded materials for resistance to contact deformation and damage. *Science* **292**, 2447, 2001.

- [Sze] S. M. Sze, *Physics of semiconductor devices*. John Wiley and Sons, 1981.
- [TAA] K. Tsukagoshi, B. W. Alphenaar and H. Ago, Coherent transport of electron spin in a ferromagnetically contacted carbon nanotube. *Nature* **401**, 572, 1999.
- [TDD] S. J. Tans, M. H. Devoret, H. Dai, A. Thess, R. E. Smalley, L. J. Geerligs and C. Dekker, Individual single-wall carbon nanotubes as quantum wires. *Nature* **386**, 474, 1997.
- [TJP] N. Tombros, C. Jozsa, M. Popinciuc, H. T. Jonkman and B. J. van Wees, Electronic spin transport and spin precession in single graphene layers at room temperature. *Nature* **448**, 571, 2007.
- [TVD] S. J. Tans, A. R. M. Verschueren and C. Dekker, Room-temperature transistor based on a single carbon nanotube. *Nature* **393**, 49, 1998.
- [UPH] V. Umansky, R. de-Picciotto and M. Heiblum, Extremely high-mobility two dimensional electron gas: Evaluation of scattering mechanisms. *Appl. Phys. Lett.* **71**, 683, 1997.
- [Var] Y. P. Varshni, Temperature dependence of the energy gap in semiconductors. *Physica* **34**, 149, 1967.
- [vH] L. van Hove, The occurrence of singularities in the elastic frequency distribution of a crystal. *Phys. Rev.* **89**, 1189, 1953.
- [VT] S.O. Valenzuela; M. Tinkham, Direct Electronic Measurement of the Spin Hall Effect. *Nature* **442**, 176, 2006.
- [WAB] S. A. Wolf, D. D. Awschalom, R. A. Buhrman, J. M. Daughton, S. von Molnár, M. L. Roukes, A. Y. Chtchelkanova, D. M. Treger, Spintronics: A spin-based electronics vision for the future. *Science* **294**, 1488, 2001.
- [WG] D. C. Worledge and T. H. Geballe, Spin-polarized tunneling in La_{0.67}Sr_{0.33}MnO₃. *Appl. Phys. Lett.* **76**, 900, 2000.
- [WHK] J. Weis, R. J. Haug, K. v. Klitzing and K. Ploog, Competing channels in single-electron tunneling through a quantum dot. *Phys. Rev. Lett.* **71**, 4019, 1993.
- [WHL] D. Waldron, P. Haney, B. Larade, A. MacDonald and H. Guo, Nonlinear spin current and magnetoresistance of molecular tunnel junctions. *Phys. Rev. Lett.* **96**, 166804, 2006.
- [Wik] Wikipedia, http://en.wikipedia.org/wiki/Fabry-P%C3%A9rot_interferometer.
- [WT] C. T. White and T. N. Todorov, Carbon nanotubes as long ballistic conductors. *Nature* **393**, 240, 1998.
- [WWM] S. M. Watts, S. Wirth, S. von Molnár, A. Barry and J. M. D. Coey, Evidence for two-band magnetotransport in half-metallic chromium dioxide. *Phys. Rev. B* **61**, 9621, 2000.
- [XWV] Z. H. Xiong, D. Wu, Z. Vally Vardeny and J. Shi, Giant magnetoresistance in organic spin-valves. *Nature* **427**, 821, 2004.
- [YKD] Z. Yao, C. L. Kane and C. Dekker, High-field electrical transport in single-wall

carbon nanotubes. *Phys. Rev. Lett.* **84**, 2941, 2000.

[YNF] S. Yuasa, T. Nagahama, A. Fukushima, Y. Suzuki and K. Ando, Giant room-temperature magnetoresistance in single-crystal Fe/MgO/Fe magnetic tunnel junctions. *Nat. Mat.* **3**, 868, 2004.

[ZA] G. Zeidenbergs and R. L. Anderson, Si---GaP heterojunctions. *Solid-State Electron.* **10**, 113, 1967.

[ZBH] J. Zhao, A. Buldum, J. Han and J. P. Lu, Gas molecule adsorption in carbon nanotubes and nanotube bundles. *Nanotechnology* **13**, 195, 2002.

[ZD] X. Y. Zhang and J. Y. Dai, Fabrication and magnetic behaviour of superconductor nanowire arrays. *Nanotechnology* **15**, 1166, 2004.

[ZFC] Y. Zhang, N. W. Franklin, R. J. Chen and H. Dai, Metal coating on suspended carbon nanotubes and its implication to metal-tube interaction. *Chem. Phys. Lett.* **80**, 35, 2000.

Acknowledgments

I dedicate my acknowledgments to all the people who contributed directly or indirectly to my doctorate research. I thank Prof. Dr. Kern, University of Tübingen for his kind support and helpful discussions of the thesis. I thank Prof. Dr. Klaus von Klitzing for supporting my work in his department at Max Planck Institute for solid state research, Stuttgart. I give my special thanks to Prof. Dr. Siegmund Roth for his openness, kindness and strong support to not only my research works but also my life in Germany. I have always enjoyed the conversations with Prof. Roth on the topics of physics, history, religions, and so on. I thank Prof. Dr. Po-Wen Chiu at National Tsing-Hua University, Taiwan, for his introduction of this group and guiding me into the world of mesoscopic physics. I thank Prof. Dr. Viera Skakalova for her helps in transport measurement. I thank Dr. Ursula Dettlaff for providing nanotube materials. I thank Dirk Obergfell for his efforts in setting up equipments and helps in fabricating devices. But more than that, I learned a lot from Dirk's work attitude, which shows me the true meaning of "precision" and "made in Germany". I thank Viktor Siegle, my office roommate, for his extraordinary patience in talking with me and solving lots of my problems. I thank Serhat Sahakalkan for his great work in building up equipments, which is important for my research. Additional thanks to Viktor and Serhat for their kind helps and supports to many of my daily-life difficulties. I thank Martti Kaempgen for showing me scandinavian ways of living and thinking. I thank Björn Hornbostel for his enthusiastic expressions of his feelings and opinions on many things, from which I have also benefited a lot. I am appreciated for the permanent and solid assistance in the cleanroom provided by Ulrike Waizmann, Thomas Reindl, Monika Riek and Achim Gueth. Finally, I dedicate this thesis to the memory of Te-Wei Ying. It is you inspiring me to explore more about science. Your excellence in math and physics is admirable, and your courage fighting against illness is respectful. I am forever grateful for your great contributions to my life.

Curriculum Vitae

Name: Chen-Wei Liang

Date of birth: 05. 09. 1979

Place of birth: Taipei, Taiwan

Education:

- | | |
|-------------|--|
| 1985 – 1991 | Shi-Jian elementary school, Taipei, Taiwan |
| 1991 – 1994 | Shi-Jian junior high school, Taipei, Taiwan |
| 1994 – 1997 | Ho-Pin high school, Taipei, Taiwan |
| 1997 – 2001 | National Tsing-Hua University, Hsinchu, Taiwan |
| 2001 – 2003 | National Tsing-Hua University, Hsinchu, Taiwan
Master thesis: Deposition of $\text{Ba}(\text{Ma}_{1/3}, \text{Ta}_{2/3})\text{O}_3$ buffer layer
by pulsed laser deposition process and its
effects on $\text{Pb}(\text{Zr}, \text{Ti})\text{O}_3$ thin film. |
| 2004 – 2009 | PhD thesis: Electrical Characterization of Carbon Nanotubes
for Electronics |

Miscellaneous:

- | | |
|-------------|---|
| 2005 – 2009 | Doctorate scholarship from the Deutscher Akademischer
Austauschdienst (DAAD) |
|-------------|---|